Mechanical properties of single keloid and normal skin fibroblast measured using an atomic force microscope.

A thesis submitted to The University of Manchester
for the degree of Doctor of Philosophy
in the Faculty of Engineering and Physical Science.

2010

Juan Vicente Méndez Méndez
School of Mechanical, Aerospace and Civil Engineering (MACE)

Table of contents

Final word count for this thesis = 46,132

List of Figures

List of Tables

List of abbreviations

TGF	Transforming growth factor
TGF-α	Transforming growth factor-α
TGF-β	Transforming growth factor-β
Nd:YAG	Neodymium:yttrium-aluminum-garnet
C4S	Chondroitin-4-sulfate
MMP-2	Metalloproteinases-2
MMP-9	Metalloproteinases-9
PAI-1	Plasminogen activator inhibitor-1
uPA	Urokinase plasminogen activator
UPR	Unfolded protein response
PDGF	Platelet-derived growth factor
VEGF	Vascular endothelial growth factor
IGF-1	Insulin-like growth factor 1
FPDL	Flashlamp-pumped pulse dye laser
HSP47	Heat shock protein 47
CGRP	Calcitonin gene related peptide
FAK	Focal adhesion kinases
MTOC	Microtubule organizing centre
PDMS	Poly(dimethylsiloxane) stamp
AFM	Atomic force microscope
FEM	Finite element method
VSMCs	Vascular smooth muscle cells
DNA	Deoxyribonucleic acid
RNA	Ribonucleic acid
ECM	Extra cellular matrix
HASM	Human airway smooth muscles
MTC	Magnetic twisting cytometry
SFM	Scanning force microscope
SPMs	Scanning probe microscopes
STM	Scanning tunnelling microscope
SPC	Sphingosylphosphorylcholine

Nomenclature

σ	Normal stress
b	Length of the elliptical crack
a	Width of the elliptical crack
r_c	Smallest radio of the elliptical crack
σ_{max}	Maximum stress
G'	Storage modulus
G''	Loss modulus (imaginary term)
η	Hysteresivity
E_x	Equilibrium Young's modulus
d_m	Diameter of the micropipette
R	Radius of the egg or cell
r_I	Radius of the intrusion
x_I	Intrusion distance
P	Hydrostatic pressure
T_m	Tension in the membrane
P , Δp	Suction pressure
r	Radius of the deformed cell
δ , d	Deformation or deflection
F	Force applied
I	Inertial momentum
E	Elasticity modulus, Young's modulus
R_p	Radius of the pipette
U_t	Velocity of the tether cell
U_f	Velocity of the freely moving cell
n_o	High refractive index
$\vec{F}$	Force due to refraction
n	Index of reflection
$\vec{S}$	Momentum flux of photons
$\vec{S}in$	Direction of the light in
$\vec{S}out$	Direction of the light out
c	Velocity of the light
θ_1	Incidence angle

θ_2	Refraction angle
F_{scat}	Scatter force
F_{grad}	Gradient force
R_r	Relationship F_{grad} / F_{scat}
k_t	Trap stiffness
$\vec{x}$	Distance between the bead centre and focus beam
F_{Tot}	Total force
F_S	Sample contribution force
F_d	Drag force
F_{VdW}	Van der Waals force
F_{el}	Electrostatic force
F_{mag}	Magnetic force
F_{Chem}	Chemical force
ε	Strain
σ_T	Surface charge densities of tip
σ_S	Surface charge density sample surface
ε_0	Vacuum permittivity
ε_w	Dielectric constant of water
D , h	Surface-tip separation
λ_D	Debye length.
H	Hamaker constant
R_T	Tip radius
μ , η	Fluid's dynamic viscosity
R	Spherical radius
v	Relative velocity
$b(h)$	Drag damping factor
$h + h_{eff}$	Effective cantilever tip height
a_{eff}	Effective radius of the cantilever
m_{eff}	Effective mass
k	Spring constant
F	measured force
R_E	Effective radius
$\delta(f)$	Deflection frequency domain
$F(f)$	Force frequency domain
$H_s(f)$	Mechanical transfer frequency domain of sample force

$H_d(f)$	Mechanical transfer frequency domain of drag force
$H'_d(f)$	Real term of $H_d(f)$
$iH''_d(f)$	Imaginary term of $H_d(f)$
$F_s(f)$	Force frequency domain of the sample contribution
$H(f)$	Global mechanical frequency domain transfer
$f_0 \quad \omega_0$	Resonant frequency
S_{FF}	Auto spectrum
S_{ZF}	Cross spectrum
ϕ_{PZT}	Phase shift of the piezoactuator
Re	Reynolds number
F_d	Hydrodynamic force
f^*	Correction factor for deviations from the Reynolds flow in thin gap
k	Spring constant
F	Force
α	Tilt angle
I	Moment of inertia
L	Length of the cantilever
w	Cantilever width
γ^*	Correction factor of the tilt angle between the cantilever and surfaces
A	Fitting parameter which depend of cantilever geometry
H_a	Hamiltonian equation
q	Displacement of the oscillator
p	Momentum
m	Oscillating mass
k_B	Boltzmann's constant
T_{em}	Temperature
$\langle z_c^2 \rangle$	Main square displacement of the cantilever
K	Effective stiffness
δ	Total deformation of both surfaces
θ	Half tip front angle
ν	Poisson ratio Cell
t	Thickness of the cantilever
b	Cantilever base arms distance
Xv	Variable distance between surface-tip
SD,s	Standard deviation

t_t	T-student
tc	Critical value of t_t
$\overline{x}$	Mean
n	Sample size
DF	Degrees of freedom

Abstract

The human body consists of a number of very complex, highly specialised organs which perform a variety of functions that are essential to life and health. One of the main functions of the skin, the largest of the human organs, is to maintain the integrity of the body. It does this by acting as a physical barrier, preventing micro-organisms and other potentially harmful substances from entering the body. When the integrity of the skin is damaged through injury, a self-protective mechanism is triggered and the reparative wound healing process begins. Under normal circumstances the wound healing process culminates in the skin recuperating its normal characteristics and functions at the site of the injury, with only a small visible mark being left behind. However, in some cases the wound healing process may become altered leading to the production of abnormal scars, such as keloids. Keloid scars are formed from scar tissue at the site of an injury, as a result of excessive tissue repair that extends beyond the boundaries of the original wound. These scars are characterised by excess collagen deposition produced during the wound healing process. It is estimated that as many as 20% of the black and Hispanic population are affected by keloid scarring. In addition to the aesthetic aspect, keloid scars can also be painful, itchy and prone to become infected. Keloid scar formation can be triggered by skin injuries caused by, for example, acne, wounds, shaving, burns, and surgical incisions. The mechanism by which keloid scars form is currently not well understood and consequently no effective treatments exist to date.

This thesis describes an investigation into the mechanical properties of single keloid and normal skin fibroblast cells for the purpose of establishing if there is a quantitative difference between the two types of cells. This information will be of benefit to researchers looking for a better understanding of the keloid formation mechanism and for those seeking improved treatments. An atomic force microscope (AFM) was employed to indent single Keloid and normal skin fibroblast cells taken from five patients. Values for the apparent Young's modulus of the cells were then calculated by fitting the experimental data using Hertz's model. Apparent Young's modulus values were then compared. The findings of the analysis indicate that statistically, there is a significant difference in the Young's modulus values of normal and keloid cells, with keloid cells exhibiting substantially greater stiffness than normal skin fibroblast cells.

To enable the keloid and normal skin fibroblast cells to be studied in as close to their natural, physiological environment as is possible the AFM experiments described in this thesis were undertaken in a phosphate buffered saline (PBS) solution. In such cases the use of a fluid medium presents additional complexities, not least of which is the introduction of a hydrodynamic drag force due to viscous friction of the cantilever with the liquid which can affect the experimental data obtained and consequently any material properties calculated as a result of using these data.

In order to investigate the effect of dragging force on the experimental data obtained from the AFM a novel integrated finite element based model was developed. The model, described in this thesis, provides quantification of the drag force in AFM measurements of soft specimens in fluids, consequently enabling more accurate interpretation of the data obtained from AFM experimentation. The model is validated using extensive data obtained from AFM experimentation undertaken in a number of fluids of different viscosities, at a variety of tip velocities and platform-tip separations and by comparison with an existing analytical model. The novel model is shown to accurately account for drag forces in AFM in fluid media without the need for extrapolation of experimental data and can be employed over the range of tip geometries and velocities typically utilised in AFM experimentation.

The work described in this thesis demonstrates that the AFM is a valuable tool that can be used to successfully investigate the mechanical properties of biological samples in fluids. It was shown that increased accuracy in the interpretation of data obtained from AFM experimentation can be obtained by taking into account the hydrodynamic drag force due to viscous friction of the cantilever with the liquid. The investigation into the mechanical behaviour of keloid cells described in this thesis significantly adds to the yet small body of research undertaken on keloid cells to date. The findings of the investigation will provide valuable information that will be of benefit in the future to researchers looking to develop effective treatments for the prevention, reduction or removal of keloid scars.

Declaration

No portion of the work referred to in the thesis has been submitted in support of an application for another degree or qualification of this or any other university or other institute of learning.

Copyright

Dedication

To my mum, dad and family.

Acknowledgements

I would like to extend my deepest and sincerest gratitude to my supervisor, Dr. Teresa Alonso-Rasgado, for all of her support, guidance, insight, patience and constant encouragement. It would not have been possible for me to finish this long and arduous journey without her continued support and concern.

I would like to express my gratitude to Professor Richard Snook for his enthusiastic guidance, valuable suggestions, constructive criticisms and insightful views.

I wish to thank Dr Elsa Correia Faria for her constructive criticisms and insightful views indispensable in improving this work.

I wish to gratefully acknowledge the PhD scholarship No. 173213 and associated financial support provided by The National Council on Science and Technology of Mexico (CONACYT).

I thank Dr. Ardeshir Bayat for providing the cells used in this research work.

I would like to thank to Dr Apolinar Mendoza, Dr Steven Marsden, Ms Barbara Bo-Ju Shih and Dr Syed Farhatullah for their help in the laboratory.

Finally, I would like to thank my friends in Mexico and Manchester for all their support.

Chapter 1

Introduction.

In general when people speak about mechanical properties they are referring to an idea related to inert material. Common engineering materials such as concrete, iron, plastics and glass are used in lots of ways, for example, to build towers or to construct cars, and their mechanical properties are well known (stiffness, shear and Young's modulus, etc). It is necessary to understand in detail how a material behaves in order to take advantage of its mechanical properties and to use it in a proper way. In the selection of materials for an application, factors including loads, costs, and safety – among others- must be taken into account. Safety is often highly important, and for this reason the materials used for construction in engineering are under constant investigation.

However, inert materials are not only studied in engineering, but also in biological organisms. For example, trees are under the influence of loads, and those loads are wielded by the weight of the leaves and branches, which in turn depend upon the degree of humidity and/or the force exerted by wind. This demonstrates that biological organisms are under direct influence of mechanical loads during their life cycle. In the same way, in bioengineering, for example, several parts of the human body attract the attention of researchers looking to find solutions to problems such as prosthesis in the case of skeleton problems or stents for blocked heart arteries. In all these cases the understanding of the forces involved in the biological process is a key element.

The skin is the largest human organ. Its main functions include the protection of the integrity of the body against foreign micro-organisms, the control of body

temperature, the synthesis of vitamins, and the prevention of fluid loss (blood). When this organ is wounded a self-protective mechanism is triggered: first of all, the fluid loss is stopped and then a chain of coordinated and precise reparation steps proceeds, finally and inevitably culminating with the formation of a scar.

Under normal circumstances, the scar process finalises with the recuperation of the main structural, aesthetic and functional characteristics of the skin though a visible mark is left in the place of injury. However, this process can be altered in any of the steps carried out along the healing process resulting in an abnormal scar, as discussed in section 2.2.

Keloid is one of the abnormal scar formations. It is defined as an over proliferative collagen disease characterized by over-grown tissue at the injury site, which rises above the surface, growing beyond the original wound limits. A simple skin cut, a pimple or a major injury or surgery, can trigger keloid formation. It can cause severe itching, and its abnormal aesthetical appearance can have an impact on a person's self esteem and lead to stigmatisation. In addition, Keloids may affect movement capacity due to flexibility loss which can cause problems to perform normal live activities and furthermore it may be a problem to work causing financial problems, as discussed in section 2.3.

The scar process in abnormal scarring is not well understood and the exact mechanism of wound healing regulation remains unknown [1]. Keloids can be present in almost any colour of skin, but it seems that dark skin individuals are more prone to develop them. It has been estimated that Keloids are predominant in up to 20% of black Africans [2]. Also Spanish and Oriental people seem to have a predisposition to develop them. It is possible then that genetic factors are involved, though stress at the site of injury seems also to be related.

Looking at the internal scar process, the most active participants are the cells that actively collaborate in the healing, producing biochemical components, sending and sensing signals, migrating at the site of injury, and finally repairing the injury.

The cell constitutes the basic unit of life and performs a variety of functions: the synthesis, sorting, storage and transport of molecules; the expression of genetic information; the recognition, transmission and transduction of signals; and the powering of molecular motors [3]. The cell also converts energy from one form

to another, and responds to external environments by continually altering its structure [4], for example, in order to allow it to move forward during migration, contractile forces must be generated within the cell [5]. It is known that many important processes are related to the deformation of cells due to mechanical loads [4, 6, 7] and it is thought that mechanical loads and deformation are involved in Keloid formation, as discussed in section 2.5.

The cell commonly experiences mechanical stimulus. "Living cells in the body are constantly subjected to mechanical stimulations throughout life. These stresses and strains can arise from both the external environmental and internal physiological conditions"[8] and they show specific responses to these. For example, muscle cells contract or relax, endothelial cells can become stiff or flexible, and neutrophils can change shape [9]. Moreover, "the process of recognizing and responding to mechanical stimuli is critical for the growth and function of living cells" [10] as well as their cell shape and differentiation. Taking into account the influence that these forces exert in chemical and biological functions [11] it is possible that these mechanical forces might also play a role in the proliferation of Keloids [12].

Other examples that show the relation between these forces and diseases can be found in cancer and malaria [13], where it has been documented that the mechanical characteristics of the normal cells differed from sick ones. In the case of some types of cancer, the disease is spread by the motility of the cell, which means that cancer cells have the ability to remodel their cytoskeleton in order to pass through narrow channels and infect new organs [14].

The study of the mechanical properties of cells is a very challenging task. First of all, cells are very small (10-100 μm), which makes manipulation difficult. Second, cells are very sensitive dynamic microsystems, capable of moving, changing shape and reacting in response to different stimuli [15].

Several techniques such as focal adhesion [16] cell locomotion adhesion forces [17-19], viscoelastic properties and mechanical changes under chemical treatment, etc. have been used in order to study mechanical properties of cells: micropipette aspiration, optical tweezers, magnetometry, engineering substrates, and AFM, among others (Chapter 3). In micropipette aspiration, the micropipette is the main element, which is used as tweezers to grab the sample. Optical tweezers is a technique in which highly concentrated light is used to trap small objects like polyethylene beads, which can be attached to cells making

possible their manipulation. The magnetometry method is based on the physical property of magnetism which can be used to attract or repel ferromagnetic materials. A magnet is used in order to impinge the generated magnetic force on small magnetic beads attached to the cell surface. A posterior analysis of the relationship between the applied force and bead displacement is used to calculate the mechanical properties of the cell. Substrates such as polymer gels, polymer films, elastomeric substrates, glass, polystyrene and silica are used to study some cell properties such as focal adhesion, migration sensing cell mechanism, motility and tractional forces. AFM is an instrument that belongs to the family of scanning probe microscopes (SPM). Created by Gerd Binnig and Christoph Gerber in 1986 [20], it is a very useful tool for performing mechanical experiments of biological samples. A very sensitive and tiny cantilever is used to indent cells, and with this information the mechanical properties of cells can be investigated, as discussed in Chapter 3.

The AFM has been used to indent single keloid and normal skin fibroblast cells to calculate the apparent Young's modulus (section 3.6) by fitting Hertz's model (section 6.8). The results were then compared to study if this parameter can be used to investigate the mechanical differences between both cell types. AFM is a useful tool because it is possible to perform experiments in fluids to reproduce the cells natural environmental conditions and to avoid alterations in the cells normal processes. However, the use of relatively viscous fluids brings uncertainties because drag forces are generated due to the interaction of the cantilever and the fluid. Therefore, in order to better understand this phenomenon a finite element model (FEM) has been created (Chapter 5) to quantify the drag forces and study its affect on the determination of the apparent Young's modulus.

The complete understanding of the mechanical functions of the cell will enable the correlation of mechanical changes with specific diseases such as malaria and cancer openning the possibility of the development of techniques that allow the monitoring, prediction and tests of new drugs.

This thesis describes an investigation into the mechanical properties of keloid and normal skin fibroblast cells using AFM measurements undertaken in order to determine the differences between the two types of cells, as discussed in Chapter 6.

In addition, the influence of hydrodynamic drag force on AFM measurements of soft samples in fluids is established by the development of a finite element model. The model enables the hydrodynamic drag forces present during AFM measurements of soft samples in fluids to be accurately quantified without the need to determine empirical coefficients or extrapolate data, consequently providing more accurate interpretation of the data obtained from AFM experimentation, as discussed Chapter 5.

Chapter 2

Keloid scars and mechanical properties of cells.

2.1 Introduction.

A keloid scar is defined as a dermal tumour that spreads beyond the margin of the original wound, that continues to grow over time, that does not regress spontaneously, that often recurs after excision, and has been present for at least 1 year [21]. The first known written description of a keloid scar was made centuries ago in the Smith papyrus in ancient Egypt [22]. A later description was provided by Retz [23] in 1790. In 1802 Alibert [12] introduced the name "Cheloide", from the Greek "Chele", meaning Crab's claw.

2.2 Skin.

The skin is the largest organ of the body. One of its main functions is to protect the body from external physical, chemical and biological attacks, preventing the contact of some of the fragile systems within the body with harmful microorganisms such as bacterial invasion. Additional functions of the skin include the synthesis of vitamin D and temperature control. Furthermore, the numerous nerve termini within the skin are responsible for the sense of touch. The skin also helps to regulate body fluids such as water and contains networks of capillaries to circulate blood in the skin. The skin is the interface between

mammals and the exterior world; Figure 2.1 shows a schematic representation of skin and its components [24, 25].

Skin is made up of multiple layers and sublayers, each one with its own important components and functions. The first layer is the epidermis, the outermost layer and therefore the visible part of the skin. It is made up primarily of keratinocytes (90-95%), with Langerhans cells, melanocytes and Merkel cells making up the remaining 5-10%. This layer renews itself continually by a process which is carried out initially at the bottom of the epidermis where the keratinocytes cells originate from mitotic division of stem cells. Once the cells are ready they move up towards the epidermis and near to the surface they die. Thus the visible skin is formed by dead cells which are constantly being lost and replaced by new cells. One of the functions of the epidermis is the production of a substance called melanin which gives the skin its colour. Dark skin produces more melanin, a substance that protects the skin from getting burned by the sun's ultraviolet rays when exposed. The cells produce extra melanin changing the skin colouration to avoid damage in the skin [25].

The second skin layer is the dermis, a supportive compressible and elastic connective tissue. It is formed from cells (fibroblast, dermal dendrocytes and mast cells), fibrous molecules and a ground substance (glycoproteins and proteoglycans), and contains sweat glands, nerve endings, blood vessels, hair follicles, hair erectors and oil glands. It also contains collagen and elastin, which are tough and stretchy. The nerve endings give the sense of touch sending harm signals to the brain or spinal cord, which results in orders being immediately sent to the muscles to react, avoiding damage to the skin. Blood vessels transport oxygen and nutrients to cells. The hair erector muscle is connected to each hair follicle and the skin; it contracts in response to cold, fear, etc. Oil or sebaceous glands produce sebum a natural skin oil. Sweat glands produce sweat which helps to control the body temperature through evaporative cooling [25].

The third layer is the subcutaneous tissue (hypodermis) which is mostly made up of fat, which helps the body to stay warm and absorbs shocks. The main cells of the subcutaneous tissue are the adipocytes [25].

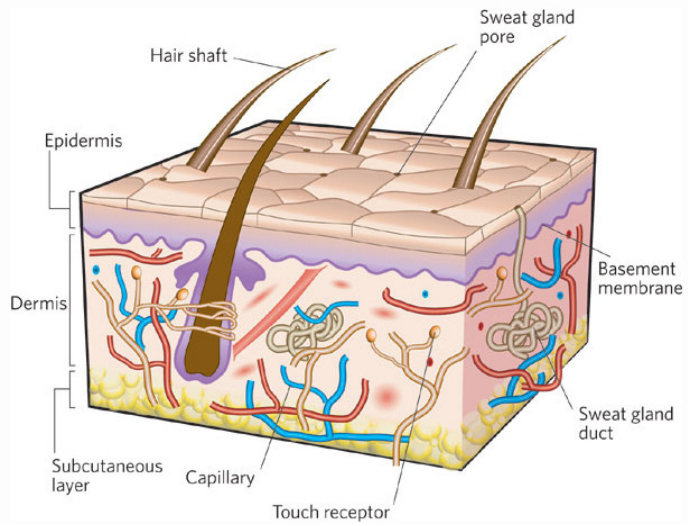

Figure 2.1 Skin structure, figure taken from [26].

The skin is under constant mechanical loads, stressing and straining it daily. Some activities can result in injuries, triggering a self reparation process to recover the integrity of the skin and to keep its functions. The result of this healing process is a scar.

2.3 Wound healing process.

When normal skin is wounded it initiates and orchestrates a cascade of repair phases that culminates in scar formation at the site of injury [1], a process known as cicatrisation or scarring. This process initially repairs the tissue temporarily, forming a clot that serves as protection for the denuded wound tissue, stopping blood loss by constricting the blood vessels and preventing the loss of components like growth and coagulation factors and cytokines that fill the injury site and generate a new matrix through which cells can migrate during the repair process [1, 27]. Next, a hardened crust is formed over the top of the wound, while internally the cicatrisation process continues.

The normal wound healing process progresses in an orderly and efficient manner. It is characterized by four overlapping phases: hemostasis, inflammatory, proliferation and remodelling [1, 28].

Hemostasis. In this phase the foreign material and damaged tissue is removed and the phagocyte process is initiated.

Inflammatory. The removal and phagocyte process is continued by macrophages. Once the wound is cleaned out, fibroblast, epithelial and endothelial cells migrate and the proliferation phase begins [1].

Proliferation. Fibroblasts are synthesized and deposit a new scaffold called the extracellular matrix filling the physical defect caused by the injury. The matrix becomes cross-linked and organized during the final phase. In this phase a great quantity of biochemical components are produced, for example transforming growth factors β (TGF-β) which are considered the master control signal of fibroblast, vascular endothelial cell growth factors (VEGF) involved in new blood vessel formation [1], and epidermal growth factors (EGF) and transforming growth factors α (TGF-α) that stimulate the epithelisation.

Remodelling. Once the wound is filled completely with a substance formed by proteoglycans and glycoproteins the amount of collagen and fibril cross-linking increases to provide the scar's ultimate strength [1]. When the feedback and control mechanisms among the participant components fail, the result is an abnormal healing [2].

The desired cicatrisation is the total regeneration of the new tissue, with the same structural, aesthetic, and functional characteristics as the original uninjured skin [1]. Unfortunately, however, this is not always the outcome. The four possible results of cicatrisation are shown in Figure 2.2. Note that these are not the only possible outcomes of cicatrisation, however, the vast majority of cases can be classified into one of these four groups. The rate and quality of scar formation varies amongst individuals as it depends upon the size, depth and location of the scar and genetic disposition, hormones, skin colour, etc, factors that may cause alterations in the healing process.

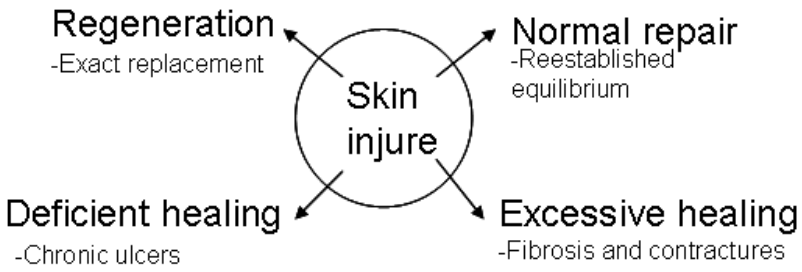

Figure 2.2 Possible responses of the skin to injury.

The four possible results of cicatrisation are:

Regeneration this refers to a scar which heals completely recovering the original function and appearance of the organ, for example regeneration occurs in lower vertebrates, such as salamanders and invertebrates [1] and in embryos [29], etc. This cicatrisation constitutes scarless healing.

Normal repair occurs in most of the cases. A small mark is left at the site of the injury and the organ recovers its original functions completely.

Deficient healing produces contractures that shrink the open wound but produce ulcers, i.e. deficient cicatrisation that can incapacitate the person [30].

Excessive healing occurs when the body overreacts to the healing process, leading to the development of thick and/or raised scars, for example, keloid and hypertrophic scars.

2.4 Keloid scar.

Keloid scar formation can be triggered by a simple skin cut, pimple problems, burns, sternum infections, following acne, chickenpox, trauma or surgery [2, 23] or any injury that damages the skin. Keloids represent a clinically distinct form of pathological scarring which occurs during skin wound healing, formed by the excessive accumulation of connective tissue arising in sites of trauma [31]. They are unique in humans [32]. Abnormal scars can cause symptoms like severe itching, aesthetically unpleasant disfiguring, for example changes in the texture and colour, which can affect psychosocial development and cause anxiety, depression and disruption in daily activities [33]. Functionally, keloid cicatrisation can cause the limitation of movement capacity due to flexibility loss [23]. Other psychosocial consequences are development of post-traumatic stress reactions, loss of self esteem, and stigmatisation, which can in turn be associated with substantial emotional and financial cost [29].

The scar process in abnormal scarring is not completely defined and the exact mechanism of wound healing regulation remains unknown [28]. Keloid appearance is related to several factors; it can be present in almost any colour of skin, but it seems that dark skinned people are more prone to develop them. It has been estimated to occur in up to 20% of black people [2]. Spanish and Oriental people seems to have a predisposition to develop keloid scars and

people with black heritage are more susceptible to present with this kind of cicatrisation. In addition, it seems to be related to hormonal changes, appearing in adolescent or pregnant women and is related to the immunological system. The exact number of sufferers is unknown but estimates suggest that there are 11 million keloid and four million burn scar sufferers, 70% of whom are children in the developed world [29].

Keloid scars are sometimes difficult to identify and some times are confused with hypertrophic scars, with which they have some clinical similarities. Pathologically, however, there are differences that distinguish one from the other [31]. Keloid scars extend beyond the wound boundary and tend to remain elevated whereas hypertrophic scars form within the boundary of the original wound, rise intensely for several months and then regress over time [31, 34]. The difference is that keloid scars tend to grow beyond the original margins of the injury. If a raised scar is still emerging after a year, a keloid scar is a potential diagnosis. In contrast, hypertrophic scars generally show some evidence of regression over this time period. Although there are pathologically differences between keloid and hypertrophic scars, morphologically they can be similar which can lead to errors in identification. Figures 2.3 and 2.4 are examples of keloid scar formation.

Figure 2.3 Keloid formation on the back of the head, picture courtesy of Dr Ardeshir Bayat.

Figure 2.4 Chest keloid formation, picture courtesy of Dr Ardeshir Bayat.

2.5 Keloid Scar formation.

Keloid scars are one of the possible outcomes of the wound healing process. The exact mechanism is unknown, however, normal and keloid scar formation processes are similar in the early stages. The major difference is that keloids produce excessive collagen [23, 34], and/or insufficient degradation of collagen and other extracellular matrix proteins including proteoglycan, identified as chondroitin-4-sulfate (C4S) [23], fibronectin and elastin [35]. Several hypotheses have been suggested to explain this behaviour involving biochemical, metabolic and/or immunological factors [31]. One of these theories suggests that since keloids are characterised by an excessive accumulation of collagen, perhaps there is an imbalance in the production of the protein that stimulates and/or degrades collagen protein [31]. The proteins involved in the protein stimulation and/or degradation of collagen are metalloproteinases, MMP-2 and MMP-9; both degrade types IV and V collagen, gelatine, elastin and proteoglycan core protein; "MMP-2 has been associated with normal, daily remodelling of the extracellular matrix, while MMP-9 may be more involved in early repair in response to injury"[31].

Altered growth factor milieu is responsible for the exuberant scar tissue found in keloids attributed to an over-activity of transform growth factor (TGF-β) and platelet derived growth factor PDGF, growth factors normally produced during the proliferative phase of wound healing [34]. TGF-β is a cytokine responsible for the over-deposition of collagen [32]. TGF-β are polypeptides that transmit signals to modulate cellular activities, differentiation, migration, gene

expression, chemotaxis, matrix synthesis [36], and local delivery of growth factors that can induce both cell stimulation and inhibit cellular proliferation [21]. TGF-β1, 2 and 3 and their receptor transforming growth factors I and II (TGF-βI and βII) have been investigated to elucidate if there is an abnormal production of these factors expression [37].

Using an in vitro fibroplasia model it was found that an increase of plasminogen activator inhibitor-1 (PAI-1) was associated with the reduction of urokinase plasminogen activator (uPA) in keloid fibroblast [2]. Another hypothesis suggests that fibroblast from keloids may have an enhanced activation of unfolded protein response (UPR) [38]. Others point to the platelet-derived growth factor (PDGF) [28] involved in the production of growth factors. In addition, vascular endothelial growth factor (VEGF) has been found to be expressed in keloids [33].

The location of the scars (head, shoulders, chest etc) suggest that the factors involved in keloid formation may include a local factor (see section 2.5.4), furthermore the appearance of keloids during puberty, menopause and pregnancy may indicate that endocrinologic changes may be associated with keloid formation, as these periods are characterised by large changes in hormones [23, 39]. The common recurrence of keloids between the ages of 10-30 years at which time plasma levels of growth hormones and insulin-like growth factor 1 (IGF-1) are high, suggests that hormones may influence keloid formation. In addition, genetic predisposition seems to be related to the abnormal healing process combined with other factors [39] such as immunological factors [12], sebum reaction, and altered mechanical tension alignment [34]. Also, keloids are related to alterations in components of the extracellular matrix that regulate growth factor activity. Characteristically the extracellular matrix of keloids is abnormal, with elevated levels of fibronectin and certain proteoglycans, resulting in a disorganized extracellular matrix and collagen architecture and decreased levels of hyaluronic acid [34].

"Other dermatological diseases have been associated with keloid formation including: dissecting cellulitis of the scalp, acne vulgaris, acne conglobata, hedradenitis suppurative, pilonidal cysts, foreign body reactions, and local infections with herpes, smallpox or vaccinia. Keloids have been noted in individual cases of patients with Ehlers-Danlos syndrome, Rubestein-Taybi syndrome, and pachydermoperiostosis but the relation of keloids with this disease is unknown"[23].

2.5.1 Genetic factors.

Higher recurrences of keloids have been found in darker-skinned races. It has been suggested that genetic predisposition may trigger keloid formation [21], and a familiar predilection for keloid formation has been noted; both autosomal recessive and autosomal dominant inheritance patterns have been reported. A positive family history is more likely [23] consistent with an autosomal dominant mode with incomplete clinical penetration and variable expression [39]; these observations have led many researchers to study the genetic factors that predispose people to keloids. Many genes have been found to be related to the generation of keloids, including TGF-β, PDGF, VEGF, p53, and HSP47 [40]. In addition, it has been hypothesized that the unfolded protein response (UPR) [38], metalloproteinase [31] and fobronectin [41] are implicated in keloid formation.

2.5.2 Growth factors.

The scarring process implies the coordination of cells involved in the healing process; this coordination suggests signalling between cells of the same type (autocrine activity) and with other types of adjacent cells (paracrine activity) by means of transforming growth factor [42]. TGF-β and subtypes TGF-β1 and TGF-β2. TGF are cytokines which are one of the four major signalling molecules, alongside neurotransmitters, endocrine hormones and autocoids. It has been suggested that cytokines play a major role in controlling the remodelling of tissue [43]. TGF are polypeptides that act in picomolar to nanomolar concentrations. An abnormal signalling is thought to be responsible for the formation of keloids, through TGF regulation of cell proliferation, migration, differentiation, extracellular matrix degradation [21] and repair [32].

2.5.3 Mechanical influences in keloid scar formation.

Cells commonly experience mechanical stimulus, "living cells in the body are constantly subjected to mechanical stimulations throughout life. These stresses and stains can arise from both the external environmental and internal physiological conditions"[8] and cells show specific responses to these. For example, muscle cells contract or relax, endothelial cells can become stiff or flexible, and neutrophils can change shape [15]. "The process of recognizing and responding to mechanical stimuli is critical for the growth and function of living cells"[10], and thus other processes including mobility, "consisting of a

complex set of integrated molecular events that are vital to many life processes"[15], growth, cell shape, and differentiation [9] that constitute some of the main tasks of cells.

During the past few decades, research has established the connection between structure, mechanical responses and biological functions of different organs and tissue including for example, the heart, lungs, bones and tissues, blood vessels and skeletal and cardiac muscles [44]. Also, research has established how hypertension affects arteries, by characterizing the changes of the arterial wall associated with hypertension [9].

It is not known completely how deformation can affect some processes, nevertheless, it is known that mechanical loading of cells induces deformation and remodelling, which influences many aspects of human health and disease (for example, malaria [13], lung diseases, blood vessel disease [6]). Mechanical forces strongly influence chemical and biological functions [11], for example it is known that the mechanical characteristics of cancer cells are different from healthy cells. Cancer is spread due to the motility of the cell which can be attributed to the remodelling of the cytoskeleton. In the treatment of cancer therefore it is important to control this motility [14, 45].

Hypotheses suggest that mechanical stresses (tension and compression forces) are involved in keloid formation [12]. Mechanical stresses seem to be closely associated with fibro-proliferation disease [34]. Satoshi [46] in the "neurogenic inflammation hypothesis" hypothesizes that "mechanical stress, including skin stretching, stimulates mechanosensitive nociceptors on sensory fibres in the skin. Stimulated fibres release neuropeptides, including SP and CGRP, and these peptides bind to the receptors (SP-NK1R and CGRP-CGRP1R) on various cells in the skin, including keratinocytes, fibroblast, mast cells and endothelial cells. Consequently, activated endothelial cells induce vasodilatation and permeabilization of vessels". "Cytokine production, including TGF-β and NGF in various cells are also stimulated by neuropeptides".

Ogawa [40] hypothesizes that keloids and hyperthopic scars are developed because mechanical forces may be detected by two different types of receptors. These include cellular mechanoreceptors (also known as mechanosensors) and the receptors on nerve fibres which include mechanosensitive nociceptors which produce the somatic sensation of mechanical forces.

In vitro and in vitro investigations suggest that forces promote collagen production and dictate collagen architecture and orientation and affect dermal remodelling [34]. Forces are a factor that not only aggravate keloid growth but also promote their generation [40]. Forces are transduced via integrin-matrix interactions, which then signal to focal adhesion kinases (FAK). Subsequent downstream signal propagation leads to a wide variety of cellular responses, including promotion of cell survival [47].

2.5.4 Site specificity of keloids.

It is known that keloids occur in particular sites. The sites of highest scar recurrence are the anterior chest, the shoulder, especially the scapular region, the ear lobe and suprapubic region [13, 40, 46, 48, 49]. In normal day life these sites are stretched by cyclical movements, the chest is stretched by normal breathing, the scapular region is constantly stretched by movements of the upper limbs and the bending motion of the body, the suprapubic regions are commonly stretched by sitting and standing movements. The shape of the scars formed in such sites suggests that the stretching force shapes the scar. Figures 2.5 and 2.6 show a chest and shoulder scar respectively. The shape of the scar in both Figures appears to have been driven by the stretching forces present [40, 46].

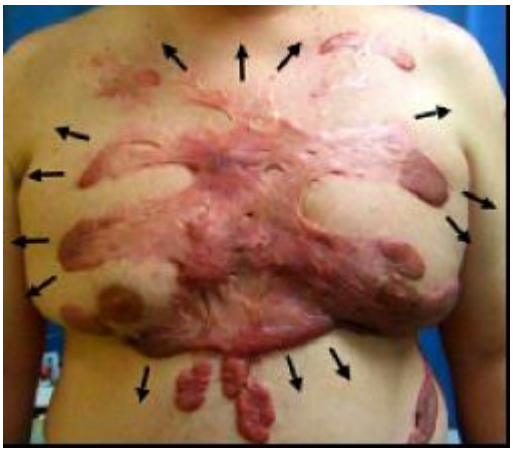

Figure 2.5 Keloid chest scar formation, taken from [40].

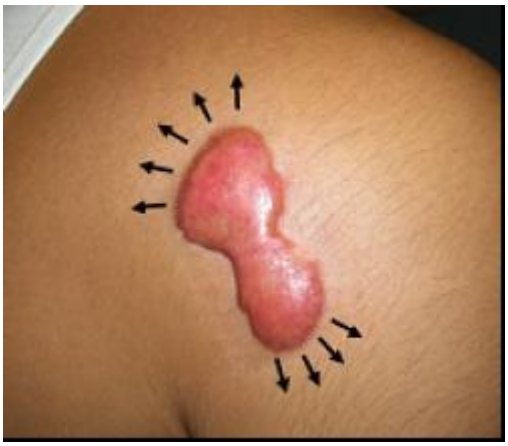

Figure 2.6 Keloid shoulder scar formation, taken from [40].

The shape of the scar is almost characteristic of the zone where it appears, for example ear lobe keloids often grow as large lobules, external keloids on central regions of the body commonly develop a butterfly shape (Figure 2.6), deltoid

keloids tend to extend vertically [40], and on the chest, keloids develop in a crab like shape (Figure 2.5). The regions where keloids commonly occur seem to be related to tension forces, stretching the initial injury triggering the keloid formation. Earlobe keloids seems to be the exception [12], occurring in an area where typically no tension forces exist.

It is possible by analysing a simple cut to relate the mechanical forces involved in keloid formation to tension. Consider the case of an initial injury that is linear (see Figure 2.7), located in the central part of a section of skin. If it is assumed that forces are not applied in this case, then the shape and dimension of the scar will not change. If tension forces are applied, as illustrated in Figure 2.8, then the initial scar will be deformed, becoming elongated, opening up in the central part.

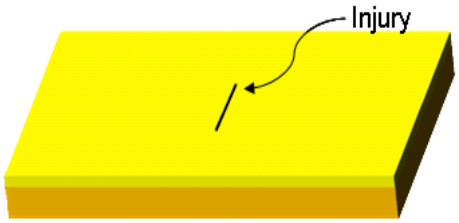

Figure 2.7 Skin injury, no load applied, adapted from [50].

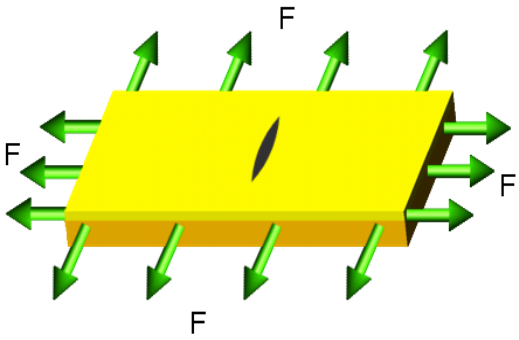

Figure 2.8 The skin loaded by tension, adapted from [50].

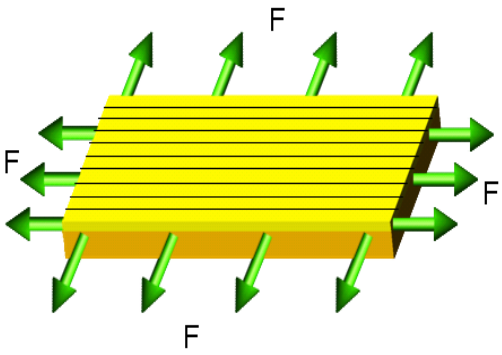

Figure 2.9 Skin without injury, stress lines in response to load force, adapted from [50].

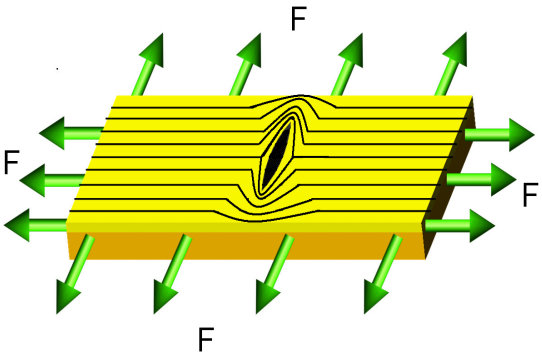

Figure 2.10 Skin injury, stress lines in response to load force, adapted from [50].

Further, it is of interest to analyse the stress lines for the cases of injured and uninjured skin. In the case of skin which has not been injured, illustrated in

Figure 2.9, the stress lines are uniform because the skin in which the stress lines propagate is continuous. If however the continuity of the skin is altered by an injury, as illustrated in Figure 2.10, then this causes the stress lines to be concentrated at the sharp extremes of the injury. A similar problem has been addressed in mechanical engineering, as illustrated in Figure 2.11. In this problem a plate with an elliptical crack in the centre, of length $2b$, width $2a$ and smallest radius r_c, is subjected to forces which are applied on two opposing ends. These forces cause a stress σ to be generated in the plate.

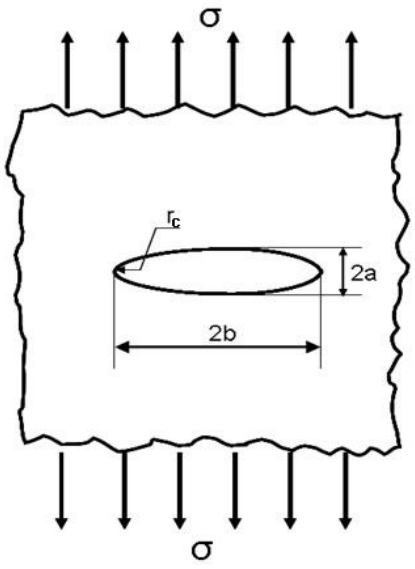

Figure 2.11 Plate with elliptical crack, adapted from [50].

The maximum stress can be calculated using the empirical expression for an elliptical crack [51]:

$$\sigma_{\max} = \sigma\left(1 + 2\frac{b}{a}\right) = \sigma\left(1 + 2\sqrt{\frac{b}{r_c}}\right) \tag{2.1}$$

Where σ results from the force applied on a normal area; $2b$ is the length, $2a$ the width and r_c is the smallest radius of the crack. The analysis of this expression shows that when r_c approaches zero, $\sigma_{\max} \to \infty$.

Figure 2.12 shows the case of the simulation of an elliptical shaped scar under tension. The results indicate that the highest stress concentration occurs around the smallest radius of the scar. The stress pattern forms a butterfly shape which can also be clearly distinguished in the photograph of the actual keloid scar shown in Figure 2.12. The accumulation of larger amounts of scar tissue may be

a response to the highest concentrated stress in such an area. This observation is consistent with Wolff's law [52]. Wolff proposed that the skin's form is determined by the stress in the skin.

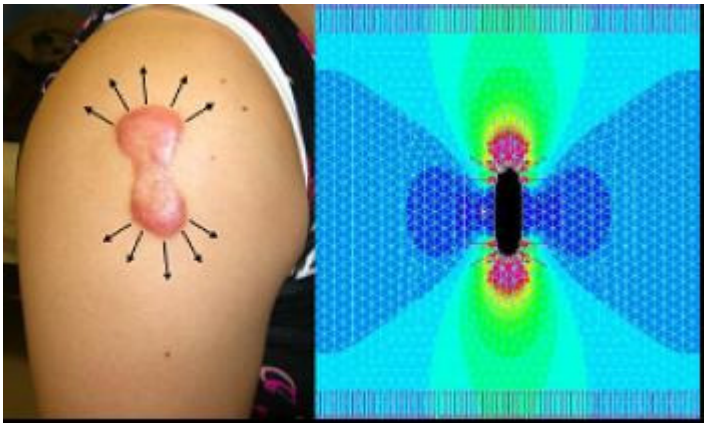

Figure 2.12 FEM scar simulation, taken from [53].

2.6 Keloid scar treatment.

Some of the methods that have been used to treat keloid scars include intralesional steroid injections, 5-fluorouracil, paper tape, pressure application, silicone sheeting, radiation laser therapy, surgical excision, corticosteroid and injections among others [34]. Also, combinations of these methods have been tried in order to improve their effect, for example excision and intralesional injection of steroids have been tried together [49], as have CO_2 laser treatment and surgical excision [54] and excision and radiotherapy treatment [55].

The paper tape method consists of the placement of paper tape over the wound to control wound widening; better results have been obtained with the tape placed longitudinally along the wound as opposed to transversally across the wound [56]. In radiation therapy, several laser types and wavelengths have been tried for example, the flashlamp-pumped pulse dye laser (FPDL) [57] has been frequently used in the treatment of keloid scars and also carbon dioxide, argon, and neodymium:yttrium-aluminum-garnet (Nd:YAG) laser radiation have been used to reduce keloid recurrence rates which can be greater than 90% [54]. Pressure therapy has been established as an effective option. This technique consists of the application of pressure directly over the wound. The ideal pressure needs to be between 24-30 mmHg [58]. Corticosteroids such as hydrocortisone acetate, methylprednisolone, dexamethasone and the more widely used triamcinolone acetate have been used in the treatment of keloid and hypertrophic scarring. The injection of corticosteroids reduces the fibroblast

production of collagen and glycosaminoglycan synthesis and reduces the production of basic FGF-β1 [59]. Silicon gel therapy is also used as a treatment in an attempt to minimize the formation of prominent scars such as keloids. It is also used in purely cosmetic surgery, as the silicon plasters that were initially used were found to be uncomfortable. In contrast, the use of silicon gel makes for a very comfortable application [60]. Surgical excision of keloids by itself generally results in lesion recurrence, with recurrence rates of between 45 and 100 %. This can result in a keloid of larger dimensions. Subtotal excision along with lateral undermining have been credited with improved outcomes and fewer recurrences [49]. Antimetabolites 5-Fluorouracil and triamcinolone intralelesional injections given over a period of time can cause the scars to flatten and soften [61-63]. Other techniques such as suture [64] and cryosurgery [65] are also used. A combination of therapies has been tried with the objective of improving effectiveness over that of applying the treatments individually. A combination of surgery with either intralesional corticosteroid injections or with radiotherapy, and surgery with post operative radiotherapy [48, 55] has also been tried.

2.7 Structure and properties of the cell.

Cells possess structural and physical properties that allow them to support external and internal mechanical stimuli. Lim et al. [8] suggest that mechanical deviations can modify physical and biological functions. The authors point out that stimuli such as fluid shear of endothelial cells activates hormone release and intracellular calcium signalling. Also, the mechanical compression of chondrocytes cells modulates proteoglycan synthesis and in addition the tensile stretching of cell substrates can alter both cell motility and orientation. Furthermore, Lim et al. [8] note that certain chemicals can increase and decrease cell stiffness, for example chemotactil agent f-Met-Leu-Phe (fMLP) can increase the stiffness of neutroplis cells. In the case of keloid scar formation it is thought that mechanical loads may be responsible for cell mechanical alterations, causing changes in cell structures such as the cytoskeleton that can trigger abnormal scar formation (section 2.5).

2.7.1 Animal cell structure.

Cells are the building blocks that form the human body. They are very complex microsystems. A cell is directly involved in the most important processes that take place in the body, synthesizing proteins, apoptosis, engulfing nutrients, dividing for proliferation, storage and transport of molecules, expression of

genetic information, transmission and transduction of signals [7, 18], and reacting in response to internal and external stimuli. Dynamically, the cells actively migrate on a matrix [17]; for example in scar formation cells play a very important role migrating to the site of injury, participating in every stage of scar formation [1]. Cells respond to stimuli by changing their mechanical properties or by performing a mechanical function which means that cells constantly change depending on the task performed. For example, blood cells are capable of passing through narrow channels deforming in the process. Some diseases have been related to mechanical changes in cells, for example in the study of malaria it was found that the stiffness of the cell is increased due to the disease [13]. In cancer research it has been found that cells lose their original stiffness enabling the cell to migrate and infect other parts of the body which implies that cancer cells lose stiffness due to the disease. In the nervous system the deformation and motility of the cells is fundamental in nervous system formation.

Cells are made up of several organelles, including the centriole, lysosome, mitochondria cytosol, vesicule, nucleus, nucleolus and ribosome, amongst others, as illustrated in Figures 2.13 and 2.14. It is likely that every organelle has its own particular mechanical characteristics, for example, investigations have determined that the stiffness of the nucleus can be several times greater than that of the cytoplasm [66] and such heterogeneity complicates the determination of the mechanical properties of the cell because it is difficult with some experimental methods to know exactly if the measurement obtained is influenced by the nearest organelle. In this section some cell organelles will be described in order to demonstrate the heterogeneity of the cell. In addition, the cell components that give the cell its static structural and dynamic characteristic will be described.

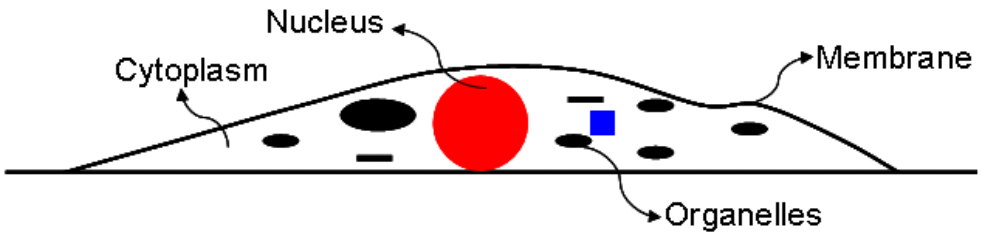

Figure 2.13 Schematic representation of a spread cell.

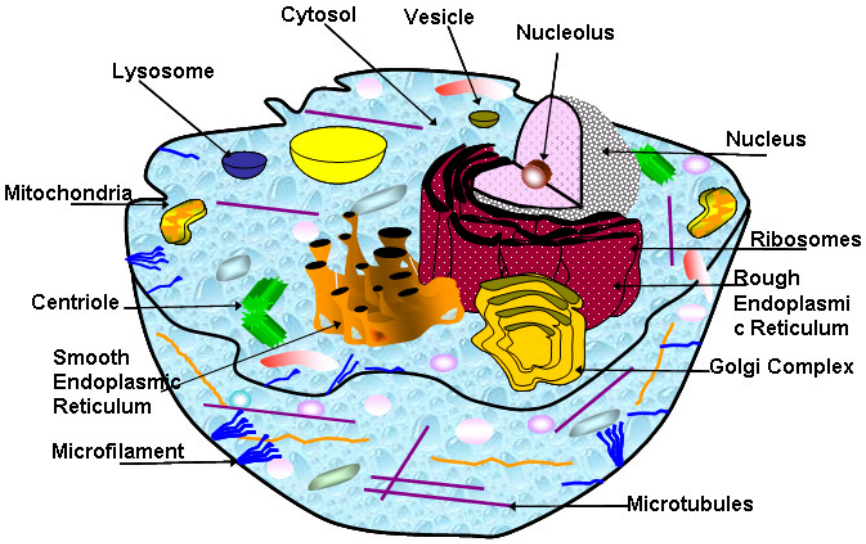

Figure 2.14 Animal cell structure.

2.7.1.1 Plasma membrane.

The plasma membrane is a semiporous envelope; it is the cell's first barrier and is $\sim 3\ nm$ in thickness [67] (NIH3T3 fibroblast cells). It provides protection from the outside environment and selectivity of substances such as nutrients and waste. Plasma membrane is formed by a double layer (bilayer) of lipids; oily substances found in all cells. In the outer surface membrane layer carbohydrates referred as glycoproteins are attached.

The plasma membrane interacts directly with the cytoskeleton, confining and shaping it. Conversely the cytoskeleton is able to modify the membrane shape, for example in migration [68] the cytoskeleton is involved in the formation and retraction of filopodia, lamellipodia, and neurites which suggests the existence of a strong adhesive interaction between the plasma membrane and the cytoskeleton [69]. In the plasma membrane some proteins serve as structural links that connect the membrane to the cytoskeleton and/or to either the extracellular matrix or an adjacent cell [70]. Figure 2.15 shows an artist's representation of the membrane and cytoskeleton structure, where it can be observed that the cytoskeleton is attached to the proteins inserted in the membrane [71].

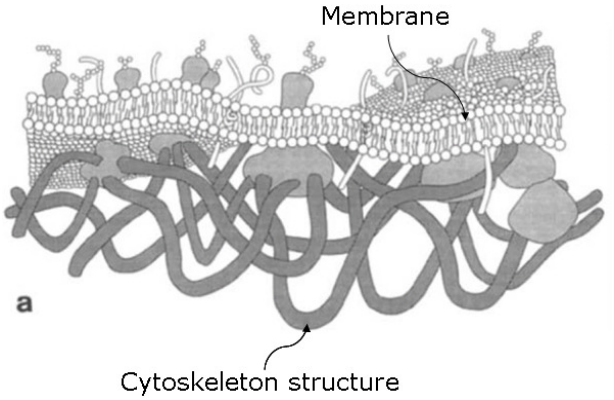

Figure 2.15 Schematic representation of the linked cytoskeleton structure and membrane of a red blood cell, taken and modified from [71].

2.7.1.2 The cytoskeleton.

The cytoskeleton is internal scaffolding that provides stability and integrity to biological cells (see Figure 2.16). It determines the cell shape and its mechanical deformation characteristics. In migration it behaves like a muscle generating contractile forces and driving cellular motile functions. In addition, it provides mechanical consistency to the cytoplasm [72]. The cytoskeleton is also involved in important mechanisms and processes such as mitosis and mechanotransduction [73]. The cytoskeleton is a dynamic three-dimensional web of protein subunits, a few nanometers in size. These subunits can assemble to form very large structures, tens or even hundreds of micrometers in size. The small protein size makes diffusion in the cytoplasm relatively easy, enabling movement from one site to another site far away [74]. The primary types of fibres comprising the cytoskeleton are microfilaments, microtubules, and intermediate filaments. The cytoskeleton works independently of the nucleus and most of the organelles of the cell. It has been demonstrated that cell stiffness is very sensitive to the cytoskeletal dysfunction [68]. Cytoskeleton filaments are anchored to specific proteins embedded in the membrane [70].

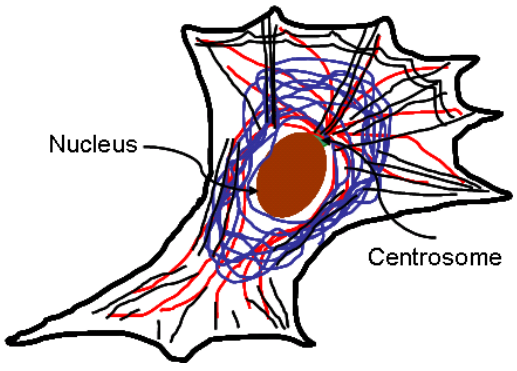

Figure 2.16 Cytoskeleton web, Adapted from [74].

2.7.1.3 Microfilaments (actin filaments).

Microfilaments are fine, thread-like protein fibres, 6-8 nm in diameter (Figure 2.17). They are formed predominantly of a contractile protein called actin, which is the most abundant cellular protein. Actin filaments provide the highest resistance to deformation up to a certain critical value of local strain. Microfilaments associated with the protein myosin are responsible for muscle contraction. Microfilaments can also carry out cellular movements including gliding, contraction, and cytokinesis [73].

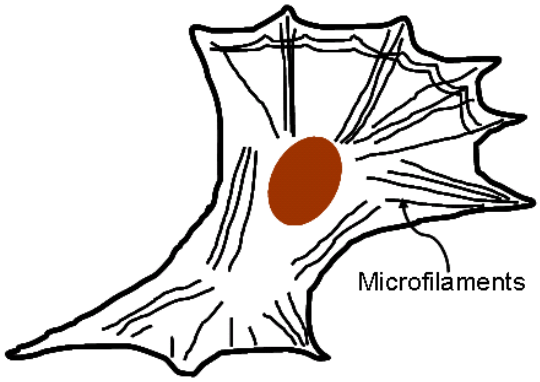

Figure 2.17 Microfilaments, adapted from [74].

2.7.1.4 Microtubules.

Microtubules are responsible for various kinds of movements in all eukaryotic cells. They are part of the intracellular structure, and are approximately 25 nm in diameter. They are long, hollow cylinders with an end connected to a single microtubule organizing centre (MTOC) called the centrosome [74]. These filaments are involved in nucleic and cell division, organization and division structure, and intracellular transport, and also ciliary and flagellar motility [73]. Microtubules are made of a protein, tubulin; they are significantly more rigid than microfilaments (Figure 2.18).

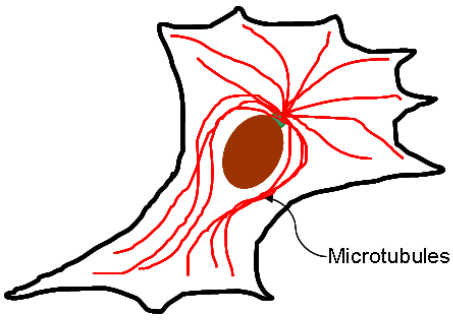

Figure 2.18 Microtubules, Adapted from [74].

2.7.1.5 Intermediate filaments.

Intermediate filaments are made of elongated and fibrous elements, they give the cell shape, and organelle motility. They are essential in chromosomal division [75]. Intermediate filaments surround the nucleus and extend throughout the cytoplasm to the cell membrane enclosing most of the organelles; they form a stable structure [76].

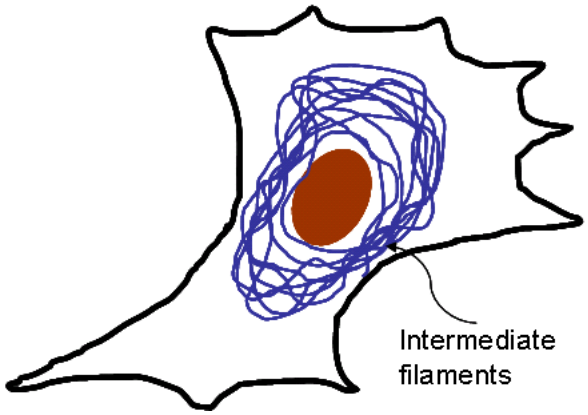

Figure 2.19 Intermediate filaments, adapted form [74].

2.7.1.6 Nucleus.

Structurally, the nucleus consists of three main parts, the nucleus, the nuclear envelope, and chromatin. Research has determined that the nucleus is around 3-4 times stiffer than the plasma membrane [77]. In the investigation undertaken by Guilak [77], a chondrocite nucleus was isolated using a micropipette aspiration technique similar to that described in section 3.2. This technique was used to determine the equilibrium Young's modulus (E_x) which was found to be of the order of 1 kPa. In the investigation performed by Maniotis et al., Dong et al. and Caille et al. [66] the stiffness of the nucleus was found to be between 3 to 10 times bigger than the cytoplasm. Caille et al. [66] found the average elastic modulus for spread and round bovine endothelial cells to be of the order of 5000 N/m^2. Usually the nucleus is round in shape and is the largest organelle in the cell. It is surrounded by a membrane, called the nuclear envelope, which is similar to the cell membrane that encloses the entire cell. The envelope is punctured with holes, called nuclear pores that allow specific materials to pass in and out of the nucleus to and from the cytosol. The envelope is directly connected to the endoplasmic reticulum and is supported by intermediate filaments. The nucleus is surrounded by the cytoplasm inside the cell [70].

2.7.1.7 The cytosol.

The cytosol is a gel like fluid that surrounds the cell organelles. It is confined by the membrane plasma. The cytosol is a mixture of cytoskeleton and dissolved small and large molecules, closely packed and mainly made of water [78].

2.7.1.8 Endoplasmic reticulum.

The endoplasmic reticulum contains a network of branching and joining vesicles that amongst other things are involved in the synthesis of many membrane lipids and proteins. It can be found in two different endoplasmic reticulum patterns, the smooth endoplasmic reticulum and the rough endoplasmic reticulum. The rough endoplasmic reticulum is covered by an evenly spaced arrangement of ribosomal granules and is involved in the production of some plasma membrane proteins [75]. The endoplasmic reticulum that has not bound ribosomes is called smooth endoplasmic reticulum. The smooth endoplasmic reticulum, rich in a wide variety of enzymes, is most common in cells which are involved in the lipid metabolism, such as steroid hormones from cholesterol, triglycerides and lipoprotein complexes [74].

2.8 Fibroblast cells.

The fibroblast is a central component in skin biology. Fibroblasts are responsible for the synthesis and deposition of extracellular matrix required to repair the skin injury. They also communicate through paracrine, autocrine and other forms of communication with nearby cells such as keratinocytes and endothelial cells. Fibroblasts are the most common cells of connective tissue and are involved in functions such as establishing, maintaining and modifying connective tissue. Fibroblasts play an integrative role in the wound repair process interacting with immunocompetent cells and through their regulation of neuropeptides at the site of injury [79]. Fibroblasts appear in virtually every organ of the body. Morphologically, the culture fibroblasts are generally elongated and spindle shaped, however fibroblasts can show a variety of shapes and sizes in culture [79]. In keloids they have been associated with tension and motion on the wound site [23] and fibroblasts seem to be responsible for the high production of fibronectin, elastin and proteglycans and are also responsible for the reduction of the surface area of keloids by contraction [24]. Fibroblasts secrete proteins such

as TGF that stimulate proliferation and migration[21]. Most of the activities carried out during wound reparation are coordinated by chemical signals referred to as TGF or cytokines [1] as described in section 2.5.

2.9 Mechanical Properties of Cells.

Mechanically, cell behaviour is very complex. Some of the normal cell processes require the cell to support forces and deformations similar to solid materials. In other cases cells are required to be able to flow to perform essential functions such as migration and spreading. This paradox means that the cell has to have the ability to behave both as a solid and a fluid material. Such behaviour is reminiscent of soft glassy materials [68]. These materials do not show plastic flow and they behave like a solid until the critical shear stress is exceeded at which point the material flows, behaving as a fluid, showing an inverse relationship between the shear stress and viscosity [80]. This phenomenon has been investigated in references [81-83], by studying the complex shear stress G^* of cells, see Chapter 3 for more details.

The versatile behaviour of cells is attributed to the cytoskeleton because it has the ability to assemble a three-dimensional web of proteins that act like scaffolding giving mechanical support to the cell to behave as a solid. When necessary the proteins diffuse in the cytoplasm enabling the cell to behave as a fluid; this allows the cell to move from one site to another site far away [74].

2.10 Keloid cell mechanical properties.

To date, no experimental work has been published on single keloids cells. However, at the keloid tissue level some experiments have been undertaken in order to understand the molecular factors that influence keloid formation. Keloid scars have been studied intensely from a biochemical point of view, however, from the mechanical perspective most of the studies have been performed on hypertrophic scars. The only mechanical study performed of Keloids has been performed at the macro level; the objective of this study was to determine the mechanical changes of keloids scars treated with intralesional triamcinolone acetonide [63]. The mechanical properties were measured using a commercially available skin elasticity meter suction device (Cutometer SEM, Courrage and Khazaka, Köln, Germany) as illustrated in Figure 2.20.

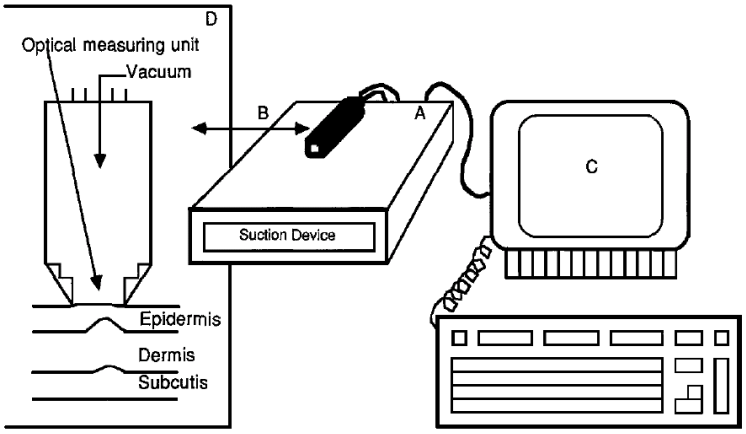

Figure 2.20 Cutometer graphic diagram, taken from [84].

The Cutometer measures mechanical properties of the skin by applying a negative pressure that sucks up the skin scar. The deformation vs Time graph shown in Figure 2.21 is a typical deformation curve for normal skin; Ue is the immediate distension, Uv is the delayed distension, Ur is the immediate retraction and Uf is the final distension. The measurements on keloids showed that scar elasticity was increased with the application of the injections.

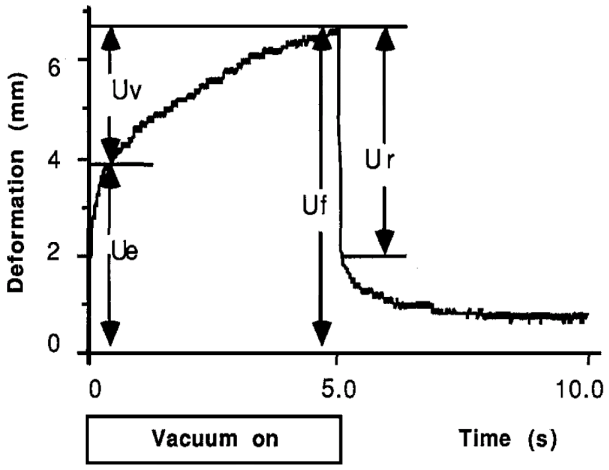

Figure 2.21 Normal skin deformation vs. Time curve, taken from [84].

Chapter 3

Experimental techniques to study mechanical properties of single cells.

3.1 Introduction.

The need to understand the mechanical properties of cells and their relationship with their chemical and biological functions prompted researchers to look for ways to investigate these relationships. This investigation has been particularly difficult due to the small scales and the complexity of the relationships involved in normal cell process lifetimes. One of the first attempts to determine the mechanical properties of cells consisted of stretching a cell between needles or in a centrifugal field or by observing the degree of flattening under gravity [85]. Cole 1932 used a minute gold beam to compress sea-urchin eggs [85] obtaining satisfactory results. Subsequent developments in technologies have resulted in progress; however, there is still much work to be done in this field. Some of the cell aspects investigated cover: changes in mechanical responses in the presence of different chemical substances [81, 86], effects of temperature [87-89], adhesion of cells on different substrates [90-93], mechanism of motility [94], protein forces [95] and viscoelastic analysis [96, 97], etc.

This chapter will describe the existing methodologies that have been utilised to study mechanical properties of cells, grouped by similarities in 6 groups. The first experimental techniques (3.2) considered are the micropipette techniques, where the main component is the glass micropipette that is used in a similar manner to tweezers, the cell is "grabbed" in the end of the micropipette by applying a negative pressure. The second method (3.3) is the optical tweezers, which use a high concentrated light to grab and manipulate small objects. The third method (3.4) are the engineering substrates, the stiffness of the subtracts are used as an indicator of mechanical cell behaviour for example, flexible substrates are used to study the cell focal adhesion. The fourth method type (3.5) are the magnetic methods, in these the magnetic force exerted on ferromagnetic beads imposes forces on the cell enabling mechanical properties to be studied. The fifth group (3.6) corresponds to the AFM which is used in the experimental work carried out in this thesis. It works by using a very sensitive element, a cantilever, which is brought into contact with the sample to apply forces and measure the response to such load. Finally the last group (3.7) corresponds to methods not included in any of the previously mentioned groups.

3.2 Micropipette aspiration.

3.2.1 Introduction.

The micropipette is the most important element in this method. It has been used in two different configurations, single and double micropipette. The cell elastimer is an example of single micropipette, the cell elastimer is used to suck the cell into the micro pipette and then by relating the deformation and negative pressure, it is possible to determine the membrane tension. The double micro pipette can be used in some cases like tweezers by grabbing the cell from two opposite ends and then stretching the cell to finally determine some mechanical properties [98]. The double micropipette can also be used in a different way, with one micropipette used to hold a cell or bead but with the other the cell can move as a piston, so the micropipette is used as a channel through which the cells move freely. This configuration has been used to study focal adhesion [72].

3.2.2 The micropipette.

The micropipette is an instrument commonly used in biology and medicine. It is a relatively simple instrument capable of performing complex tasks, for example, it can be used as a micro electrode and also to perform fluid/substance injection. It has been used in specific areas of research, for example, in intracellular surgery, in the investigation of deoxyribonucleic acid (DNA) and small biological tissues [99, 100]. In the micropipette aspiration method, it is used like tweezers, capable of grabbing cells to manipulate them and measure force deformations with this force being able to be related to mechanical properties. Most of the micropipettes are made of borosilicate, aluminosilicate and quartz [99, 101, 102]. The micropipette was invented around 1904 by Marshall A. Barber [103], a bacteriologist of the University of Kansas School of Medicine. He was the first to make and use glass micropipettes, and was interested in the pathogenesis of a variety of infectious diseases. Barber made micropipettes small enough to be manipulated conveniently in the field of a compound microscope. In 1954 Mitchison and Swann developed an instrument called the "cell elastimeter", which basically consists of a glass micropipette mounted on a micromanipulator which is brought into contact with the cell. A negative pressure is applied to partially suck the cell into the micropipette. The membrane tension is calculated in this type of experiment.

3.2.3 Cell elastimeter.

Mitchison and Swann, in 1954 developed the so called "cell elastimeter" [85] illustrated in Figure 3.1. In essence the instrument consists of a glass micropipette mounted on a micromanipulator and fitted to the end of rubber tubing; the other end of the rubber tubing is connected to a reservoir containing water. The localised movements are visualized with a microscope. The movements of the micropipette are controlled by a micromanipulator which enables movement in three dimensions. It is also possible to move the platform of the microscope in order to place the specimen in the correct position. The suction pressure is controlled by a mechanical system consisting, in essence, of a screw. This system controls the vertical position of the tank with a resolution of $0.1 - 0.2\ pN/\mu m^2$ [104].

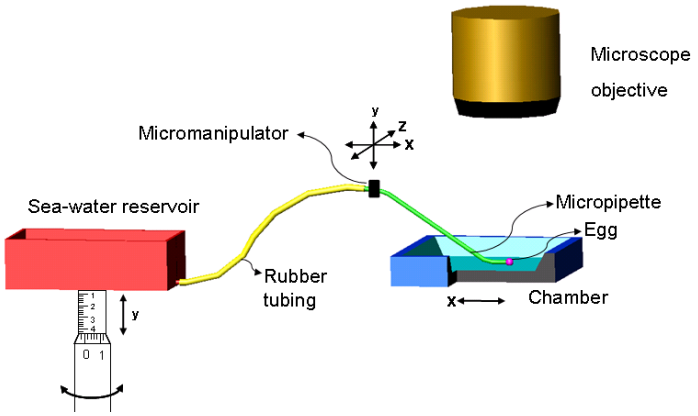

Figure 3.1 Cell elastimeter main components.

The operation of the elastimeter is as follows, the cell is brought into contact with the micropipette tip, a negative pressure is applied later and the cell is sucked into the pipette. The tension membrane is then determined by analysing the geometry of the sucked cell (see Figure 3.2).

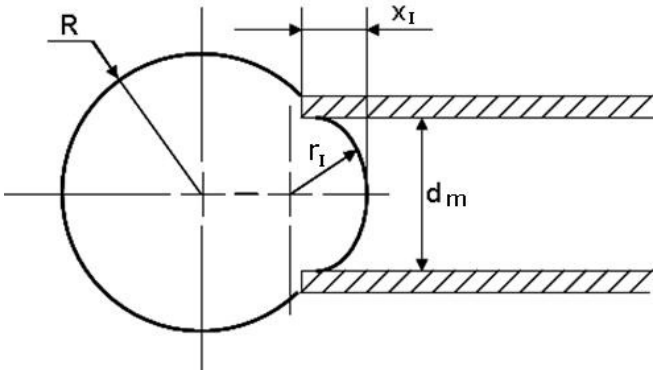

Figure 3.2 Schematic representation of the egg and the pipette after application of the negative pressure, showing the main dimensions taken into account to determine the rheological properties as a simple tension problem.

The above figure shows the main dimensions used to determine the rheological properties, d_m, diameter of the micropipette, R, radius of a sea urchin egg, r_I radius of the intrusion into the pipette due to the increment of the pressure and x_I is the intrusion distance; all these dimensions are measured by a microscope.

Assuming the problem is that of simple tension, therefore the corresponding model is shown below:

$$P = 2T_m\left(\frac{1}{r_I} - \frac{1}{R}\right) \tag{3.1}$$

$$r^2 = \left(\frac{1}{2}d_m\right)^2 + (r_I - x_I)^2 \tag{3.2}$$

$$r_I{}^2 = \frac{1}{4}d_m{}^2 + r_I{}^2 - 2r_I x_I + x_I{}^2 \;\therefore\; r_I = \frac{\frac{1}{4}d_m{}^2 + x_I{}^2}{2x_I} \tag{3.3}$$

$$\text{So that } p = 2T_m\left(\frac{2x_I}{x_I{}^2 + \frac{1}{4}d_m{}^2} - \frac{1}{R}\right) \tag{3.4}$$

The hydrostatic pressure (P) is known (P is dependent on the height of the reservoir) and the rest of variables are measured by direct dimensioning using the microscope, enabling the tension in the membrane (T_m), to be determined.

The problem was initially resolved considering the membrane as an elastic body however, later the problem was studied by considering that the surface of the egg behaves like a rigid membrane [85].

3.2.4 Modifications of the cell elastimeter.

Several problems were found in the cell elastimeter, such as evaporation of liquid in the tank and control of tank elevation which resulted in uncertainties in the pressure controls. In order to minimise this problem the pressure control system was modified adding a fine pressure control and the reservoir was closed to avoid evaporation, also the visualisation and micropipette diameter were improved as illustrated in Figure 3.3.

In 1993 the system was used to study the mechanical properties of isolated plant protoplast membrane (secale cereale L. cv Puma) [105] in order to understand the affectation by freezing injury (see Figure 3.3). In this system the pressure is generated by a coarse pressure control and a fine pressure control, and a manometer was added to monitor the pressure, enabling a greater control of the pressure.

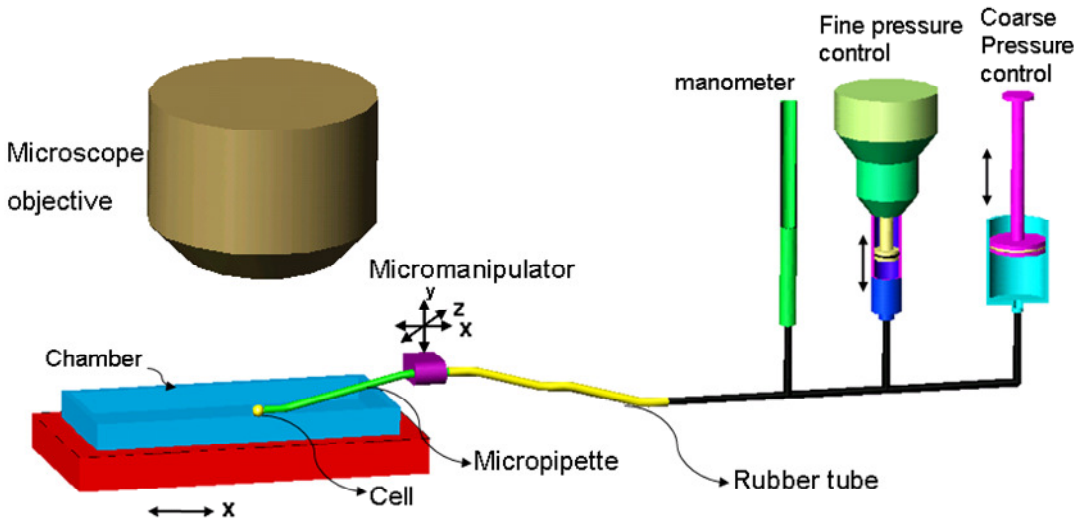

Figure 3.3 Arrangement of the modified system.

The tension of the membrane in this case was determined using expression (3.5):

$$\gamma = -\frac{P}{2/(r - \frac{2}{R})} \tag{3.5}$$

Where R is the radius of the cell, P is the negative pressure, r is the radius of the deformed cell (Figure 3.2).

A single micropipette was also used by Schmid-Schönbein [106] to study passive mechanical properties of human leukocytes, a standard solid viscoelastic model was found to describe leukocytes deformation for small strains. Waugh et al. [87] measured the elastic properties of red blood cells as a function of temperature. Thoumine et al. [94] used a novel dual micromanipulation device consisting of a micropipette and glass microplates on which chick fibroblasts were allowed to attach to the surface, then the free end was aspirated into the micropipette. Additional examples of the use of micropipettes can be found in [104, 107]

3.2.4.1 Double micropipette modifications.

In 2003 a tensile test system was used by Miyazaki et al. [9] to determine the tensile properties of vascular smooth muscle cells (VSMCs) using a pair of glass micropipettes operating like tweezers. This device consists mainly of two micropipettes coated with biological adhesive that grab the cell by the action of

both the biological adhesive and the negative pressure in the micropipettes. One of the micropipettes is fixed and the other one is movable, enabling the cell to be stretched (see Figure 3.4).

The cell is stretched between the two micropipettes. The micropipettes are coated with a cell adhesive and cells resist being deformed. The micropipettes are deformed and a cantilever sensor attached to one of the micropipettes measures the deflection.

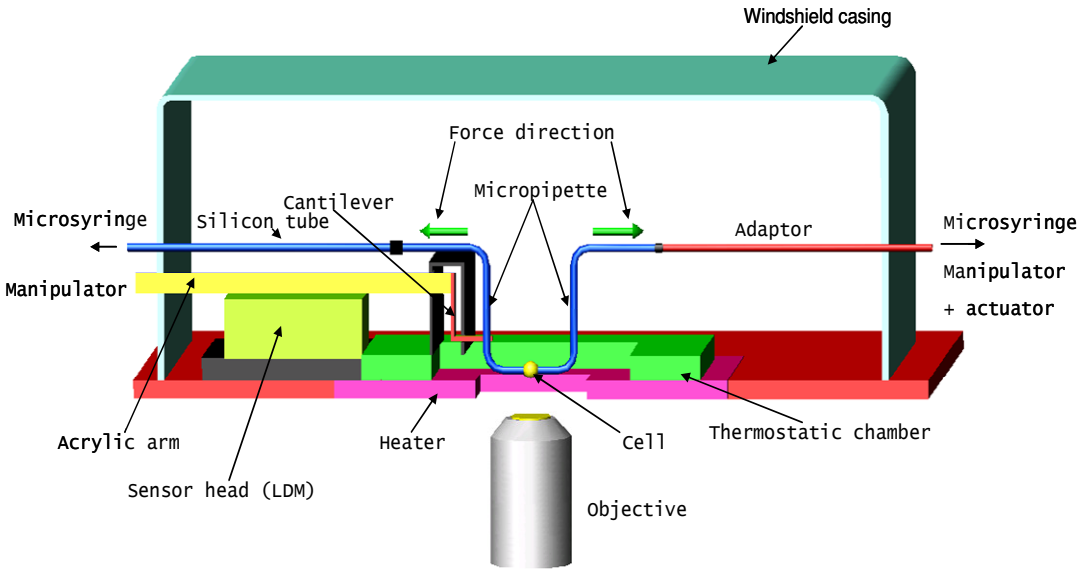

Figure 3.4 The micropipette test was undertaken using the arrangement shown in the diagram, the cell is grabbed between two micro pipettes, the micro pipettes are pulled and the cell is stretched, a cantilever is connected to the micropipette and the stress is determined.

In this method a relatively large portion of the cell goes into the micropipettes and because of this the stretch behaviour is just the behaviour of a part of the cell (see Figure 3.5). In particular, in this experiment the use of biological adhesive helps to reduce the pressure in the micropipettes and reduces the quantity of cell that goes into the pipette.

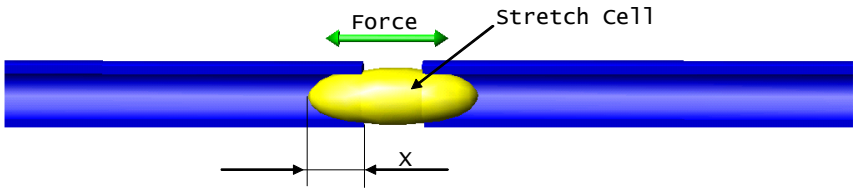

Figure 3.5 Showing a cell stretched between a pair of micropipettes.

The applied force to deform the cell is determined by a cantilever sensor that first senses the deflection of the micropipette which is then used in expression (3.6) to determine the applied force F.

$$\delta = \frac{FL^3}{3EI} \tag{3.6}$$

where, δ is deformation, F is force applied, L is perpendicular distance between the force and fixed area, I Inertial momentum, E elasticity modulus.

Another variation of the micropipette aspiration method has been used by Shao et al. [108], in which a pair of micropipettes is used to measure adhesion forces and tether formation in membranes. In this modification two micropipettes are used, one is used to fix a bead which is normally coated with a particular cell adherent; this bead is slightly bigger than the diameter of the micropipette in order to avoid the bead moving into the micropipette. In the other micropipette a cell is used like a piston, being moved forward-backward by the variation in the pressure (see Figure 3.6). The cell in this case is the same size as the micropipette or smaller than it, enabling an almost free movement due to the change in pressure; the variation in the velocity is used to measure the attached and the tether interaction (see Figure 3.6c, tether illustration).

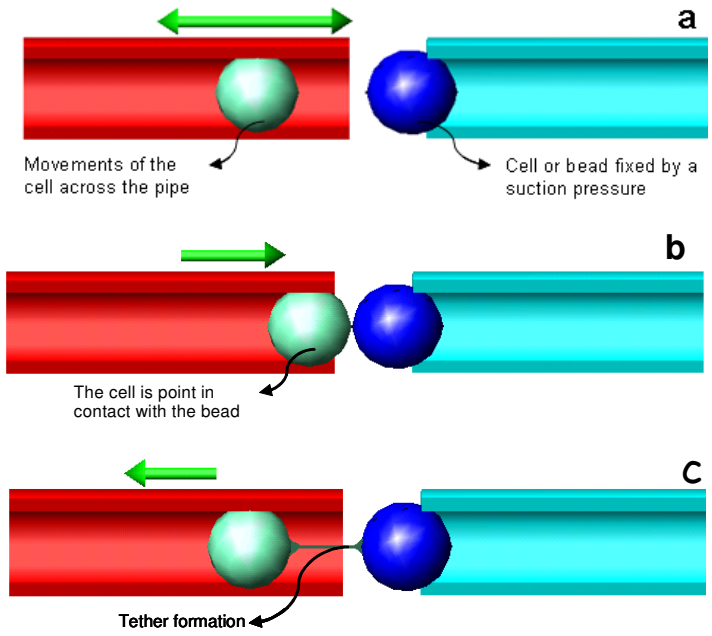

Figure 3.6 Arrangement of micropipette to test cell adhesion and tether. a) the cell is relatively free to move across the micropipette due to the changes in the pressure. b) the cell is brought into contact with the bead, c) the cell moves away from the fixed bead.

The force due to adhesion is given by the equation:

$$F = \pi R_p^2 \Delta p \tag{3.7}$$

Where, R_p is the radius of the pipette, Δp is the suction pressure determined by the hydrostatic head of a water-filled reservoir.

The tether force is given by:

$$F = \Delta p \pi R_p^2 (1 - \frac{U_t}{U_f}) \tag{3.8}$$

Where, U_t is the velocity of the tethered cell, U_f is the velocity of the freely moving cell.

This experimental technique enables the investigation of focal adhesion, adhesion between cell-cell and/or cell-synthetic materials because it is possible to fix different material; it also enables the investigation of the influence of chemical substances in the focal adhesion.

3.3 Optical tweezers.

3.3.1 Introduction to optical tweezers.

In the early 1970 Arthur Ashkin [109], a pioneer in the field of laser-based optical trapping, demonstrated that optical forces have the ability to trap small particles, the trapped particle can then be manipulated as the light is moved, and with the use of a suitable instrument, optical tweezers, the forces and displacements can be measured. The forces that the instrument is able to measure are in the range of 0.1-200 pN and the displacements in the range of 4 nm. In principle, optical tweezers were able to be used to manipulate and study the properties of small dielectric particles. Over recent years it has become an important tool for performing a wide range of studies in biology and other fields mainly due to the fact that the tool is able to measure displacements and forces with high precision and accuracy.

At the present time optical tweezers are being increasingly used to perform mechanical tests; other applications include for example, in colloidal research to manipulate live bacteria and viruses [110]. For a recent review of the advances, calibration and design consideration of optical tweezers [110], and for biological applications in particular, see reference [5].

Optical traps have made possible the manipulation, and experimentation of DNA, as well as enabling some of properties of DNA to be described, in a way that has not been possible before. Detailed knowledge of individual interactions between molecules is essential for understanding the complex mechanisms involved in the real biological processes [111], used in the study of the inhibition of viral adhesion to cell surface [112], as well as mechanical properties of the single molecules of DNA and RNA [113-118].

3.3.2 Principles of the optical tweezers.

Optical tweezers use the radiation pressure to trap small objects, with the source of the radiation pressure being provided by a laser light. The light delivered has an intensity given by a Gaussian distribution, which means that the intensity of the beam is higher in the centre of the spectrum and lower around the borders (see Figure 3.8).

A laser beam first passes through a set of lenses and controls that act like a polarizer, then passes through a high numerical aperture objective lens and finally the highly concentrated light is sent to an object with a high refractive index n_o. The beam suffers a change in the direction when it crosses the object due to its refractive index, the photons suffer a change of the momentum producing a force given by Newton's second law [5] (Equation 3.9).

$$\vec{F} = (\frac{n}{c})\iint(\vec{S}in - \vec{S}out)dA \tag{3.9}$$

Where, $\vec{F}$ is the force due to refraction, n the index of reflection, $\vec{S}$ momentum flux of photons, $\vec{S}in$ direction of the light in, $\vec{S}out$ direction of the light out, c the velocity of the light. The objects to be manipulated are generally very small objects, for instance silica and polystyrene beads (micro size dielectric particles).

The angle of incidence of the beam changes due to the difference in density depending on the difference of the refraction index of the surroundings and the bead index (see Figure 3.7). This change in the direction of the light generates a force due to the change of momentum of light.

In some procedures the silica or polystyrene bead is the trapped element that is also attached to the specific object being studied such as a cell and DNA etc, also it is possible to trap directly the study sample, for example it is possible to trap and manipulate a cell directly using a laser trap, using an infra red light to avoid damage to the biological samples [111, 119].

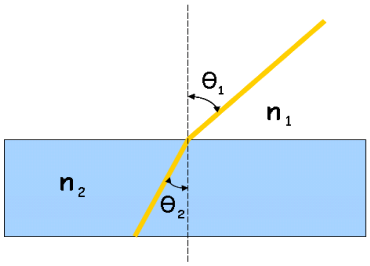

Figure 3.7 The angle of incidence is different to the angle of refraction.

The change in the direction of the force is expressed in Equation (3.9), the variation of the force is determined by the differences in the refraction index, and this variation of direction produces the force necessary to trap small objects.

3.3.3 Optical trapping.

Small spheres are used in optical trapping. The effect of the photons when they interact with an object is called radiation pressure; it can be separated into two rectangular components: the scattering force F_{scat} and the gradient force F_{grad}, the second one is the one responsible for the optical trapping (see Figure 3.8).

The stable trap is reached theoretically when the vector F_{scat} is equal to F_{grad}; which means that the two forces are in equilibrium. In terms of the relationship between the two, $R_r = F_{grad} / F_{scat} = 1$, this condition is theoretical, in practice R_r greater than 1 is required, for example for polystyrene latex spheres in water $R_r \geq 3$, where the particle diameter is $D \leq 95\ nm$ under the specific characteristics of a longitude of wavelength and a Gaussian beam of focal spot size [120].

Not only is it possible to trap small objects with this instrument, it is also possible to determine the forces, quantitatively. The force is related to the displacement of the bead by the following expression:

$$\vec{F} = -k_T \cdot \vec{x} \tag{3.10}$$

Where, k_T is the trap stiffness, $\vec{x}$ is the distance between the bead centre and beam focus (see Figure 3.8).

These parameters are used to calibrate the trap.

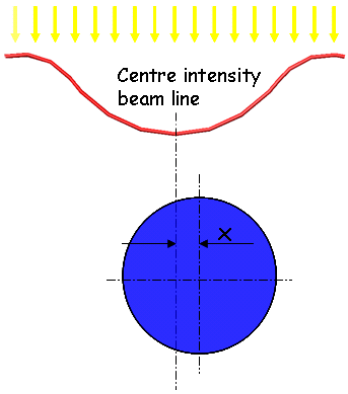

Figure 3.8 The distance between the centre intensity beam line and the centre of the beam is express by x.

3.3.3.1 Single beam trap.

It is possible to trap biological samples with a single beam, which can be configured to trap different samples, for example DNA and cells, enabling the mechanical testing of samples. One of the arrangements that can be used to study mechanical properties is illustrated in Figures 3.9 and 3.10. This arrangement is used to trap DNA, one end is attached to the glass coverslip and the other end is attached to the bead, the bead can be manipulated to perform the mechanical test.

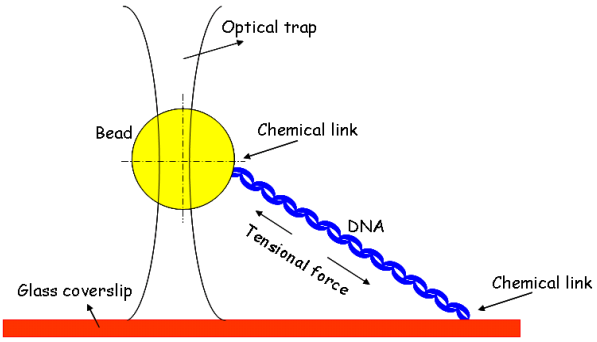

Figure 3.9 Single trap [118, 121].

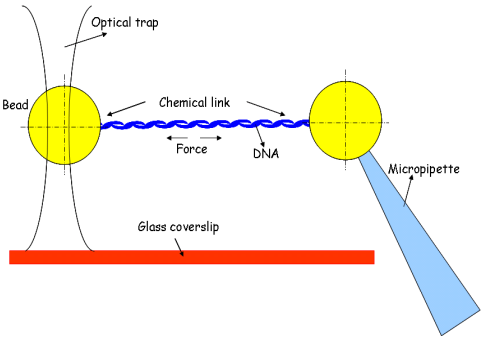

Figure 3.10 Single trap and micropipette combination [114].

3.3.3.2 Double beam trap.

In Figure 3.11 a red blood cell (erythrocyte) is stretched between two optical traps. This particular test was performed to study the mechanical properties of malaria infected cells at different stages of the illness; the optical traps used in this test are able to produce stretch forces with a maximum force of 190 pN [122] also this arrangement of double laser beams can be used to stretch DNA attaching DNA at opposite ends beads and then applied a small force to deform the DNA chain Figure 3.12 [114, 117, 118] .

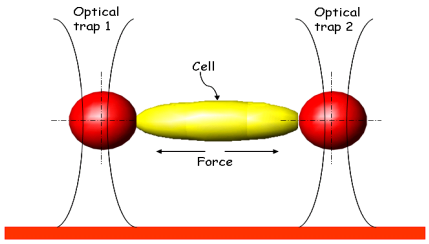

Figure 3.11 Optical trap control: silica beads are attached to opposite ends of the cell [122, 123].

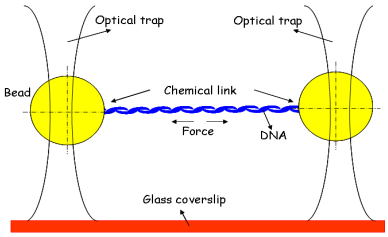

Figure 3.12 A double optical stretching of a DNA molecule [114, 117, 118] .

A double optical trap (Figure 3.13) can also be used to stretch a cell (optical stretcher). In this process an infra red laser is used to minimise damage to the cell as much as possible [124].

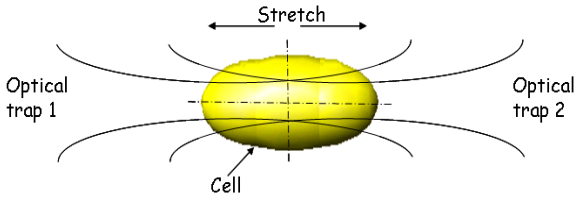

Figure 3.13 A double optical trap stretching a cell.

3.4 Engineering substrates.

3.4.1 Introduction to substrates.

Substrates have been used to understand many phenomenon such as motility, signal transmission, mechanical traction, focal adhesion, analysis of the mechanisms by which the cells respond to mechanical signal and the transmission of this information to others cells (intercellular signal) without physical contact occurring between them [91, 125, 126]. The advantage of focal adhesion is that islands of different shapes are created and it represents an interesting tool to perform tests which make it possible to study the influence of the shape of substrates.

There are many substrates that have been used such as, polymer gels, polymer films, elastomeric substrates, glass, polystyrene and silica. Some specific properties of substrates, such as stiffness, flexibility or transparency may prove most advantageous for some experiments [90].

In many studies of substrates an extra cellular matrix (ECM) is used. This is a "substance" to which the cell adheres to. It is generally spread and/or stamped on a substrate to control the shape cell adhesion and to study the areas in which focal contacts or focal adhesion occurred. This plays an important role in the regulation of the actin organization, and thus affects spreading, morphogenesis and migration [127].

This kind of surface can be made using different techniques, for example, soft lithography, conventional lithography and self ensemble technique [128, 129]. These surfaces are normally coated with an extra cellular matrix (ECM), and cell or cells are positioned on the surface. The focal adhesion forces normally deform the substrate, this deformation can be measured and the force applied on the surface substrates calculated.

3.4.2 Fabrication of poly(dimethylsiloxane) stamp (PDMS).

The PDMS is used in the fabrication of flexible patterns and to stamp ECM on substrates. A negative pattern (Figure 3.14a) is first transferred to a photoresist layer (Figure 3.14b), the transference is carried out using UV light, the pattern printed on the photo resist layer can be observed in Figure 3.14c, in this figure

the dark area is the transferred pattern, in a later step the photoresist is developed and areas which aren't protected by the mask are removed Figure 3.14d. Finally, using it as a negative mould a PDMS material is deposited Figure 3.14e and polymerised to obtain the final PDMS stamp Figure 3.14f.

PDMS moulds are utilized in the reproduction of flexible substrates, and also they are used to stamp extracellular matrix (ECM) on different substrates (flexible and non flexible), to a determined geometry. In the case of ECM, it is spread on PDMS mould and later transfer to substrate. One of the advantages of the PDMS moulds is the possibility of creating different patterns and shapes (squares, triangles circles, lines etc) [16, 130].

3.4.2.1 Pattern substrates.

In micropattern substrates, different techniques such as photolithography are used to build the patterns [16]. As Figure 3.15 shows, it is possible to achieve many geometries. The diagram shows how a poly-dimethyl siloxane (PDMS) pattern is obtained using photolithography. This PDMS pattern can also be used to make further patterns if it is used like a stamp (see Figure 3.15).

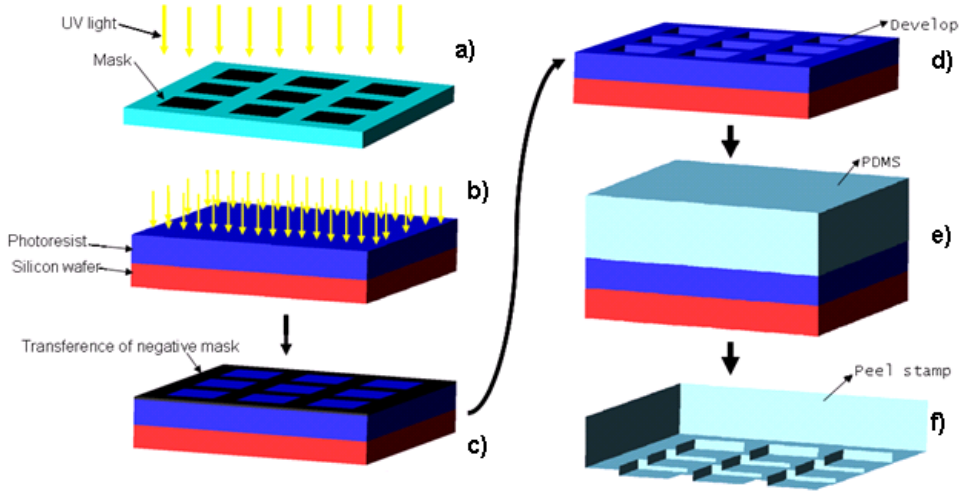

Figure 3.14 Process to obtain a PDMS pattern.

3.4.2.2 Rigid substrates.

A good example of a rigid substrate is the micropatterned substrates coated with adhesive islands of ECM. For instance, Brock A. et al. 2003 [17], created an ECM pattern on a non-adhesive substrate with different shapes. In this case all of the geometries had the same area and the relationship between the geometry of the

ECM and the directional motility was analyzed. The results revealed that the cell has the capacity to sense the geometry [17] see Figure 3.15.

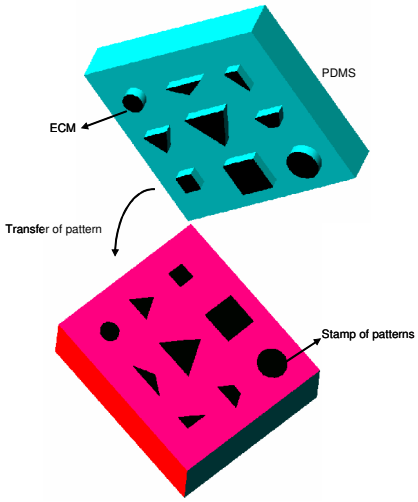

Figure 3.15 Transference of an ECM pattern from PDMS to mould.

Focal adhesions are therefore also the sites at which forces are transmitted to the substrate. They can be detected as dark areas in interference reflection microscopy [126], with an electron microscope, with fluorescent labelling or by using specific adhesion molecules such as vinculin, paxillin and integrins. It has been recently shown that tension "reinforces" focal adhesion, which is stimulated after the application of external forces [126].

3.4.2.3 Flexible substrates.

Dembo et al. [18] mention that Harris et al. 1980 [131] and Harris 1988 [132] first had the idea to use elastic substrates. Flexible substrates such as silicones, gels and rubbers, polyacrylamide [19] etc, have been employed. Forces are applied by adherent cells on the substrate on which they sit. Due to these forces, the substrate is deformed, and this deformation is an indication of the quantity of force exerted by the cell. The measurement of the force should be as accurate as possible, because the interpretation of the deformation depends upon this information. An important step in this technique is the calibration of the substrates.

In the case of flexible substrates the pattern is used as reference for the displacement (see Figure 3.16) in which the rows show the deformation of the substrates due to the cells tractional force. A contractile apparatus of the cell is anchored to the substrate and the substrate is deformed [126]. The deformation

of the substrate can be measured, and this deformation can be related to force that the cell exert on it.

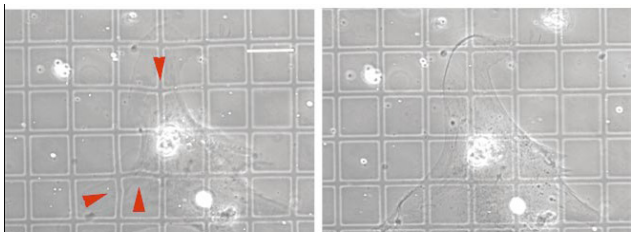

Figure 3.16 Substrate deformation, figure taken from [126].

3.4.2.4 Substrates with embedded particles.

In this case polymeric substrates are fabricated with a special characteristic; this characteristic is that the substrate contains fluorescent beads distributed along the substrate (see Figure 3.17). This method is similar to the pattern substrate; the flexibility is the properties used to perform the test. The cell exerts forces on the substrate and the beads are displaced, the displacement of the beads is video recorded, then the images filmed are digitalized, for example in Figure 3.18 the displacements are shown mapped by vectors.

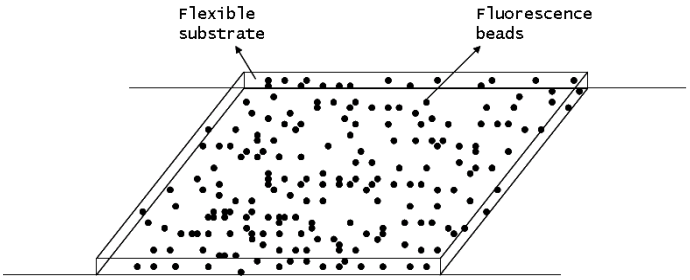

Figure 3.17 Embedded particles in substrate.

The calibration of the substrate is the same as that used in the pattern technique.

Maps generated with this technique are useful in understanding that the force exert onto each bead is translated into a displacement. The force is represented by a vector and a map of force is built (see Figure 3.18).

Cells are allowed to adhere onto the substrate and the forces generated by the cells deform the substrate causing the displacement of the beads. Images of the deformation are recorded, then the cell is released and the images of the substrate without deformations are recorded. Finally with the combination of

both images are possible to build force maps, the initial position of the beads (undeformed substrate) are the origin of the vector and the final position of the beads (deformed substrate) are the head of the vectors (see Figure 3.18).

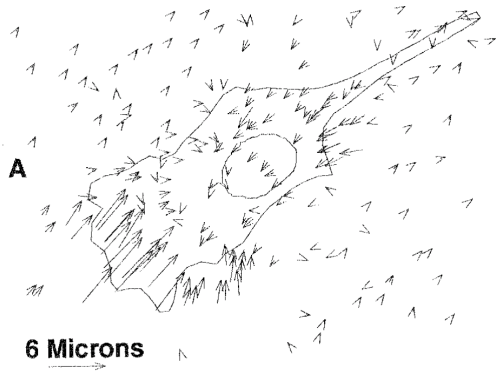

Figure 3.18 Vectors of force, figure taken from [18].

3.5 Magnetic methods.

3.5.1 Introduction.

Electrical currents are generated in the human body as a product of some internal organ processes for example, the heart and the brain. In such cases the relationship between magnetic fields and electric currents can be explored. For example in neurology magnetic signals have been used to generate images or maps of human brain activity [133], and in cardiology electrical currents are used to diagnose heart disorder, and in lungs studies have been carried out to study contaminants.

Magnetic methods are based on a physical property called magnetism. Magnetism is a property of materials that consists of a force with the capacity to attract or repel ferromagnetic materials. Some materials exert easily detectable magnetic properties like iron, nickel and cobalt; in other materials the magnetic force may be weak; nevertheless all materials are influenced by the magnetic field. To date this technique has mainly been employed to study mechanical properties such as focal adhesion [134], elasticity [81], changes in mechanical properties such as stiffness, viscosity in response to stimuli [96], transduction and mechanical sensing of forces by integrins [97, 135] and the study of viscous elasticity in human airway smooth muscles (HASM) [96] in response to treatment with N^6, 2'-O-dibutyryladenosine 3',5'-cyclic monophosphate (DBcAMP), cytochalasin D and histamine.

After the initial experimental investigations, the further development of technology enabled more accurate measurements and better analyses using this technique. Also, some novel tools were subsequently employed to improve the technique. Tools such as the video recorder filmed the test and opened up the possibility of subsequent analysis and measurement of the bead displacements [136] and micromanipulators helped to improve the control of the magnetic material. In some cases, optical tools are not required because the measurements are made by analysing the residual magnetic field, using special equipment that is able to perform the function of determining the angular displacement by analysing the residual magnetic field [6].

3.5.2 Magnetic twisting.

'Twisting tests', also known as magnetic twisting cytometry (MTC) consist of a magnetic field being applied to cells containing magnetic particles. The magnetic field is oscillated in a circular movement in the horizontal plane for specific periods, as illustrated in Figure 3.19. In order to measure the rotation of the magnetic bead, pictures are taken at different time periods or a galvanometer can be used to measure the magnetic field and the rotation angle can then be calculated, this experiment has been used to study mechanical properties of cell membrane and cytoskeleton studies [6, 137].

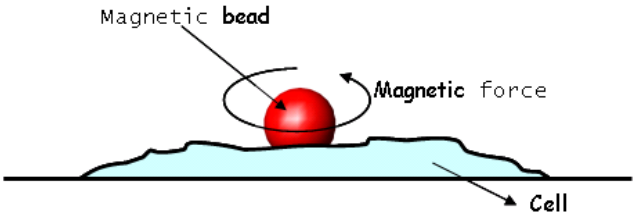

Figure 3.19 Magnetic twisting: a partially phagocitose cell and the magnetic field direction.

3.5.3 Magnetic dragging.

The cells are prepared in the same way as for magnetic twisting, however, the main difference from the twisting test is the transversal movement of the magnet (see Figure 3.20), that is a linear movement in parallel with the microscope platform on which the sample is sitting.

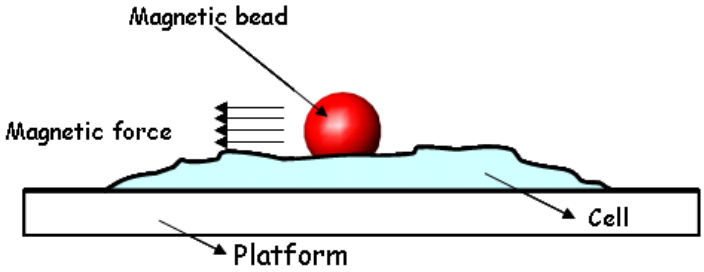

Figure 3.20 Magnetic dragging.

3.5.4 Magnetic prodding.

In this case the magnetic field is used to poke the cells with the beads as illustrated in Figure 3.21.

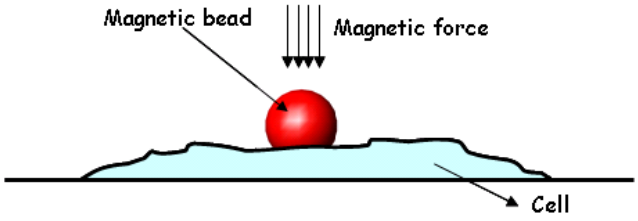

Figure 3.21 Magnetic prodding: the bead is pushed onto the cell.

3.6 Atomic force microscope (AFM).

3.6.1 Introduction.

Over the past decade the AFM has emerged as a useful tool. This equipment has been used to study a wide range of materials such as composites, glasses, metals, polymers, electronics, membranes, films, synthetic ceramics, composites and biological organisms, in numerous fields such as, automotive, aerospace, chemical, material science and biology, etc. Particularly in the biology and biomedical areas, the AFM has emerged as a new and versatile instrument.

The AFM or scanning force microscope (SFM) belongs to the family of scanning probe microscopes (SPMs), that are based on the scanning tunnelling microscope (STM). It was invented by Gerd Binnig and Christoph Gerber in 1986 [20], and it is able to reproduce images of the surface of conducting and non-conducting materials [138] to molecular and in some cases atomic resolution. It can also measure forces at the pico-Newton scale at the level of a single atom [139]. It can be utilized in aqueous environments [140], and to perform studies of

phenomena such as electrode position [141], wear resistance [142], surface roughness [143, 144], lubrication [145], corrosion, nanotribology [146], and adhesion. Specifically in biology, it has been used to study nucleic acid, receptor-ligand complex, the molecular interactions determining the stability of single proteins and to understand the elastic and viscous properties of membrane proteins using dynamic modes [147], and has been extended to probe the dynamics of single molecules, including polysaccharides. Also it is used to determine properties such as adhesion and electrostacity [95].

The AFM has become one of the most popular tools to image biological objects with sub wavelength resolution. It should be mentioned, however, that visualisation of biomolecular interaction processes in situ is not as straight forward as the visualization of fixed structures [148].

3.6.2 Principles of the AFM.

The AFM does not use lenses, it is an instrument used to reproduce the topography of samples by scan-raster, a very sharp tip mounted on a cantilever supplying information in three dimensions. The tip is located in "contact" (see operation modes 3.6.4.5) perpendicular to the surface of the sample, then depending on the AFM design, scanners are used to translate either the sample under the cantilever or the cantilever over the sample (see scanner 3.6.4.4). In both cases, the tip covers the area of interest and according to the topography of the sample the beam is deflected following up and down the contour of the sample; its deflection is sensed and the information gathered due to the deflection can be used to reproduce a topographical model of the sample. AFM is not only used to construct models, it is used to study interaction forces, especially in biology, for example DNA-protein interactions [149], visualization of cell chromosomes during mitotic phases in a chinese hamster ovary cells [150] and to measure forces involved between single molecules, measurements of mechanical properties of the sample and detection of protein motion [151], etc.

3.6.3 Components of an AFM.

The equipment used in the experiments described in this thesis is a Scanning Probe MultiMode™ (SPM, Veeco metrology group). It is formed by two control units, a NanoScope™ and a PicoForce™ which allow the instrument to operate in

different modes. This unit is capable of scanning 175 μm in size (see Figure 3.22).

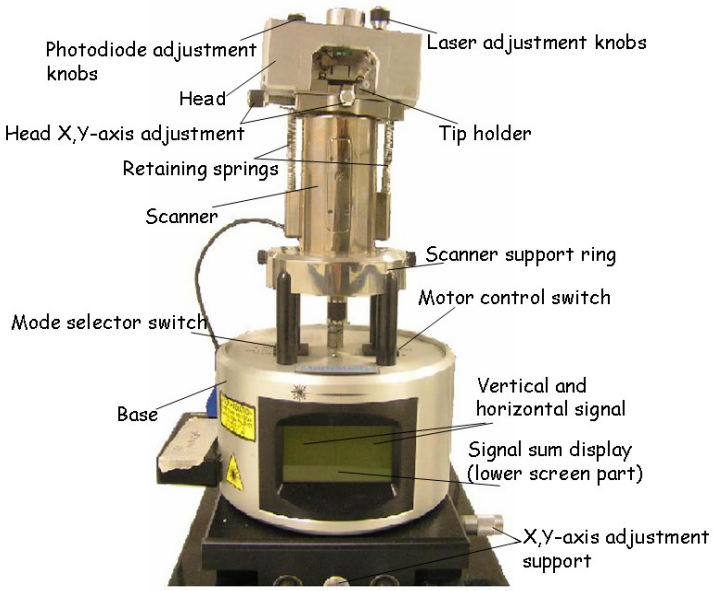

Figure 3.22 Multimode SPM.

Some of the main components of the microscope are listed below:

3.6.4 The optical head.

The optical head is a block attached to an X, Y stage displacement platform. Figure 3.23 below shows a picture of the head and the internal and external elements including the laser, mirror and photodiode, and the path way that follows the diode from the laser until it reaches the photodiode (see Figure 3.23). Inside the block, in the upper part, the laser (**1**) is located, and on the left is the photosensor (**5**). The knobs are used to obtain displacement to the desired location (head X,Y- axis stage adjust), also to move the laser and focus on the cantilever (laser X,Y-axis adjust) and finally a pair of knobs are used to adjust the signal on the photodetector (Photodiode adjust).

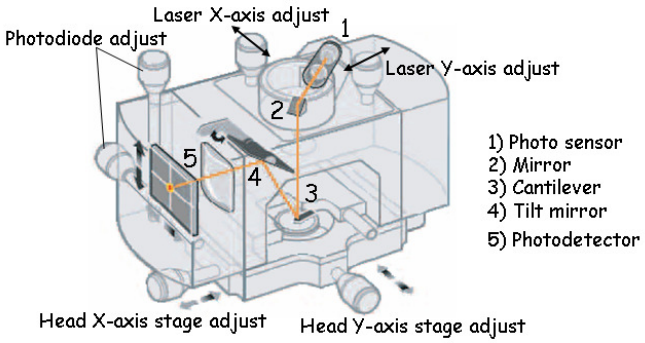

Figure 3.23 Details of the optical head of the AFM.

3.6.4.1 Tip.

The tip (Figure 3.24) was traditionally made of diamond on a gold film, but nowadays most are made of Si_3N_4 or Si with a radius of approximately 10 nm. The tip is the heart of the AFM, it is very important for the success of the technique as it must accurately reflect the surface features of the specimens under investigation. The image is constructed by scanning the sample with the tip, therefore the selection of tip plays an important role in the obtaining of an accurate surface topography. The tip is attached to a cantilever Figure 3.24, giving the tip freedom of movement. Depending on the topography of the sample; the displacements of the cantilever can be vertical and/or torsional, examples of different tip cantilever can be seen in Figure 3.25.

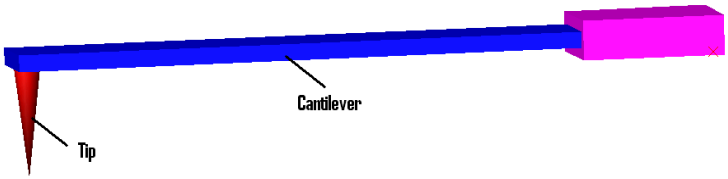

Figure 3.24 Tip mounted on a side of the cantilever.

The commercial tips available are made using different techniques and materials, including micromaching, lithographic photo-masking, etching and vapour deposition, etc. In addition, the tip can also be one of a number of different shapes for instance a parabola, pyramid, truncated pyramid, tilted pyramid, and cylinder, and with a specifically characteristic chemical or biological coating. There are still a number of long-standing problems in obtaining consistent high-resolution images using AFM. The radius and shape of the end of the AFM tip can vary resulting in a loss of sharpness [152, 153].

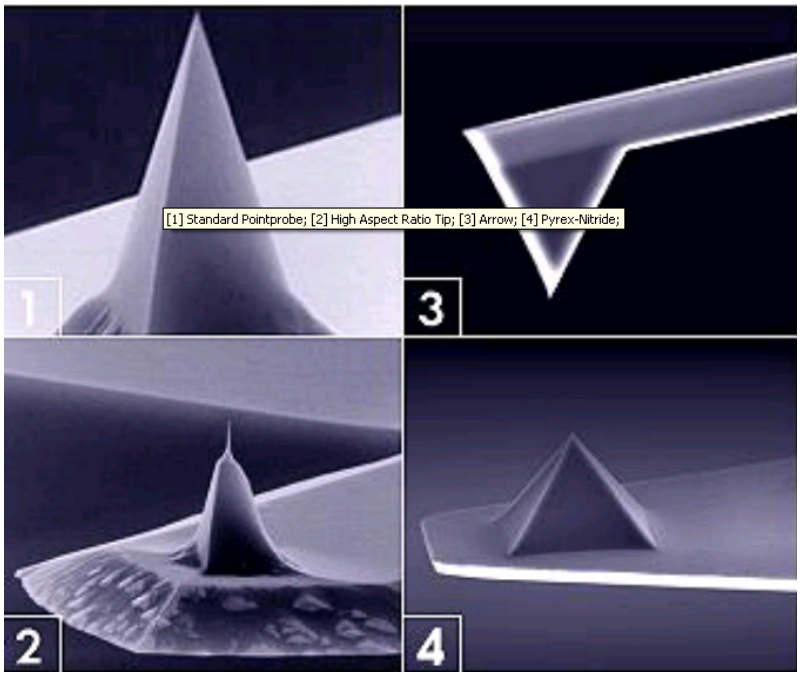

Figure 3.25 AFM cantilever probes, 1) Standard Pointprobe®, 2) High Aspect Ratio Tip. 3) Arrow™, 4) Pyrex-Nitride™ Electron micrographs by Jean-Paul Revel, Caltech. Tips from Park Scientific Instruments; super tip made by Jean-Paul Revel. Figure taken from http://www.nanoworld.com.

3.6.4.2 Cantilever deflection sensor.

There are different cantilever sensors available such as, vacuum tunnelling [154], capacitance [155], optical interferometry [156] and optical lever [157]. In this kind of system it is necessary to use an external system to measure the deflection; in the case of piezoresistive [138] and piezoelectric [158] the deflection is measured directly from the sensor.

The optical lever is the most common mode of detecting deflection. In this case a laser light is sent to the end of the cantilever; this beam is reflected onto a photosensor (photodiode); the changes in the intensity of the light due to the deflection and/or torsion of the cantilever are sensed and this information is processed by a translator. Different systems are interconnected to coordinate the function between them, and this interconnection forms a loop to coordinate the operation, enabling the AFM to operate in different modes (see modes of operation).

3.6.4.3 Photosensor.

A photodiode is a semiconductor diode that functions as a photodetector. It is used to sense the vertical (deflection) and lateral (torsion) displacements of the

cantilever. A segmented photodiode is commonly used to sense the changes in the intensity of the light between the segments produced by the vertical and lateral movements. The photodiode detector senses the variations of electrical signal, which are transformed into displacements which themselves can be transformed into forces.

Photodiodes may have a double segment or four segments:

Two segment photodiode: A two segmented photo diode is formed by two segments as its name indicates (see Figure 3.26). The light is reflected onto segments 1 and 2 and its intensity changes due to the displacement of the cantilever. This photodiode is commonly used to sense vertical displacement (deflection) of the cantilever.

Four segment photodiode. The four segment photodiode (Figure 3.27) performs the same task as the two segment photodiode but has the capability of sensing lateral displacement (torsion); normally this photodiode is used in the frictional mode [151].

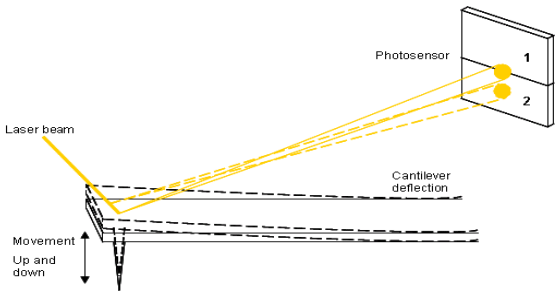

Figure 3.26 Two segment photosensor.

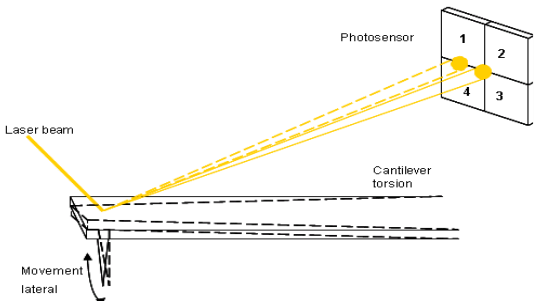

Figure 3.27 Four segment photosensor.

3.6.4.4 Scanner.

The scanners are made of a piezoelectric ceramic that is radially polarized. Electrodes are attached to the piezomaterial, and movements are achieved by applying a high voltage over the electrodes located around the material. Movement is possible along the main axis, X, Y and Z, by applying a voltage on the desired axis and following this, the piezoscanner is expanded in the required direction. The piezoelectric scanner allows three-dimensional movement controlled by the electronic feedback.

The scan function can be generated by the movement of the cantilever on the sample (cantilever scanner), or the movement of the base in which the cell is placed (tube scanner), but in both cases a piezoelectric material is used.

The tube scanner. The most common scanners consist of a platform that is attached directly onto the piezoelectric material (see Figure 3.28), the sample is positioned on the platform, which moves the sample along the X, Y and Z axis.

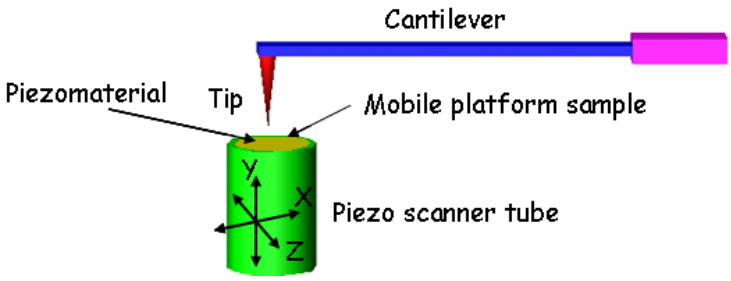

Figure 3.28 The tube scanner configuration, the piezomaterial allows movement in three-dimensions; the cantilever is fixed in one of its extremes and the sample in this case is moved in order to be scanned.

The cantilever scan. In this case, the platform is fixed. The cantilever is moved along the X, Y and Z axis by the piezoscanner to which the cantilever is fixed (see Figure 3.29). However in both cases the area of the sample is covered.

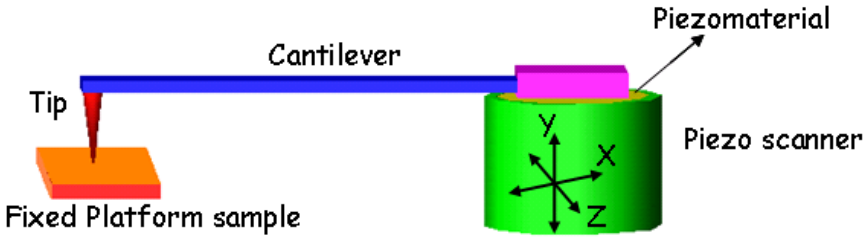

Figure 3.29 The cantilever is moved to scan the sample that is fixed on the platform.

3.6.4.5 AFM operation modes.

Contact mode. In this case the tip scans over the sample surface and can therefore damage the sample if the sample is made of a soft material. The tip is brought towards the sample, (the cantilever is undeflected), it starts to experience an attractive force and the cantilever is deflected. If the movement continues towards the sample, the tip experiences a repulsive force. The force on the tip is dependent of the distance between the cantilever and the sample [151] (see Figure 3.30).

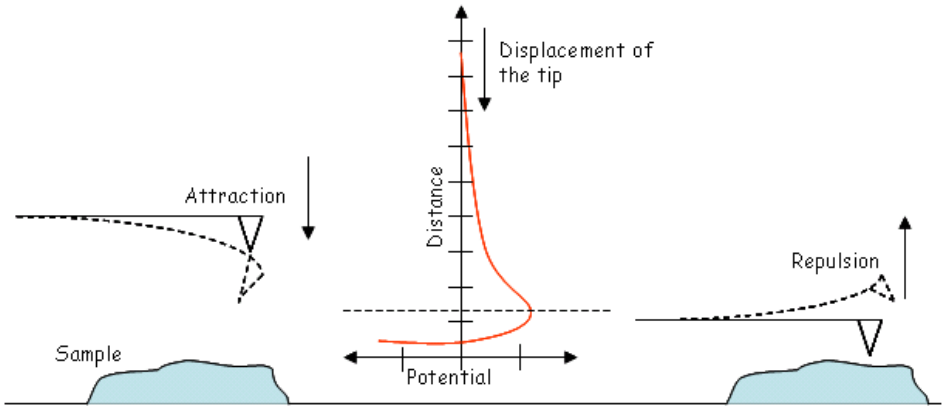

Figure 3.30 Tip-sample forces in AFM.

Constant height mode (attractive force). In this mode the distance between the sample and the tip is kept constant (Figure 3.31). The tip experiences an attractive force and the topography of the sample is obtained from the deflection of the cantilever. It is difficult to get a good reconstruction of corrugated samples using this mode.

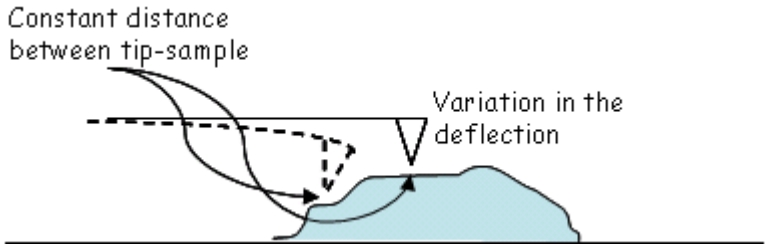

Figure 3.31 AFM; constant height mode.

Constant force (constant deflection mode, repulsive forces). In constant force mode the interaction of the tip is repulsive in nature [95]. When the tip is near to the sample it experiences a repulsive force (see Figure 3.30), the force is maintain constant moving the scanner up-down according with the topography of the sample. In this mode the accurate reconstruction of the sample is in function of the scanner feedback circuit see Figure 3.32.

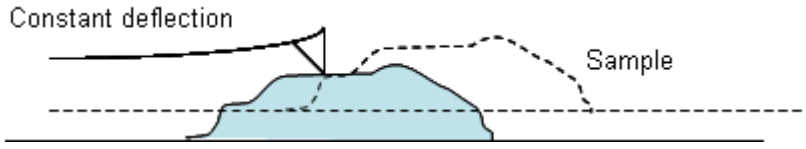

Figure 3.32 AFM constant deflection mode.

Noncontact mode. The cantilever oscillates near to its resonant frequency (almost constant). The interaction of the tip and the sample (Figure 3.33) induces variations in the amplitude; these changes in amplitude are sensed. The

feedback signals can be used to keep a constant distance, approximately of the order of 1- 10 nm, by the loop control to get a profile of the sample. Indeed the tip touches the sample just at certain points, which avoids damage to the sample (in particular biological samples) and topography reproduction is possible.

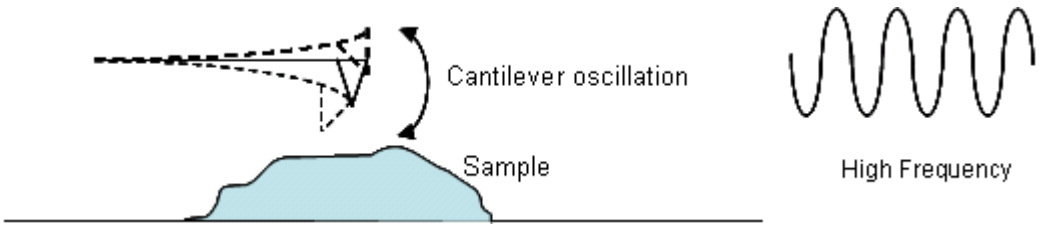

Figure 3.33 AFM; non-contact mode.

Tapping mode. In tapping mode the tip is oscillated and only touches the sample intermittently so damage to the sample is minimized. In this case the cantilever is oscillated at a high frequency (see Figure 3.34). It is similar to noncontact mode, the only difference is the frequency of oscillation, that in this case is higher than in noncontact mode.

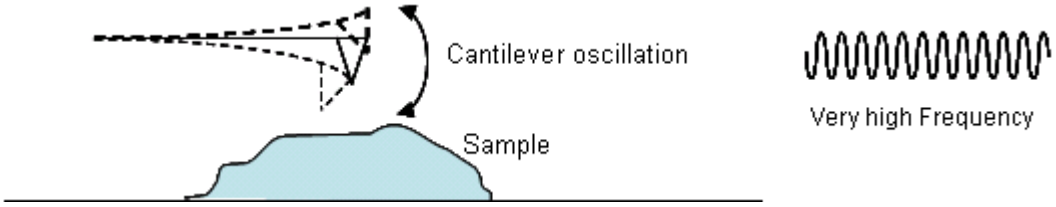

Figure 3.34 AFM; tapping mode.

Friction mode. In friction mode the tip detects changes in the friction of surfaces. This mode is normally used to study surface roughness (see Figure 3.35).

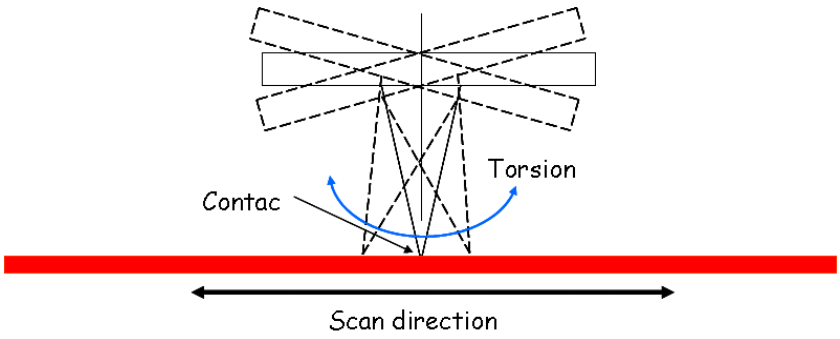

Figure 3.35 The tip is in direct contact with the sample (used to study the roughness).

3.6.4.6 Control system.

Another important part of the AFM is the electronic control system which has as its main function to coordinate the operation between the photodiode, piezoscanner and laser source (see Figure 3.36). The AFM can operate in two ways: by switching on the feedback loop and by switching it off. If the system is operated with the system switched on the mode is called constant force mode.

Operating the AFM in this mode allows the scanning of samples by the flexion constant (see modes 3.6.4.5). The interaction of the sample and the tip can cause the cantilever to be deflected as the profile of the sample changes. The loop control senses the intensity of the light and then sends the signals responding to the variations of the profile and readjusts the height of the sample by adjusting the voltage applied to the scanner.

In the case of feedback electronics being switched off, then the microscope will be operating in the so called constant height mode (see modes 3.6.4.5). This is particularly useful for imaging very flat samples at high resolution.

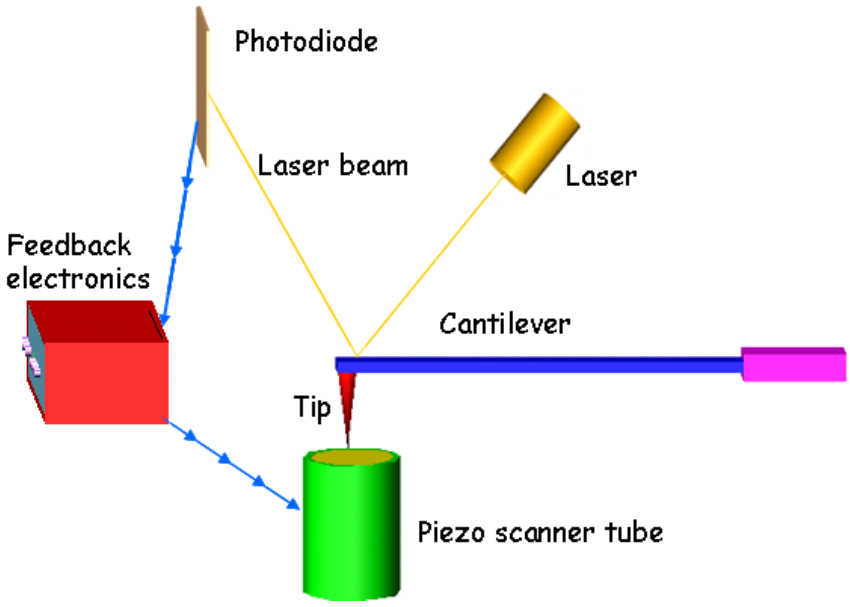

Figure 3.36 The loop allows a constant force to be attained between the tip and the sample; the deflection is detected by the electronic system; in order to keep a constant force the sample is displaced by the piezoscanner.

AFM has been used to study mechanical properties of single cells, due to it being a very versatile instrument. In addition, it can be used to perform air and fluid experiments. AFM is able to measure very small displacements and forces of the order of nm and pN respectively. The problem of calibration of the cantilever can

be overcome using one of several calibration techniques [159], although commercial available models offer a built in a calibration method that makes it simple. Moreover, it is possible to either get commercially coated cantilevers or to coat them according to the user requirements, therefore AFM is increasingly being selected as the instrument to use in a wide range of fields.

3.7 Other methods.

3.7.1 Microplate mechanical stretch method [160].

This method has been used to study changes in stiffness due to Sphingosylphosphorylcholine (SPC). The method consists of locating an in vitro Panc-1 cell between two glass microplates (Figure 3.37), and then stretching it, displacing the plates. This experiment shows how the rigidity of the cell is reduced when SPC is added to the medium.

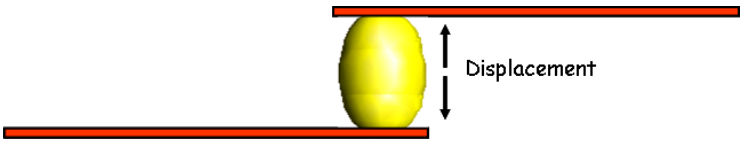

Figure 3.37 Micro plates stretching a cell.

In 1932 Cole used a very small gold beam to compress arbacia egg [161]. Images of the compressed and deflected cantilever enabled the contact area to be determined, and the egg compression and force on the area. In cell poking a glass probe is mounted at one end of a glass beam and the opposite end is mounted on a piezoelectric motor. This device is used to perform measurements of cellular viscosity cell poking [72]. Commercially it is possible to find specialised instruments to perform mechanical cell analysis for example CellHesion® is used to study cell-cell and cell-substrate interactions, JPK Instruments AG, Bouchéstrasse 12, Haus 2, Aufgang C, 12435 Berlin, Germany.

Chapter 4

Drag forces.

4.1 Introduction.

Atomic force microscope is finding increasing use in biological applications as a tool for investigating the mechanical properties and forces between molecules in addition to providing three dimensional surface profiles to high resolution. One of the major advantages with AFM is its ability to undertake measurements of specimens in fluid environments. This is particularly valuable as it opens up the possibility of undertaking investigations of biological samples in their natural, physiological environment [162-164].

4.1.1 Forces in normal fluid AFM contact mode operation (see 3.6.4.5).

The use of an aqueous medium has three advantages in AFM; first it is possible to recreate as close as possible the natural environment in order to perform in vitro experiments. Second, the adhesion force is reduced by a factor of 10-100, and the third, the van der Waals forces are reduced significantly too, however its use generates forces such as drag force, that together with other contributions [165] make up the total force (F_{Tot}) measured in the AFM. The (F_{Tot}) is formed by: sample contribution force (F_S), Drag force (F_d), van der Waals force (F_{VdW}), electrostatic force (F_{el}), magnetic force (F_{mag}) and chemical force (F_{Chem}).

$$F_{Tot} = F_S + F_{el} + F_d + F_{VdW} + F_{mag} + F_{Chem} \quad (4.1)$$

The sample force (F_S). It depends on the mechanical characteristics of the sample. The material tested could exhibit linear elastic behaviour, in this case there is a linear relationship between the applied stress σ and the strain ε, which can be represented by the relation: $\sigma = E\varepsilon$, that is, Hooke's law, in which E is Young's modulus. Another common class of material behaviour are the viscous materials, these materials are stretched when a load is applied. However, it is not its elongation εl that is proportional to the force, but its time rate of change $d(\varepsilon l)/dt$, this relationship can be written in terms of stress and strain: $\sigma = F\ d\varepsilon/dt = F\dot{\varepsilon}$ [166].

The electrostatic force (F_{el}). It is due to the interaction between a charged surface and the cantilever, this force depends on the charges involved and it can be attractive or repulsive [95]. These surface charges cause an electric field which decreases roughly exponentially with the increasing distance from the surface [167]. The electrostatic forces on a sphere with radius R was approximated for surface potentials below 50 nV [167]:

$$F_{el} = \frac{2\pi\lambda_D R}{\varepsilon_0\varepsilon_w} \cdot \left[\left(\sigma_T^2 + \sigma_S^2\right) \cdot \varepsilon_w^{-2d/\lambda_D} + 2\sigma_T\sigma_S \cdot e^{-D/\lambda_d}\right] \quad (4.2)$$

Where σ_T and σ_S are the surface charge densities of tip and sample surfaces, ε_0 and ε_w represent the vacuum permittivity and the dielectric constant of water, D is the surface-tip separation, λ_D is the Debye length.

The van der Waals force (F_{VdW}). It is due to the interaction of the atoms of the sample and the end of the cantilever tip and is defined by [165]:

$$F_{vdW} = -\frac{HR_T}{6D^2} \quad (4.3)$$

Where H is the Hamaker constant, R_T the radius tip and D surface-tip separation.

Chemical force (F_{Chem}). It is due to the formation of chemical bonds between tip and sample atoms, examples of chemical interaction can be found in [168, 169].

Magnetic force (F_{mag}). In most of the cases this term is neglected due to the fact that tips are not sensitive to this force [165].

The drag force (F_d). It is generated due to the interaction of the cantilever and the fluid (friction between cantilever and fluid and change in the flow pattern in the case of non- laminar flow). The F_d is dependent on the fluid viscosity, the relative velocity between cantilever and fluid, cantilever shape and the cantilever/tip-surface separation. In Figure 4.1 it can be seen that the flow lines direction changes near the cantilever, the mathematical models used to determine this will be discussed in the next section.

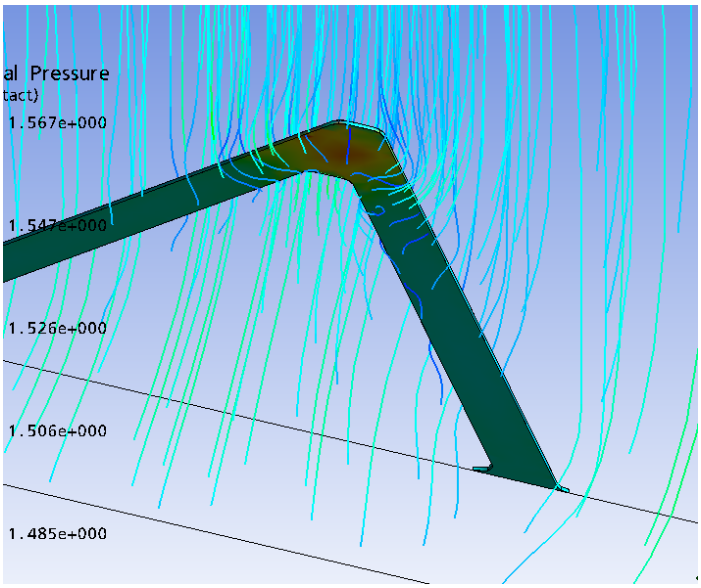

Figure 4.1 Stream lines deviation around the cantilever.

The drag forces are generated when the cantilever moves either towards or away from the sample surface, for example in indentation (approach) and in the retraction experiments (see section 6.6). In Figures 4.2 and 4.3 two examples of AFM are shown, in the first a cell is indented, the drag forces are opposite to the movement of the cantilever, in the second figure a retraction experiment of a DNA sample is shown.

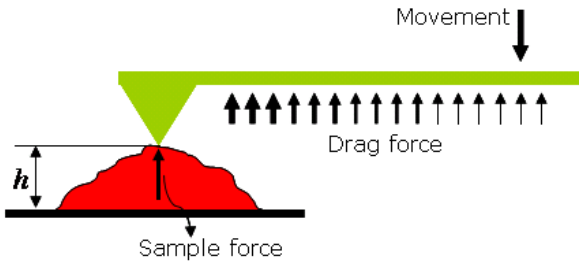

Figure 4.2 Indentation of a cell.

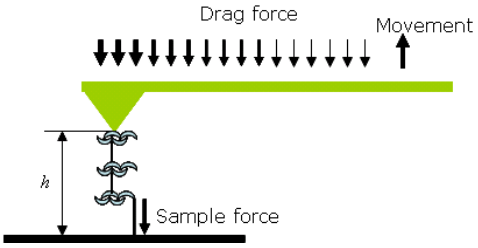

Figure 4.3 Pulling of a single molecule.

4.1.2 Mathematical drag force models.

The use of AFM for soft samples in fluid environments results in the introduction of a hydrodynamic drag force due to viscous friction of the cantilever with the surrounding fluid through which it moves [162-164, 170-172]. Cantilever-tip velocities or pulling speeds in AFM are generally such that the flow can be considered to be purely laminar flow, with Reynolds number (Re) typically below 1 [164, 170, 171]. Under such circumstances the drag force is dependent upon factors including the dimensions and velocity of the cantilever, the fluid viscosity, and the cantilever/tip-surface separation [164, 170, 171]. In cases where the magnitudes of the measured forces are low then the drag force can be of a similar order to the reaction force of the sample [171]. Under such circumstances if allowance is not made for the hydrodynamic drag force then significant errors in measurement can occur.

While hydrodynamic forces have been calculated for geometries such as spheres moving through viscous fluids [173, 174] as they approach a surface at low Reynolds number, it is not possible to directly assess the drag forces on the cantilever-tip arrangement of the AFM during the probing of soft samples in liquid environments as there is no means of accurately determining the force generated by the sample [164].

Researchers have utilised a variety of means in an attempt to account for the drag force in AFM measurements. O'Shea and Welland [175] employed the 'string of spheres' model [176] to obtain an expression for the drag on a rectangular beam approaching a surface at normal inclination. Ma et al. [170] investigated the zero frequency hydrodynamic drag coefficient of a tipless AFM cantilever in a fluid at different separations of the cantilever with respect to a glass surface. The researchers found that the experimental data obtained, which demonstrates the increase in drag coefficient as the probe approaches the

surface, could be well represented by Brenner's model [173] for a sphere moving normally towards a rigid surface. This suggests that there is an inverse scaling relationship between hydrodynamic drag force and cantilever-surface separation which is in contrast to the model of O' Shea and Welland [175] which considers a scaling that is inverse cubic in form.

An investigation into the effects of hydrodynamic drag in AFM measurements of soft samples in liquids at low Reynolds numbers has been undertaken by Alcaraz et al. [164]. This research confirmed that the hydrodynamic drag force exhibits a locally pure viscous behaviour and that the drag factor is dependent upon distance between the tip and the substrate. The authors pointed out that previous attempts to correct AFM measurements for hydrodynamic drag effects have consisted of estimating the drag force at some distance above the specimen then using this value to correct the measurements taken on contact [177-179]. However, it is expected that this approach will lead to an underestimation of the actual hydrodynamic drag at contact and the authors note that applying corrective drag force measurements taken at even a few microns above the sample can lead to significant errors in AFM measurements. From their findings Alcaraz et al. suggest a scaled spherical model for the cantilever to more accurately account for the drag factor dependence on distance. In the model envisaged the cantilever and tip arrangement is represented by a 1-D oscillator with an effective mass and spring constant and force on the cantilever is considered to consist of two components: the force applied by the sample and the viscous drag force. The analysis leads to a scaled spherical model of the cantilever which enables the drag factor at contact to be estimated by extrapolating drag factor data obtained in non-contact measurements obtained at various distances from the substrate. The model contains two empirical coefficients, one which represents the effective sphere radius of the cantilever and the other which represents the effective tip height.

4.1.2.1 Alcaraz et al. [164] model.

The expression for the drag on a spherical object moving slowly through a viscous fluid (Re<1) was first derived by Stokes [180]; this expression is of the form.

$$F_d = 6\pi\mu R v \tag{4.4}$$

where F_d is the drag force, μ is the fluid's dynamic viscosity, R is the radius of the spherical object and v is the velocity of the sphere relative to the fluid.

Stokes's law does however, have a number of limitations. For example, it considers the fluid to be of infinite extent and as such does not take account the presence of boundaries at a finite distance from the object. Under such circumstances corrections to Stokes's drag forces expression are necessary. In a further advancement Brenner [173] and Cox and Brenner [174] derived expressions for the drag force present during the motion of a spherical particle towards or away from a single plane surface in an otherwise unlimited fluid. The analytical expression for the hydrodynamic force derived is of the following form for low Reynolds number:

$$F_d = b(h)\,v \tag{4.5}$$

Where v is the relative velocity between the sphere and the plane wall, $b(h)$ is the drag damping factor which is defined as:

$$b(h) = \frac{6\,\pi\,\eta\,R^2}{h} \tag{4.6}$$

Where η is the fluid's viscosity, R is the sphere radius and h is the distance of the gap between the sphere and the plane wall.

Alcaraz et al. [164] argued that since the main contribution to the drag force arises from the viscous friction between the cantilever and the surface then it is possible to extend the spherical model of Brenner [173]and Cox and Brenner [174] to geometries such as that of an AFM cantilever by scaling the dimension of the body and the distance to the substrate. In the spherical scaled model suggested by Alcaraz et al. [164] the hydrodynamic behaviour of the AFM cantilever is modelled as a drag factor, dependent on distance from the substrate; the expression proposed by Alcaraz and co-workers is:

$$b(h) = \frac{6\pi\eta\,a_{eff}^2}{h + h_{eff}} \tag{4.7}$$

Where $h + h_{eff}$ is the effective cantilever tip height and a_{eff} is the effective radius of the cantilever, η is the viscosity of the liquid, h, the platform-tip separation.

Equation (4.7) predicts the increase of drag force on the cantilever as it moves close to the plane wall.

Alcaraz et al. [164] modeled the cantilever-fluid interaction as a spring-mass model, as illustrated in Figure 4.4. The cantilever-tip is represent by a 1-D oscillator with a effective mass (m_{eff}) and spring constant (k). Under these conditions the measured force (F) has two main components: the force sample measured (F_s) and the drag force (F_d).

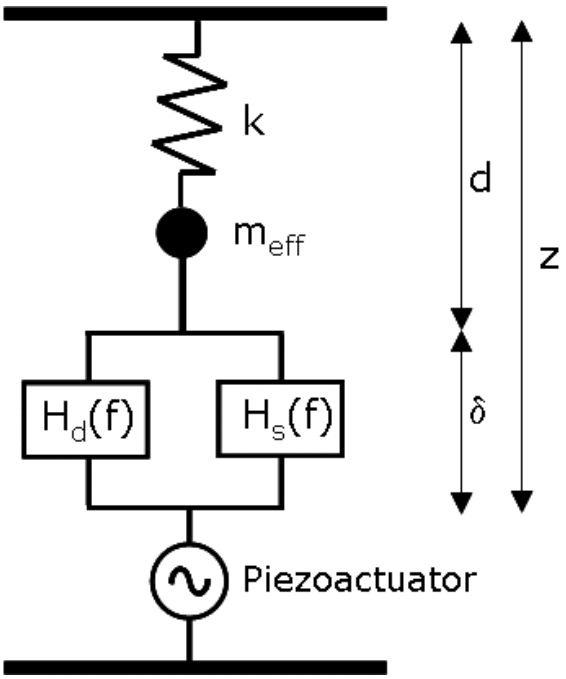

Figure 4.4 Mechanical model proposed for Alcaraz, taken from [171].

The force can be computed with the expression $F = kd$ where d, is the cantilever defection and k, is the spring constant. This system can be represented by the Equation (4.8), where the left hand side of the expression represents the cantilever, with an oscillating effective mass generated by the sample force interaction, the right side of the expression represents the hydrostatic drag force and sample contribution forces.

$$m_{meff}\frac{d^2d}{dt^2} + kd = F_s + F_d \tag{4.8}$$

If Equation (4.8) is transformed to the frequency domain and divided by $\delta(f)$ then sample and the fluid viscoelastic behaviour are characterized in the frequency domain by their mechanical transfer functions $H_s(f)$ and $H_d(f)$. The microrehological behaviour of the sample can be characterised in the frequency

domain by a mechanical transfer function defined as $H_s(f) = F_s(f)/\delta(f)$. In a similar manner the viscoelastic behaviour of the fluid can be represented by the hydrodynamic drag transfer frequency domain and divided by $\delta(f)$:

$$\left(-4\pi^2 m_{eff} f^2 + k\right)\frac{d(f)}{\delta(f)} = H_s(f) + H_d(f) \tag{4.9}$$

The resonant frequency is $f_0^2 = k/(4\pi^2 m_{eff})$, the force due to cantilever deflection $F = k \cdot d$ and the global measured mechanical transfer function is $H(f) = F(f)/\delta(f)$. Solving the equation for $H_s(f)$

$$\left(-k\frac{f^2}{f_0^2} + k\right)\frac{d(f)}{\delta(f)} = H_s(f) + H_d(f) \tag{4.10}$$

$$\left(-F\frac{f^2}{f_0^2} + F\right)\frac{(f)}{\delta(f)} = H_s(f) + H_d(f) \tag{4.11}$$

$$H_s(f) = \left[1 - \left(\frac{f}{f_0}\right)^2\right]H(f) - H_d(f) \tag{4.12}$$

For low frequencies ($f << f_0$) expression (4.12) can be simplified

$$H_s(f) = H(f) - H_d(f)) \tag{4.13}$$

For low Reynolds number conditions ($\mathrm{Re} < 1$) the hydrodynamic force is expressed in (4.5) as $F_d = b(h)v$ and its corresponding drag transfer function is:

$$H_d(f) = 2\pi\, if\, b(h) \tag{4.14}$$

Where $i = \sqrt{-1}$. $b(h)$ can be calculated for different h by measuring $H_d(f)$ at each desired distance, in noncontact measurements $H_s(f) = 0$ (non sample-cantilever interaction) and $H_d(f) = H(f)$, $H_d(f)$ can be calculated using the relationship $H_d(f) = \dfrac{kH_a(f)}{k - H_a(f)}$ where $H_a(f) = S_{FF}/S_{ZF}$, where S_{FF} and S_{ZF} are the auto and cross-spectrum, using the phase shift of the piezoactuator ϕ_{PZT} it is possible to separate $H_d(f)$ into real and imaginary terms Equation (4.14).

$$H_d(f) = H_d'(f) + iH_d''(f) \tag{4.15}$$

Using the imaginary term $iH_d''(f)$ can be used to compute the drag factor at each platform-tip separation $b(h)$ by a linear fitting of $iH_d''(f)$ vs. f, therefore $b(0)$ can be estimated by extrapolating to $h=0$, the coefficient a_{eff} and h_{eff} can be determined by fitting in Equation (4.7).

Using the scaled spherical model of Alcaraz et al. [164] Janovjak et al. [171] investigated hydrodynamic drag forces in single-molecule force measurements in AFM for different pulling speeds. The authors pointed out that hydrodynamic effects become particular significant at pulling speeds greater than 10 μm/s when they reach a similar order of magnitude to the molecular forces. In the course of their research Janovjak et al. investigated the scaled spherical model proposed by Alcaraz et al. [164]. Using the model they quantified the hydrodynamic drag force as a function of pulling speed and tip-sample separation for two V-shaped AFM cantilevers and found that while drag force exhibited a linear dependence on pulling speed (see Figure 4.5), the relationship with tip-surface separation was more complex in nature (see Figure 4.6). Note that in Figures 4.5 and 4.6 the squares represent the experiments undertaken in PBS fluid and the circles the measurements in water. In addition, the authors investigating hydrodynamic effects during the unfolding of an individual molecule of a multi domain protein. They found that if hydrodynamic effects are considered then AFM force measurements can be more accurately evaluated at pulling speeds greater than a few μm/s.

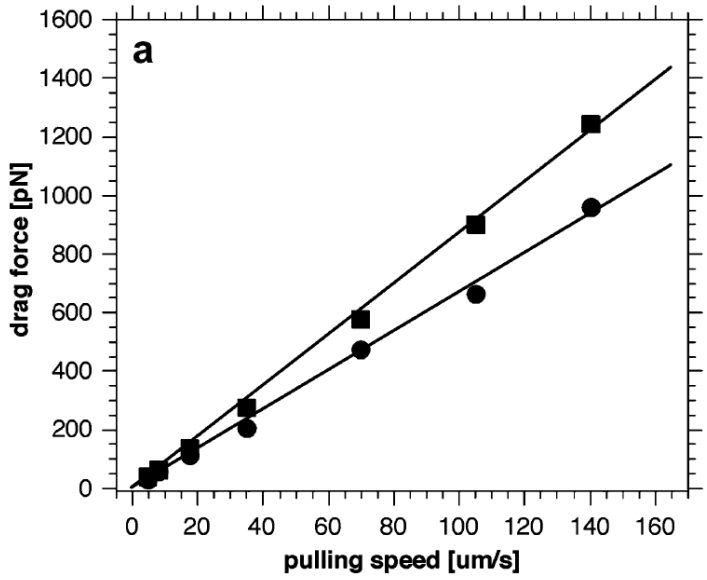

Figure 4.5 Drag force vs velocity dependency, taken from [171].

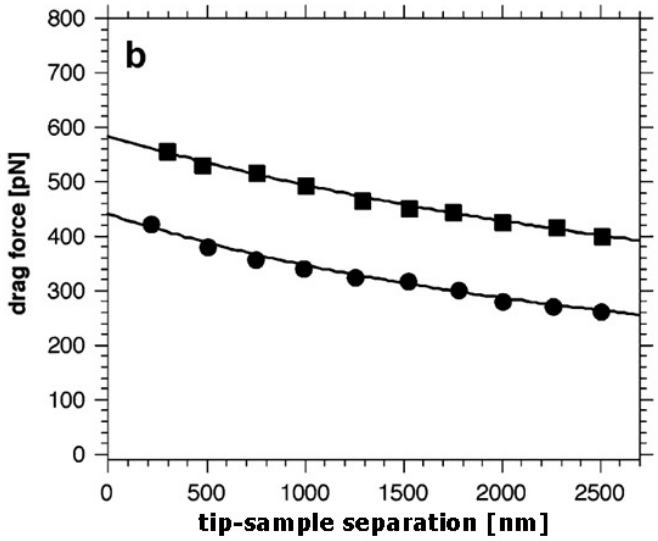

Figure 4.6 Force vs. platform-tip separation dependency, taken from [171].

Another study in which drag forces were considered has been undertaken by Vinogradona et al. [181, 182] who studied the dynamic effects in AFM measurements. In this work the cantilever is idealised using the parallel beam approximation [183], a sphere is attached to the end of the cantilever, and the forces acting on the cantilever and tip are: a concentrated force acting on the sphere tip, a pressure due to a distributed force acting on the cantilever and finally a hydrodynamic force acting on the cantilever, Figure 4.7 shows a schematic representation of the system.

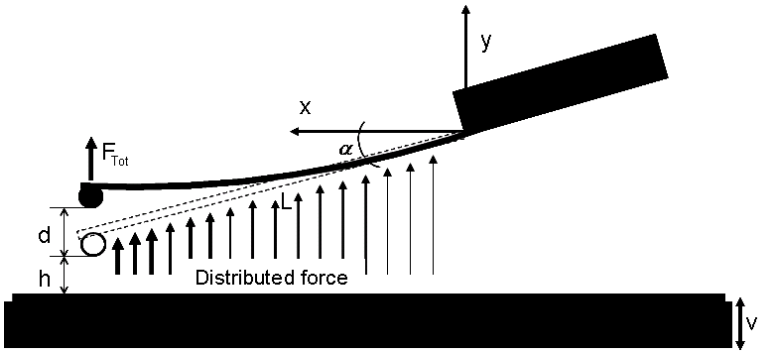

Figure 4.7 Forces acting on the AFM cantilever, adapted from [181].

The concentrated force acting on the spherical cantilever-tip, (F) is due to solid-solid interaction (spherical tip-substrate) and a solid-fluid interaction (Fluid-spherical cantilever tip). The solid-solid interaction generates surface forces as was seen in section 4.1.1; the forces (F_{sur}) can be due to van der waals, electrostatic and chemical forces, etc. Finally the hydrodynamic force (F_d) acting on the spherical cantilever tip is expressed by Vinogradona et al. [181] based on Barnocky and Davis [184] as:

$$F_d = -6\mu\pi R \frac{dh}{dt}\left(1 + \frac{R}{h} f^*\right) \tag{4.16}$$

Where, μ is the viscosity, velocity of sphere $v = dh/dt$, R is the radius of the sphere, h is the platform-tip distance and f^* is a correction factor for deviations from the Reynolds flow in thin gaps.

Therefore the concentrated force is:

$$F = F_d + F_{sur} \tag{4.17}$$

The total cantilever deflection d_T, is considered to be due to the three factors previously mentioned, the concentrated force (I), the pressure force due to the small cantilever-substrate distance (II) and finally the deflection due to the cantilever displacement (III).

I. The deflection (d_1) of the cantilever due to the concentrated force is defined by the expression:

$$d_1 = \frac{F}{2k}(-1 + 3\ \cos\ \alpha) \tag{4.18}$$

Where k is the is the spring constant $k = 3EI/L^3$, F is the concentrated force and α is the tilt angle, E is the cantilever Young's modulus, I, is the moment of inertia, L, length of the cantilever .

II. Due to the small distance between the cantilever and the substrate the normal fluid flow is altered resulting in a force acting normal to the cantilever tip area. The deflection of the cantilever due to this pressure was obtained using a lubrication approximation Navier-Stokes theory for two spheres, which after mathematical operation gives:

$$d_2 = -\frac{3v\eta}{8k}\left(\frac{w}{h}\right)^3 \gamma^* \tag{4.19}$$

Where v, is the velocity, w, is the cantilever width, η is the fluid viscosity, h, is the platform-tip separation and γ^* correction from the tilt angle between the cantilever and surfaces.

III. The cantilever is considered as a body moving into the fluid, where the frictional forces bend the cantilever; this phenomenon is described by Stokes law, and is represented by the expression:

$$d_3 \sim -\frac{3 v \eta L A}{8k} \tag{4.20}$$

Where A, is a fitting parameter which depends on cantilever geometry.

The total cantilever deflection due to I, II and III is: $d = d_1 + d_2 + d_3$, therefore it can be written:

$$d = \frac{F}{2k}(-1 + 3\cos 3) - \frac{3v\eta}{8k}\left[\left(\frac{w}{h}\right)^3 \gamma^* + A\right] \tag{4.21}$$

In the both previously methods the drag force has been analysing, in the case of the model developed by Alcaraz et al. [164] it is necessary to determine geometric factors (a_{eff} and h_{eff}) in order to calculated the drag force, and in the analysis made by Vinogradona et al. [181, 182] the drag force is calculated adding the effect of drag force acting on the spherical cantilever tip moving in fluid and the force acting on the moving cantilever, in this analysis it is also necessary to use a geometrical factor A, it is necessary to mention that the Vinogradona et al. [181, 182] formulation are made just for spherical cantilever tip which limits its use. In the next chapter it is propose the use of finite element method as a alternative tool to study drag forces, comparing the simulation with experimental results, with the objective of find out if it is possible to explore micro fluid problems with this tool.

Chapter 5

Coupled drag force model.

5.1 Introduction.

This Chapter describes a coupled model that enables the influence of the hydrodynamic drag force on experimental data obtained from AFM measurements of soft samples in fluid environments to be investigated. Validation of the model was performed using data obtained from experimental work undertaken on an AFM. The coupled model is shown to accurately account for drag forces in AFM in fluid media. This model was created using the Ansys Workbench 11.0 commercial software package. The laminar flow formulation available through the Ansys CFX module of Workbench was employed for the fluid media. This was coupled to cantilever and tip solid model. In order to investigate hydrodynamic drag force effects, experimental data were obtained using an AFM with a V-shaped cantilever fitted with a pyramidal tip. Tip velocities ranging from 1.05 to 105 μm/s were employed in water, polyethylene glycol and glycerol with the platform approached from a distance of 6000 nm. The AFM was employed in contact mode. The coupled model is also compared with an existing analytical model that attempts to quantify hydrodynamic drag force effects in AFM in fluid media [171].

5.2 Computational Model.

The aim of the coupled novel model is to quantify the hydrodynamic drag force during the motion of the cantilever of the AFM through the fluid towards the substrate so that predictions can be compared with experimental data. In order to ensure accuracy in the numerical model and facilitate a comparison with experimental results it is necessary to reproduce the experimental conditions in the numerical model. This means that cantilever, fluid and environmental conditions of the model must be as similar as possible to those of the experiments. The parameters that define the cantilever are: the geometry, mechanical properties and fluid-surface interaction; for the fluid the parameters are: shape, density and viscosity. Other characteristics that must be taken account are the displacement and velocity of the scanner, and environmental temperature.

Figure 5.1 shows the main components considered in the development of the model, these include the cantilever, fluid medium, the glass slide, cantilever chip holder and chip. The problem requires analysis of the solid cantilever, the fluid medium and the interaction between the cantilever and the fluid medium and can be classified as a Fluid Solid Interface (FSI) problem. To model and solve this type of problem requires a program with the capability to deal with such particular interactions.

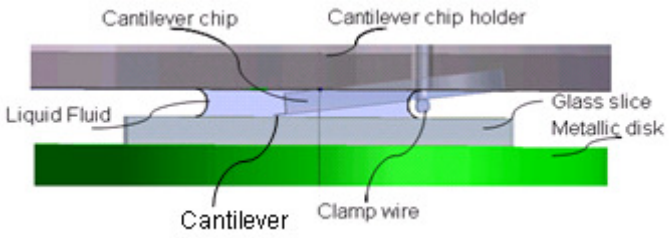

Figure 5.1 Components considered in the numerical model.

The model developed utilises the commercially available ANSYS Workbench software. The fluid was modelled using the ANSYS CFX finite element module. This was coupled with the solid model of the cantilever which was modelled using the ANSYS structural mechanics module. The remaining components e.g. substrate, cantilever chip holder etc, were modelled by the use of appropriate boundary conditions applied in the coupled solid/fluid models.

The fluid flow model considers the fluid to be 3-D, single phase, viscous, incompressible and laminar in nature. A transient dynamic analysis (ANSYS

flexible dynamic analysis) is undertaken for the cantilever. The overall simulation time for each analysis was calculated from the velocity and cantilever distance travelled (6000 nm), giving simulation times between 5.71s (velocity = 1.05 μm/s) and 0.0571 s (velocity = 105 μm/s)

The modelling process followed is illustrated in Figure 5.2; this consists of the modelling of the solid (left part of diagram), the cantilever and tip, which is practically the same process followed for a standard dynamic analysis with one difference, the creation of the interface boundary condition (the portion of the solid surface in contact with the fluid model). The final stage of the solid model creation process is the production of the input file (file linked to fluid model). The fluid component model (right part of diagram) is created as a standard CFX (ANSYS module for fluids) model with an extra boundary condition, the interface contact (the portion of the fluid in contact with the solid model). A particular detail of the fluid model is the coupling with the solid model. The coupling of the two models results in the forces calculated from the fluid analysis being applied to the solid model. Equally, if there is any change in the geometry/deformation of the solid model then this information is provided to the fluid model. This process is repeated for each of the time-steps in the analysis.

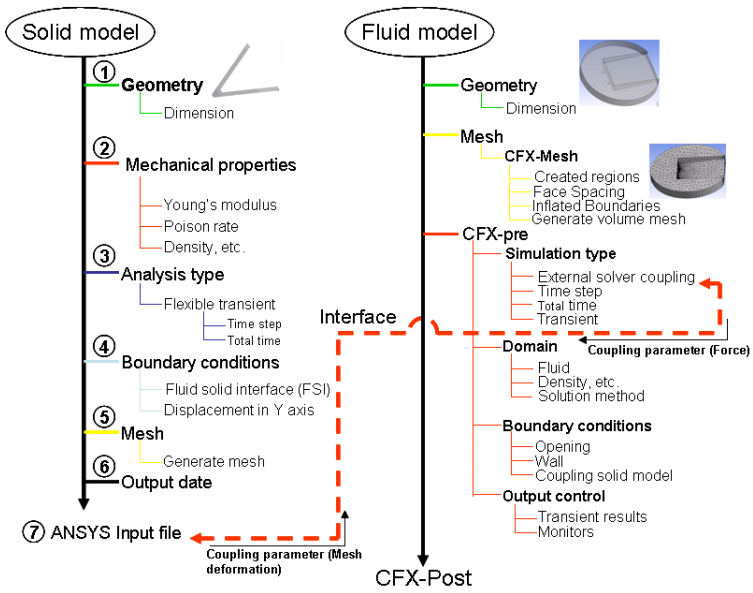

Figure 5.2 ANSYS Workbench solid-fluid model of the cantilever-fluid system.

The following sections describe the solid and fluid models and their coupling through the specification of appropriate boundary conditions in more detail.

5.3 Solid Model.

In order to develop and ensure accuracy in the solid model of the cantilever and tip it is necessary to obtain accurate values for cantilever and tip geometry, stiffness and Young's modulus; this is described in the three sections that follow.

5.3.1 Cantilever and tip properties.

5.3.1.1 Stiffness.

The cantilever used in the experimental tests is a silicon nitride V-shaped (Veeco DNP-20) cantilever. Measurement of the deflection of the cantilever resulting from the interaction with the sample enables the determination of the force via Hooke's law, $\mathrm{F} = \mathrm{k} \cdot \delta$, where F is force, k is the cantilever spring constant and δ is the deflection of the cantilever (determined by sensing the changes in light intensity as detected by the photosensor). An accurate value for the spring constant k is therefore vital to the success of the technique. Accurate determination of the cantilever spring constant k was undertaken using the Thermal Tune Method [159]. Using this method the spring constant for the cantilever was determined as being $k = 0.03544\ N/m$ (standard deviation $0.001104\ N/m$).

5.3.1.2 Geometry.

In the numerical model, cantilever dimensions can directly affect the quantification of drag forces, consequently the dimensions of the cantilever need to be defined to high accuracy. The dimensions of the main body of the cantilever were obtained from pictures taken using the camera attached to the AFM. These were used to confirm manufacturer specifications where available and to provide the additional dimensions not provided (see Figures 5.3, 5.4 and 5.5 and Tables 5.1 and 5.2). This approach was taken because small variations in geometry are possible even in the highly accurate manufacturing process used to produce cantilevers and tips. Table 5.3 shows the final dimensions that were used for the numerical model.

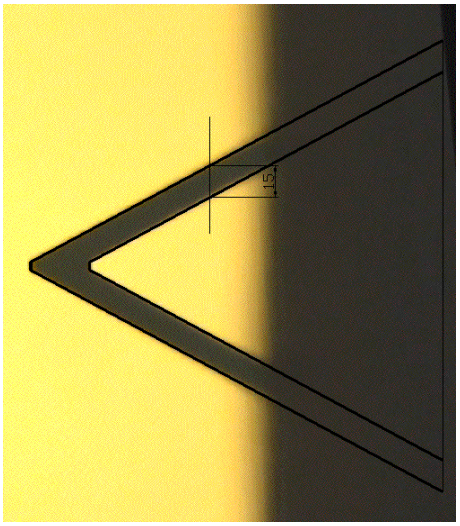

Figure 5.3 Image of cantilever.

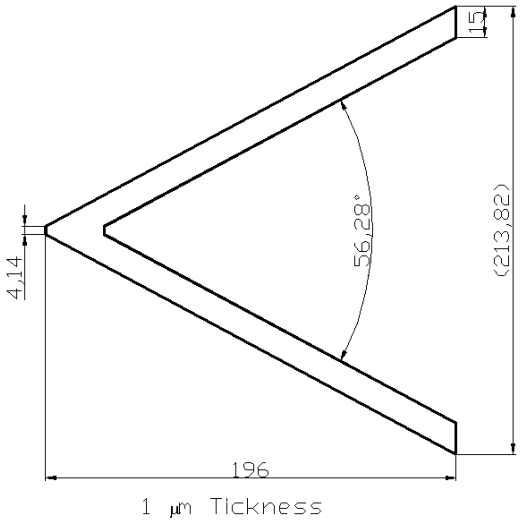

Figure 5.4 Dimension of the cantilever model.

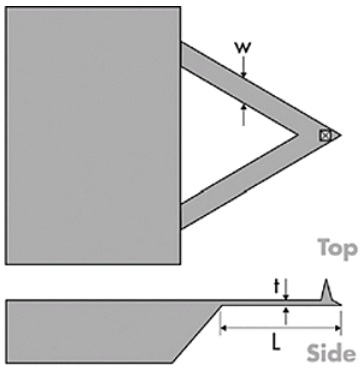

Figure 5.5 Veeco cantilever.

Width	15 µm
Thickness	0.6 µm
Length	196 µm

Table 5.1 Veeco cantilever general dimensions.

Cast Tip height	2.5 - 3.5 µm
Front angle (θ)	35 ± 2º

Table 5.2 Veeco tip specifications.

Geometry	Symbol	Dimension
Length	L	196 µm
Thickness	t	0.6 µm
Width	w	15 µm
Tip height		3 µm
Tip front angle	θ	35 º
Distance between arms	b	213.82 µm
Cantilever arm angle	α	56.28 º

Table 5.3 Dimensions used for the numerical model

5.3.1.3 Young's modulus.

In order to calculate an accurate value for Young's modulus that can be employed in the coupled model the spring constant k, determined by the thermal tune method (section 5.3.1.4, 5.3.1.5 and 6.4) is utilised; its value being 0.03544 N/m.

The Veeco DNP-20 cantilever used in the experiments is made up of several layers of materials with different mechanical properties. Table 5.4 gives information about the cantilever composition in terms of materials and material layer thicknesses.

Material	Silicon Nitride
Thickness	0.4 – 0.7 μm
Bottom layer back	15 nm Cr
Top layer back	60 nm Au

Table 5.4 Veeco cantilever composition.

As can be seen from Table 5.4 the cantilever is made predominantly from silicon nitride but with a top layer back coating of Au and a bottom layer back coating of Cr.

The overall effective Young's modulus, E, of the cantilever is the result of the combination of the three layers of materials. The accurate modelling of such a cantilever is only possible if the exact layer thicknesses are know, but as indicated by Table 5.4 it is difficult to accurately measure the exact dimensions of the layers. In the numerical model a simplification is made whereby the cantilever is considered to consist of a single, homogeneous material. Adopting this assumption means that a methodology for calculating an effective value for Young's modulus for use in the numerical model is therefore required. Note that even in cases where the manufacturer provides material properties for the cantilevers produced, significant differences may exist between the specified and actual material property values due to variances encountered during the manufacturing process, so a methodology for determining an effective value for the Young's modulus of the cantilever is of significant value.

In order to obtain accurate values for Young's modulus that can be utilised in the numerical model two possible approaches are considered here. The first involves using existing analytical models that are applicable for particular cantilever

shapes. The second consists of the creation of a finite element model. Both approaches are discussed below.

5.3.1.4 Analytical models to determine Young's modulus.

There are several analytical models which can be used to describe the mechanical behaviour of V-shape cantilevers, in particular the models proposed by Butt [185] Albrecht [186], Sader [187], and Sader and White [188]. Each model attempts to describe the behaviour of different cantilever geometries (see Figure 5.6). These analytical models are based on the Euler–Bernoulli equation for cantilever deflection analysis and the resulting equations can be rearranged for Young's modulus, E (see equations 5.1 to 5.4). As there is not a specific equation that is applicable for the geometry of the cantilever used in the experiment tests described in this thesis then all of the expressions will be considered and the results analysed. By substituting the cantilever dimensions previously determined (Table 5.3) and the value of the spring constant of $k = 0.03544\ N/m$ into Equations 5.1 to 5.4, values for Young's modulus can be obtained.

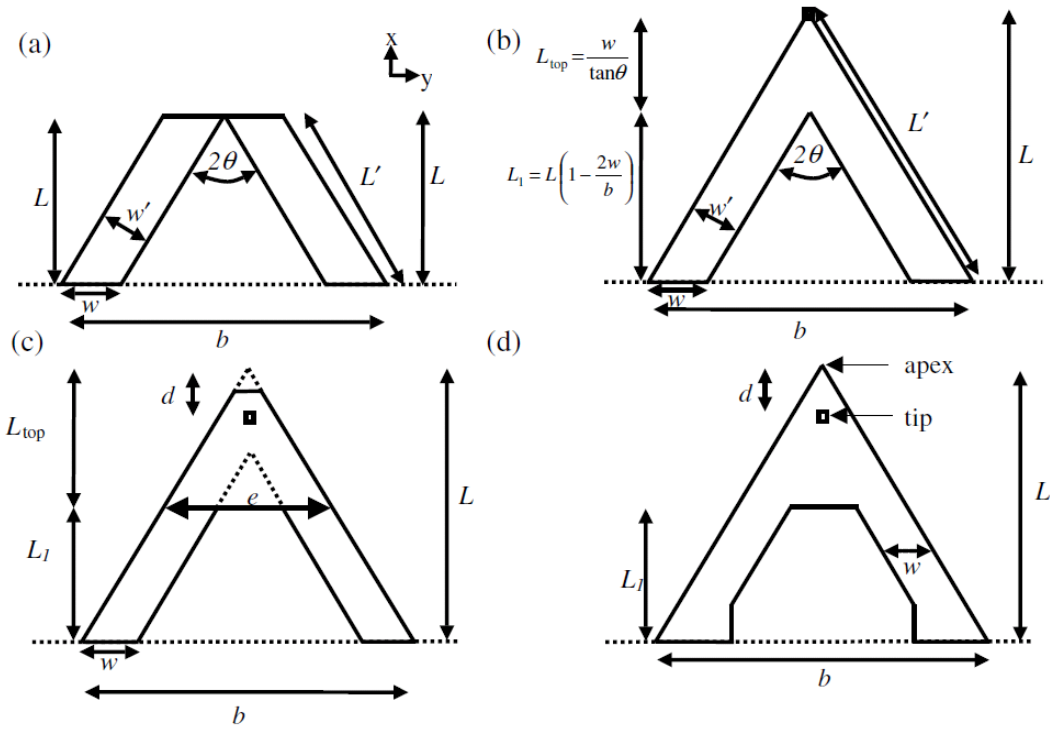

Figure 5.6 a) Parallel beam approximation, Butt [185] b) v-shaped cantilever, the indenter is considered to be in the apex, Albrecht [186], Sader and White [188] and Sader [187], c) realistic cantilever model, Tortonese [189], d) Veeco style cantilever. Taken from [183]

Parallel Beam Approximation (PBA) [190]

$$E = \frac{2kL^3}{wt^3} \tag{5.1}$$

Albrecht [186]

$$E = k\frac{2L^3}{wt^3}(1+\frac{b^2}{4L^2})^2 \tag{5.2}$$

Sader [187]

$$E = k\frac{2L^3}{wt^3}(1+\frac{4w^3}{b^3}(3\cos\theta - 2))\cos^{-1}\theta \tag{5.3}$$

Sader and White [188]

$$E = k\frac{2L^3}{wt^3}(1+\frac{4w^3}{b^3}) \tag{5.4}$$

where L is cantilever length, w is width and t is the thickness, k is spring constant, b is the distance between arms, θ is the half angle.

Substituting the values of k, and L, w, t, b and θ from Table 5.3 in Equations 5.1-5.4 yields:

Parallel Beam Approximation Equation (5.1)

$$\mathrm{E} = \frac{2(0.03544\mathrm{N/m})(196\mathrm{x}10^{-6}\mathrm{m})^3}{15\mathrm{x}10^{-6}\mathrm{m}(0.6\mathrm{x}10^{-6}\mathrm{m})^3} = 165\ GPa$$

Albrecht Equation (5.2)

$$\mathrm{E} = \frac{2(0.03544\,\mathrm{N/m})(196\mathrm{x}10^{-6}\mathrm{m})^3}{(15\mathrm{x}10^{-6}\mathrm{m})(0.6\mathrm{x}10^{-6}\mathrm{m})^3}(1+\frac{(213.82\mathrm{x}10^{-6})^2}{4(196\mathrm{x}10^{-6}\mathrm{m})^2})^2 = 277\ GPa$$

Sader Equation (5.3)

$$E = \frac{2(0.03544\ N/m)(196x10^{-6}m)^3}{(15x10^{-6}m)(0.6x10^{-6}m)}(1+\frac{4(15x10^{-6}m)^3}{(213.82x10^{-6}m)^3}(3\cos 17.5-2))^1\cos^{-1}17.5$$

$$=173\ GPa$$

Sader and White Equation (5.4)

$$E = \frac{2(0.03544\ N/m)(196x10^{-6}m)^3}{(15x10^{-6}m)(0.6x10^{-6}m)}\left[1+\frac{4(15x10^{-6}m)^3}{(213.82x10^{-6}m)^3}\right]=165GPa$$

Comparing the results obtained from using the above equations it can be seen that the difference in E value calculated using the above equations is around 40%, a significant difference. Given this fact it was decided that an alternative approach would be taken to investigate which of the models better describes the cantilever used in the experiments detailed in this thesis thus enabling a more accurate determination of an effective Young's modulus for the cantilever. In the next section the second approach, finite element modelling (FEM), is used to calculate an effective value for the Young's modulus, E, of the cantilever.

5.3.1.5 Finite element approach to determine Young's modulus.

A model of the V-shaped cantilever was created in ANSYS using the dimensions detailed in Table 5.3, and geometry shown in Figure 5.4. The cantilever and tip model shown in Figure 5.7 was utilised. The right hand ends of the cantilever were fixed and a force was applied to the tip; these boundary conditions are illustrated in Figures 5.7 and 5.8. The cantilever and tip geometry was meshed with 5522 10-noded quadratic tetrahedral structural solid elements. Young's modulus (E) was varied in the range 200-20,000 MPa. A number of discrete values of E (50) within this range were considered. The mechanical properties used in the model are given in Table 5.5. A deflection was chosen that was within the elastic range of the material and of a similar order as expected in the experimental tests (1.2 μm). For each of the values of Young's modulus considered the cantilever model was run with the applied force being adjusted until the required deflection (1.2 μm) was obtained. From the resulting deflections (δ) and applied force (F) the cantilever stiffness k was calculated

using the Hooke's Law relationship, $F = k \cdot \delta$. Tables 5.6 and 5.7 show sample results from the model.

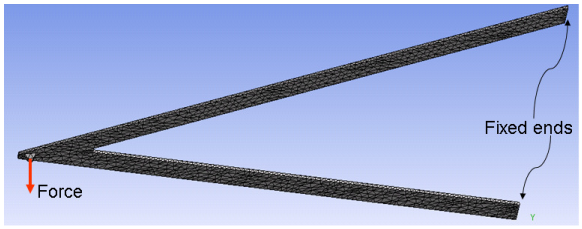

Figure 5.7 Cantilever Model.

Figure 5.8 Boundary conditions.

Structural steel properties	
Young's modulus	Variable 200-200 000 MPa
Density	3 290 kg/m^3
Poisson ratio	0.27

Table 5.5 Material properties of the modelled V-Shaped cantilever (silicon nitride), taken from http://www.accuratus.com/.

Applied deflection (mm)	Force (Fy) (μN)	k N/m	E (MPa)
1.2	0.000046455	0.000038716	200

Table 5.6 Model analysis result E = 200 MPa

Applied deflection (μm)	Force (Fy) (μN)	k N/m	E (MPa)
1.2	0.046455	0.038716	200 000

Table 5.7 Model analysis result E = 200 000 MPa

From these results a graph relating Young's modulus E and cantilever stiffness k was constructed (Figure 5.9). As the model is based on the Euler-Bernoulli theory [191] the relationship between k and E, as shown in Figure 5.9, is, as expected, linear.

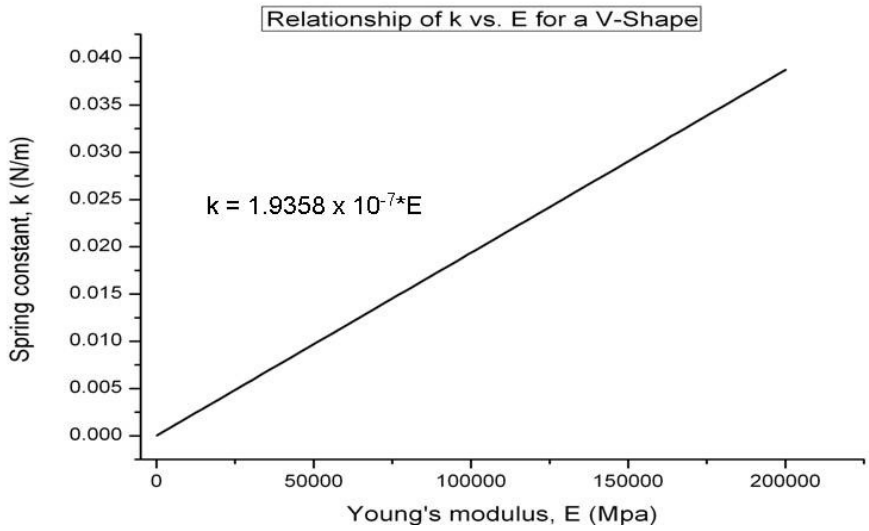

Figure 5.9 Relationship between k and E for the V-shaped cantilever

The relationship between k and E is described by the straight line fitted through the points in Figure 5.9. From this Figure the following expression relating Young's modulus and cantilever stiffness k can be derived

$$E = k / 1.9358x10^{-7} \tag{5.5}$$

Therefore with the spring constant of the cantilever used in the experiments being $\mathrm{k} = 0.03544\ \mathrm{N/m}$, then the corresponding effective Young's modulus, E, can be calculated as:

$$E = \frac{0.03544}{1.93x10^{-7}} = 183.6\ \ GPa \tag{5.6}$$

Comparing the effective value of the cantilever Young's modulus calculated using the finite element approach to the values obtained from the analytical models (Equations 5.1 to 5.4) it can be seen that the finite element result is in closer agreement with the result obtained using Sader's model [187] than with the results obtained using the other analytical methods. It was decided that the effective value of E calculated using the finite element approach would be used in the coupled fluid-solid model used to simulate the motion of the cantilever through the liquid because it was felt that this approach more accurately represents the cantilever geometry than any of the analytical models for the particular cantilever under consideration.

5.4 Fluid model.

The fluid model is developed based on the fluid shape which is formed by the physical delimitation of the glass slide (lower limit), the cantilever chip holder and the cantilever chip (upper limit) and the menisci formed due to the adhesion with the surroundings (see Figure 5.1). The dimensions of the glass slide are 5 x 5 mm and 0.5 mm thickness. The cantilever chip holder shown in Figure 5.10 is made from glass and incorporates two fluid transfer ducts that enable continuous flow experiments to be performed if required (not used in the experiments described in this thesis). The overall dimensions of the cantilever chip are shown in Figure 5.11. A clamp wire is used to fix the cantilever chip to the cantilever chip holder (Figure 5.12) however, the detail of the wire is not included in the model because it is relatively remote from the area of interest. The fluid geometry is considered to be cylindrical in shape (Figure 5.13a) i.e. the concave menisci (Figure 5.13b) are not modelled as such. These two assumptions are not expected to introduce severe errors into the model.

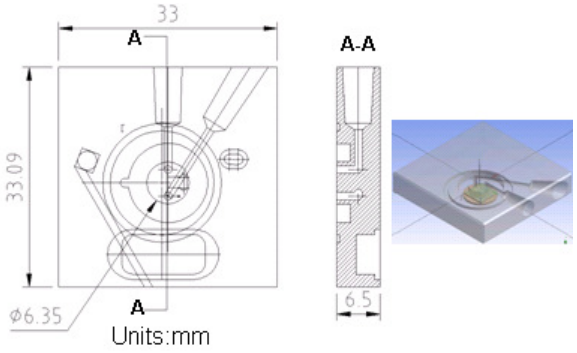

Figure 5.10 Cantilever chip holder

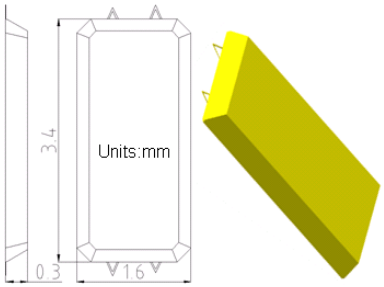

Figure 5.11 Cantilever chip

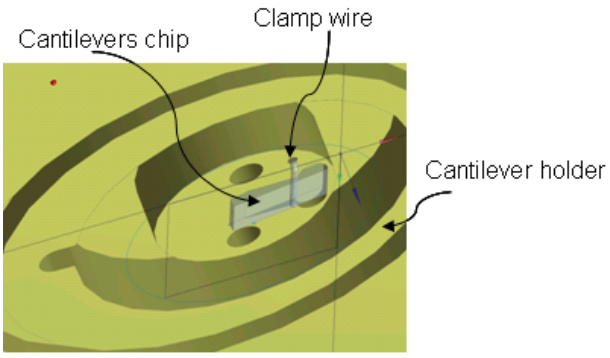

Figure 5.12 Chip fixed to the holder.

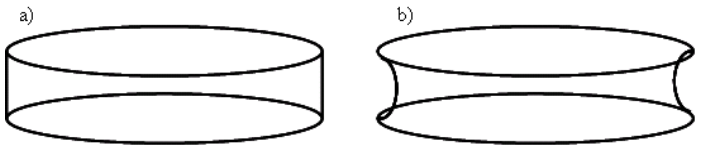

Figure 5.13 Idealised and actual fluid geometry, a) Idealised, b) Actual

The dimensions of the fluid geometry used in the coupled finite element model can be seen in Figure 5.14. Here, Xv is the thickness of the fluid. The initial fluid thickness, at the start of the experiments when the cantilever-tip separation is 6 μm, is 384.319 μm (Figure 5.14b). The platform is then displaced until the cantilever reaches the substrate; at this point the fluid thickness is reduced to 378.319 μm (Figure 5.14c).

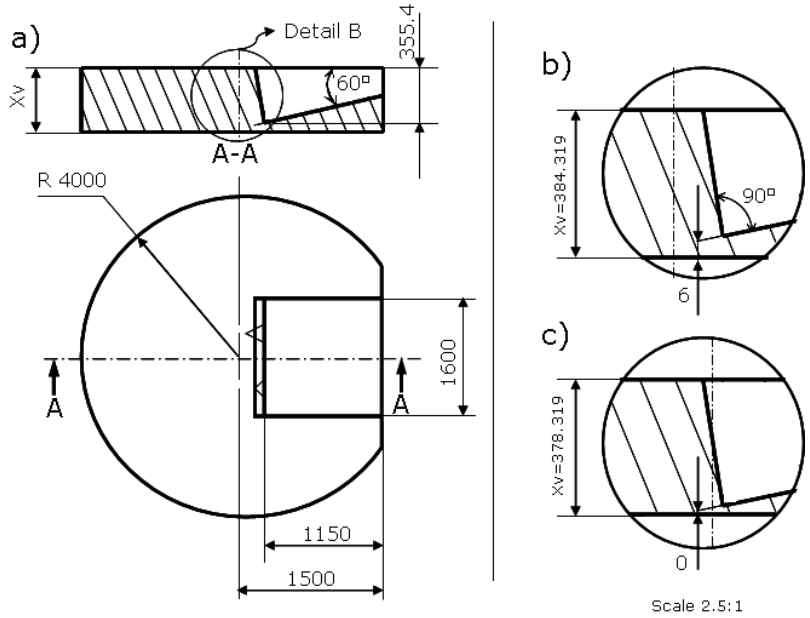

Figure 5.14 General fluid dimensions and detail B, dimensions in μm .

5.4.1 Fluid properties.

The properties of the fluids used in the coupled model and in the experimental tests are given in Table 5.8; these values were obtained using a Bohling C-VOR rheometer. Calculated Reynolds numbers for the experimental tests indicated that in all cases flow conditions were within the laminar regime.

Material	Density (kg/m3)	Dynamic viscosity (Pa.s) 20ºC
Water	0.9982	1.002 x 10-3
Polyethylene Glycol (Manufacturer: SIGMA), 300(285-315) g/mol	1.125	0.06902
Glycerol (Manufacturer:Fisher Scientific), 92.0938 g/mol	1.259	0.9604

Table 5.8 Properties at 20 ºC of fluids used in experimental tests.

5.4.2 Fluid and solid model Boundary Conditions.

The shape that the fluid medium takes in the AFM experiments is shown in Figures 5.15 and 5.16. Based on this shape the boundary conditions for the fluid model can be defined.

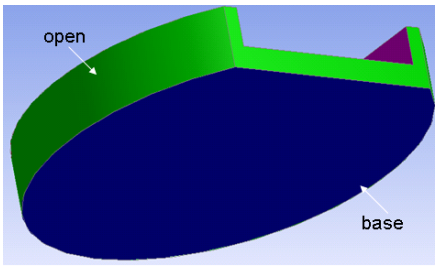

Figure 5.15 Fluid model geometry – view 1.

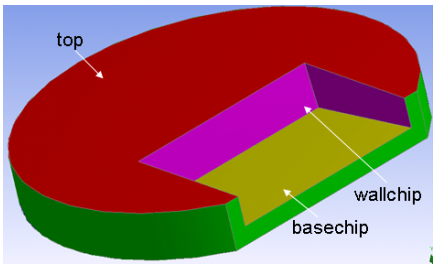

Figure 5.16 Fluid model geometry – view 2.

5.4.2.1 Surfaces open to atmosphere.

The menisci surfaces of the fluid are labelled 'open' in Figure 5.15. In the fluid model these surfaces are considered to be subjected to atmospheric pressure.

5.4.2.2 No-slip boundary conditions.

The portion of the fluid medium that contacts the glass slide is marked 'base' in Figure 5.15. The surface denoted 'top' Figure 5.16 represents the top surface of the fluid in contact with the cantilever chip holder. The areas marked 'wallchip' and 'basechip' in Figure 5.16 are the surfaces of the fluid that are in contact with walls and the base of the cantilever chip respectively. On the 'base', 'top', 'wallchip' and 'basechip' surfaces of the fluid medium a no-slip boundary condition is applied (the fluid is considered to have zero velocity relative to the solid boundary).

5.4.2.3 Specified displacement boundary conditions.

In order to simulate the motion of the cantilever through the fluid towards the substrate a specified displacement is applied to the 'base' surface, the surface of the fluid in contact with the glass slide. The value of the displacement applied is calculated given the total distance travelled (6000 nm), the total number of time steps considered and the actual time step being analysed.

5.4.2.4 Solid model: cantilever and tip model boundary conditions.

The cantilever model shown previously in section 5.3.1.5 was employed in the linked fluid/solid model of the cantilever and fluid medium.

5.4.2.5 Fixed boundary conditions.

Fixed type boundary conditions (all degrees of freedom constrained) are applied on the surfaces marked 'fixed ends' in Figures 5.7 and 5.8; these surfaces represent the surfaces of the V-shaped cantilever that are bonded to the cantilever chip.

5.4.2.6 Coupling boundary conditions.

These boundary conditions are very important as they form the coupling between the fluid and solid models enabling information to be fed between the two models. Figure 5.17 shows the fluid cantilever/tip boundary.

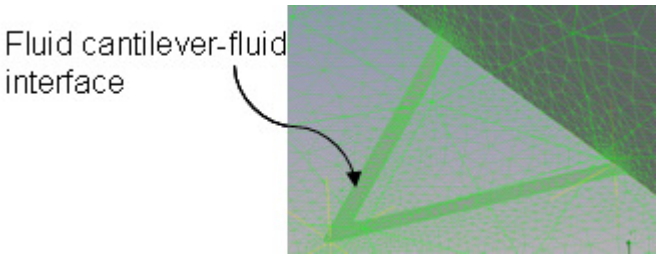

Figure 5.17 Fluid in contact with the cantilever.

5.4.2.7 Coupling fluid-solid boundary conditions.

A no slip boundary condition is applied on the cantilever surfaces in the model that are in contact with the fluid medium. Changes in cantilever shape (deformation) are fed from the solid to the fluid model.

5.4.2.8 Coupling solid-fluid boundary conditions.

In a similar manner to the fluid-solid boundary conditions, forces generated on the solid-fluid boundary calculated from the fluid model are applied in the solid model.

The ANSYS Workbench software automatically manages the coupling and linking of the cantilever and fluid medium models with force and deformation information being exchanged between the fluid and solid analysis modules during the solution process.

5.4.3 Meshes and time stepping.

The mechanical properties of the cantilever and tip used in the coupled solid-fluid model are, effective Young's modulus 183.6 GPa, density 3290 Kg/m^3, Poisson's ratio 0.27 and spring constant 0.03544 N/m.

The fluid mesh employed is shown in Figure 5.18 and the cantilever and tip mesh in Figures 5.19 and 5.20. The fluid geometry was meshed with a combination of tetrahedral, pyramidal and prism elements. The fluid mesh consisted of 462,581 4-noded linear tetrahedral elements, 3700 5-noded linear pyramidal elements and 1222 6-noded linear wedge prism elements. The cantilever and tip geometry was meshed with 5522 10-noded quadratic tetrahedral structural solid elements.

Thirty time steps were used in each of the simulations of the experimental tests. In all cases, one complete cycle was simulated. The cycle/total simulation time (t) was calculated in each case from the velocity (v) and cantilever distance (d_c) travelled, i.e. $t = d_c / v$, where d_c = 6000 nm and v = 1.05, 2.49, 4.02, 7.22, 13.1, 23.3, 30, 41.9 and 105 μm/s, yielding total simulation times ($tTime$) between 0.0571 s and 5.71 s and corresponding time step values ($tStep$) ranging from 0.0019 s to 0.19 s.

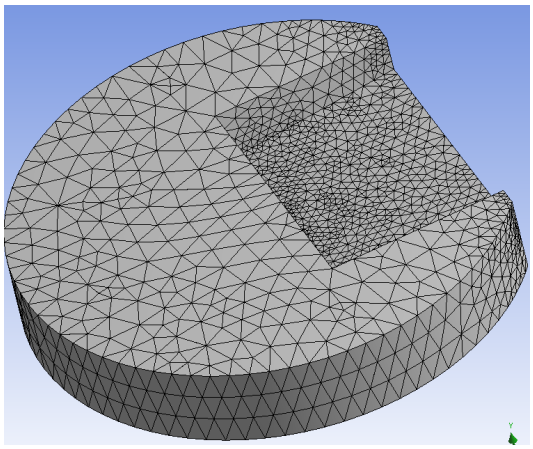

Figure 5.18 Fluid mesh.

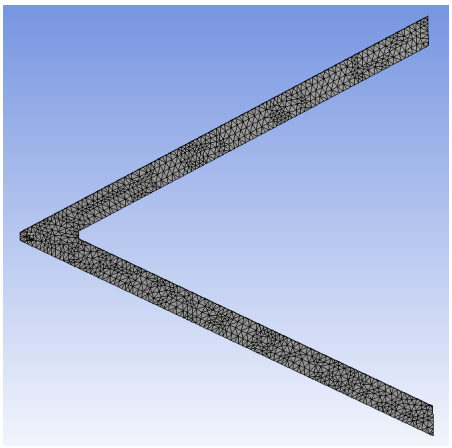

Figure 5.19 Cantilever and tip mesh.

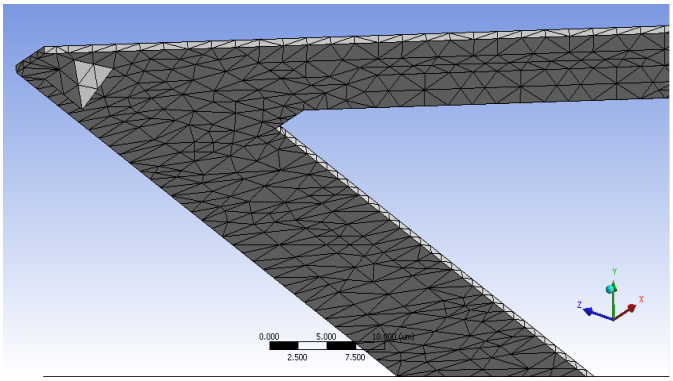

Figure 5.20 Cantilever mesh and tip detail.

5.4.4 Coupled model validation with existing analytical model.

In this section the coupled model developed is validated by comparing with the existing analytical model of Alcaraz et al. [164].

The coupled model described in this thesis has been used to quantify hydrodynamic drag force using the same cantilever geometry and cantilever and fluid properties as used by Janovjak et al. [171] when investigating the model proposed by Alcaraz et al. [164]. Results from the coupled model are compared with those from Janovjak et al. [171].

Alcaraz et al. [164] extended the spherical model of Brenner [173] and Cox and Brenner [174] to AFM cantilever geometries by scaling the dimension of the body and the distance to the substrate. In the model of Alcaraz et al. the hydrodynamic behaviour of the AFM cantilever is modelled as a drag factor, dependent on distance from the substrate (see Chapter 4, section 4.1.2.1). Two empirical coefficients are used, one to represent the effective cantilever tip

height and the other the effective radius of the cantilever. The drag force at contact is estimated by first measuring the drag factor b(h) at different tip-surface separations then extrapolating the data to obtain a value for h=0. It should be noted that the model is only valid for measurements taken in the vicinity of the sample as it predicts a drag force of zero for larger separations.

Janovjak et al. [171] quantified hydrodynamic drag force as a function of pulling speed and tip-sample separation for two V-shaped AFM cantilevers using the scaled spherical model of Alcaraz et al. Here, predictions from the numerical model described previously in this thesis are compared against the results obtained by Janovjak et al. when quantifying the model developed by Alcaraz et al. model for a small V-shaped cantilever in water. Note, it was not possible to provide predictions for comparison purposes for the second case of the larger V-shaped cantilever in PBS media as accurate PBS fluid properties could not be confirmed.

The cantilever used by Janovjak was an OTR4 Olympus, shown in Figure 5.21, having a spring constant of 0.095 N/m. The nominal dimensions of this small silicon nitride V-shaped cantilever are shown in Figure 5.22.

In order to compare the results of Janovjak with the coupled model the methodology described previously in section 5.3.1.5 was employed to calculate an effective Young's modulus for the OTR4 Olympus cantilever. The value of the effective Young's modulus calculated for this cantilever was 186.1 GPa.

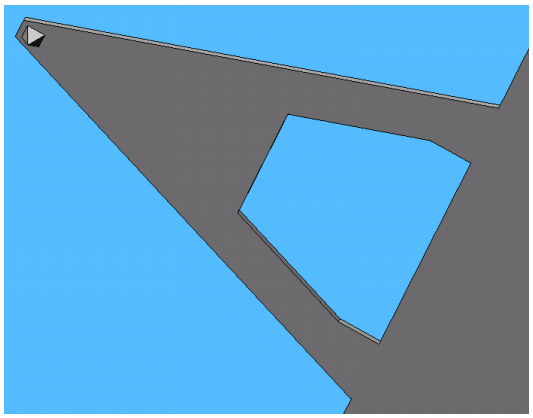

Figure 5.21 Cantilever model OTR4 Olimpus.

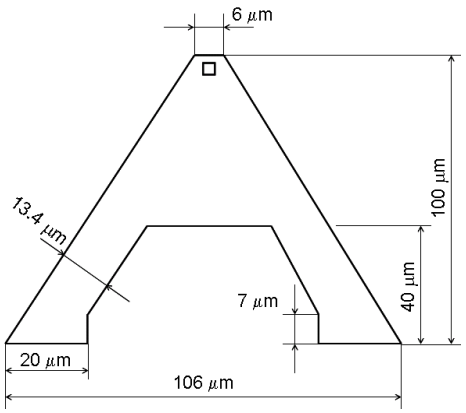

Figure 5.22 Cantilever dimensions, 0.4 µm thickness.

The results of the comparison are shown in Figures 5.23 and 5.24. Figure 5.23 is a plot of drag force versus pulling speed for the small V-shaped cantilever. The results from using the Alcaraz et al. [164] scaled spherical model are shown alongside corresponding predictions from the coupled numerical model. From this figure it can be seen that the predictions from the numerical model are in very good agreement with the empirical model of Alacaraz et al. The linear dependence of drag force on tip velocity can be clearly seen. In Figure 5.24 is plotted drag force versus tip-sample separation for the small V-shaped cantilever with coupled numerical model predictions shown alongside the results from the empirical model. Again, good agreement is obtained between the two models. The more complex dependence of drag force on tip-sample separation is evident, with an increase in drag force close to the surface being experienced. The average errors between the predictions from the novel coupled model and the empirical model are 2% for Figure 5.23 and 8% for Figure 5.24.

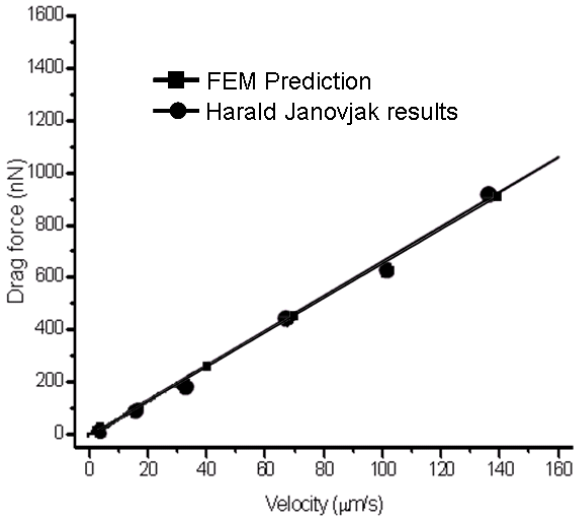

Figure 5.23 Drag force versus tip velocity for tip-sample separation of 500nm. Comparison with empirical model of Alcaraz et al. [164].

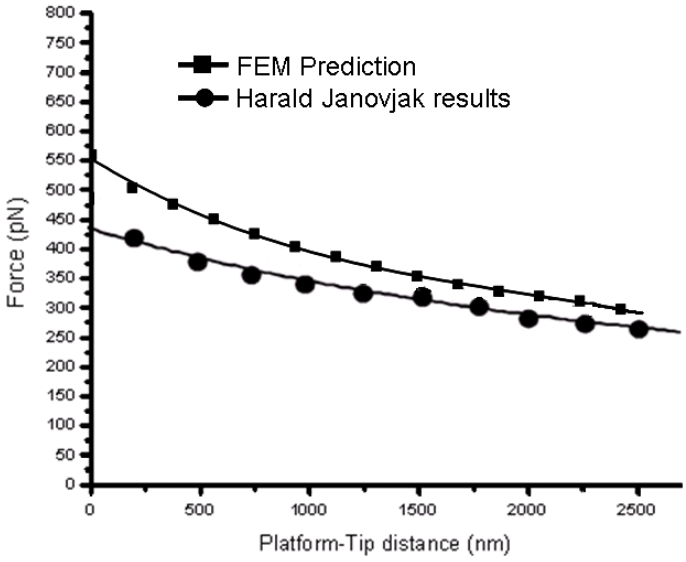

Figure 5.24. Drag force versus tip-sample separation for tip velocity of 70μm/s. Comparison with empirical model of Alcaraz et al. [164].

5.5 Experimental work.

In order to further validate the coupled model extensive experimental work was undertaken using an AFM. The experiments involved making drag force measurements in fluids of differing viscosities, using a range of cantilever velocities at varying tip-sample separations for a variety of substrates.

5.5.1 Experimental set-up.

Drag force measurements were carried out in three fluids of different dynamic viscosities and densities, polyethylene glycol (Sigma UK, Poole, UK), glycerol (Fisher Scientific UK Ltd, Loughborough, UK) and water on glass, mica and stainless steel substrates. The measurements were carried out at room temperature using a commercially available Picoforce Multimode AFM (Veeco, Cambridge, UK). The AFM was equipped with a piezoelectric ceramic scanner enabling movement along the main X, Y and Z axes. A silicon nitride V-shaped probe comprising a cantilever (Veeco, Cambridge, UK) of dimensions, length 196 μm, width 15 μm, and thickness 0.6 μm, and a silicon nitride pyramidal tip of height 3 μm was employed for the tests. The determination of the spring constant of the probe was undertaken in fluid using the in-built Thermal Tune Method [159] prior to commencement of the experiments.

In the experimental tests 30 μl of fluid was deposited on a piece of glass slide of dimension 5 x 5 mm, the glass slide having first been cleaned by being

immersed in ethanol for 20 minutes then rinsed with distilled water. Measurements were taken in each fluid with the cantilever moving at constant velocity from 600 nm above the platform until the tip was brought into contact with the glass surface. Nine different velocities were employed, 1.05, 2.49, 4.02, 7.22, 13.1, 23.3, 29.9, 41.9 and 105 μm/s.

In each test the surface of the substrate was first located by moving the cantilever slowly down until contact was made with the surface, this was achieved using the 'engage' function available on the microscope. Once the surface had been located the desired displacement (6000 nm scanner displacement) and cantilever velocity were set. The AFM was operated in static (contact) mode and force curves were obtained for each test. The sampling frequency was adjusted so that 2048 points/cycle were obtained. Each experimental test was performed seven times in order to ensure repeatability of the results.

5.5.2 Methodology for determining drag force from experimentation.

In order to explain how drag force results were obtained from the force curves produced from the experimental tests it is convenient to consider the approach curve from one of the tests undertaken. Figure 5.25 shows an approach curve, consisting of 1024 data points, obtained from an AFM experiment in water using a glass substrate with the platform moving towards the cantilever and tip at a constant velocity of 41.9 $\mu m/s$ from an initial (vertical) distance of 600 nm away. The point marked **A** in this figure denotes the start of the displacement, the point at which the platform begins to move towards the cantilever and tip. Point **B** indicates the cantilever-platform contact point. The analysis will focus on the zone between **A-B** where the cantilever interacts only with the fluid and the substrate makes no contribution to the force measured by the AFM.

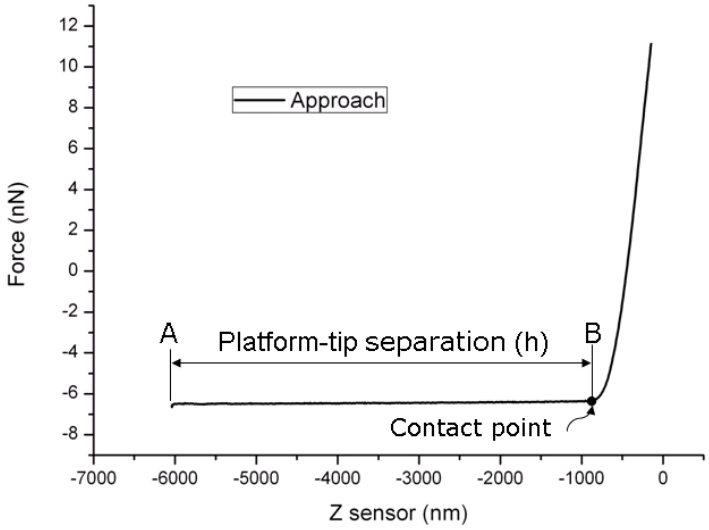

Figure 5.25 Analysis of approach force curve for drag force determination.

At point **A**, the cantilever tip-platform separation, *h,* is at its maximum and the force is zero. At point **B**, $h = 0$ and the force is at its maximum. The distance between these points is the total platform displacement, where no substrate interaction takes place.

Next, the portion of Figure 5.25 of interest, the section between points **A** and **B**, is considered in more detail, as shown in Figure 5.26. Note, the X axis has been rearranged for clarity. Between points **A** and **B** the cantilever interacts only with the fluid, therefore the force on the cantilever tip measured between these points is due only to this interaction i.e. it is the hydrodynamic drag force. At the tip-platform contact point **B**, the platform has moved a distance 5167.5 nm from its initial position and the drag force has reached its maximum at approximately 0.3 nN.

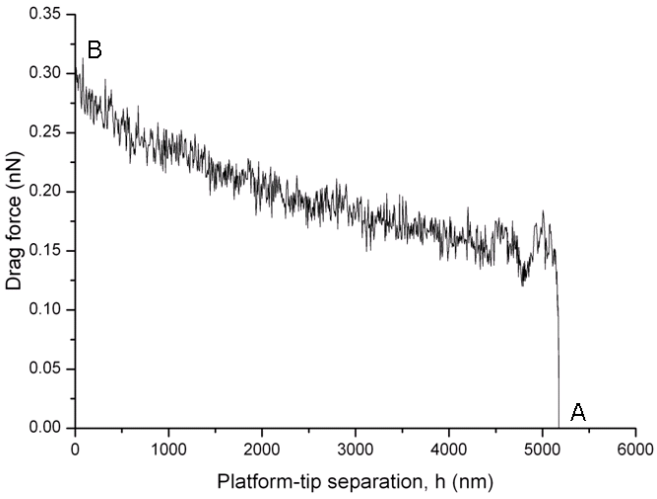

Figure 5.26 Force curve for section A-B.

The final step involved in extracting drag force data from the force curves obtained from the experimental tests consists of fitting a polynomial function through the force curve data for section **A**-**B** shown in Figure 5.25. This approach effectively filters out any noise from the results. Figure 5.27 shows the resulting polynomial curve for this example.

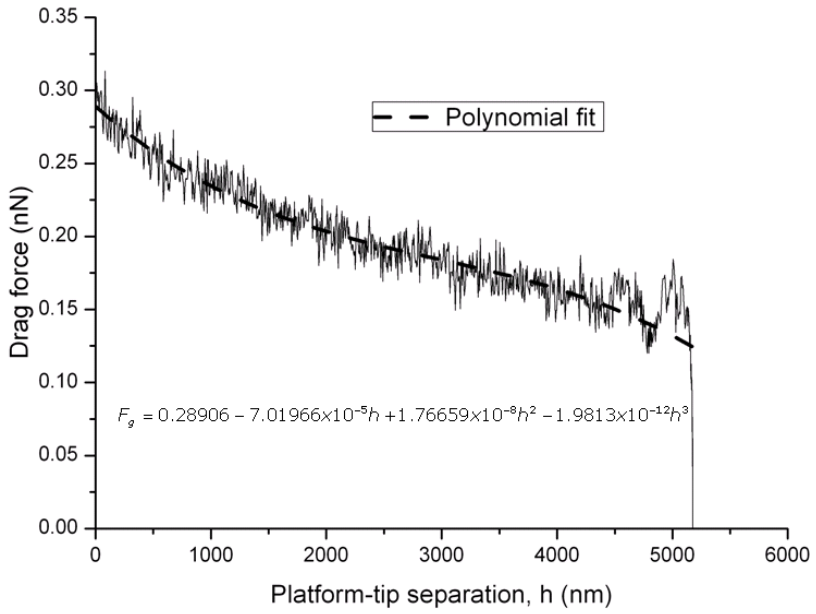

Figure 5.27 Polynomial function fitted in the drag force curve.

This methodology was employed to extract hydrodynamic drag force data from the AFM force curves obtained from the experimental tests described in this thesis.

5.6 Results and discussion.

In this section the experimental results obtained from AFM tests are compared against corresponding predictions from the numerical model.

The series of experimental tests undertaken enabled:

the investigation of the influence of velocity on hydrodynamic drag force for particular tip-sample separations in polyethylene glycol, glycerol and water, with a glass substrate;

the investigation of the influence of tip-sample separation on hydrodynamic drag force for particular velocities in polyethylene glycol, glycerol and water, with a glass substrate.

the investigation of the influence of substrate material (mica, stainless steel and glass) on hydrodynamic drag force.

5.6.1 Comparison of experimental results with coupled model predictions.

The fluids used in the experimental tests were chosen to provide a range of viscosities (low, medium and high). Although extensive data was obtained from the experiments, for comparison purposes three velocities (1.05, 13.1 and 105 μm/s) and three tip-sample separations (0, 300 and 600 nm) were considered, as it was felt that this would be sufficient to enable a detailed analysis and comparison with coupled model predictions.

5.6.2 The influence of velocity on hydrodynamic drag force.

Figures 5.28, 5.29 and 5.30 are plots of drag force versus tip velocity for tip-surface separations of 600, 300 and 0 nm respectively for the three fluid media for the case of the glass substrate. Note, experimental results were not obtained for the high viscosity fluid, glycerol, at velocities exceeding 13.1 μm/s as the bending of the cantilever at these velocities was such that the laser of the AFM fell outside the useful measuring range of the quadrant cell detector.

The mean results are shown for the experimental data in plots Figures 5.28, 5.29 and 5.30 along with standard deviation, however, the standard deviation values are difficult to make out in this case as their values were very small (average standard deviation is ± 0.05 nN).

Upon inspection of Figures 5.28, 5.29 and 5.30 it can be seen that the shape of the plots is very similar in nature for the three tip-surface separations shown. In terms of the experimental results shown in these figures it can be seen that as expected, drag force increases with velocity. In addition, the relationship between drag force and tip velocity is approximately linear in nature. This finding is in agreement with those of the investigation undertaken by Janovjak et al. [171] and is further validated by the predictions from the numerical model which are also shown in Figures 5.28, 5.29 and 5.30. The influence of the fluid viscosity on drag force is also readily discernible from the plots; for a given velocity, drag force increases with fluid viscosity. The average error between the numerical predictions and the experimental results shown in Figures 5.28, 5.29 and 5.30 is 15%.The largest differences between numerical drag force

predictions and experimental results tend to occur at the higher tip velocities in the fluids of greater viscosity and this may be explained by the fact that the linear relationship between the quadrant cell detector response to laser position is only valid up to a certain deviation from the centre of the QCD and that Hooke's Law, used to determine the force from the deflection of the cantilever, is only applicable for small deflections.

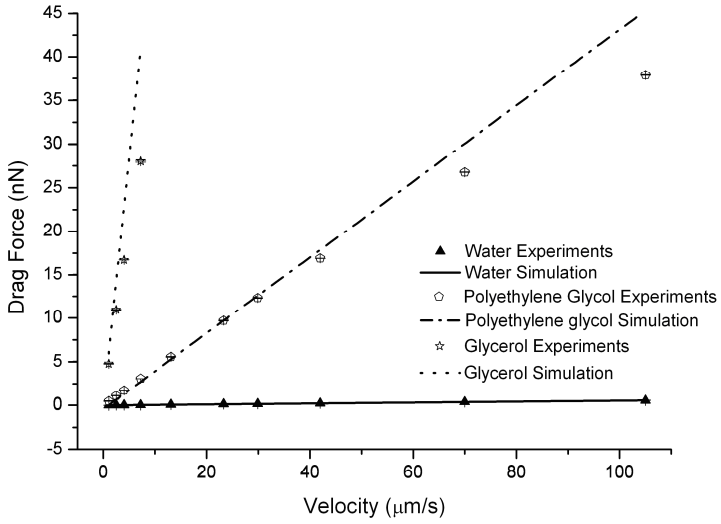

Figure 5.28 Glass substrate: drag force versus velocity for tip-surface separation of 600 nm.

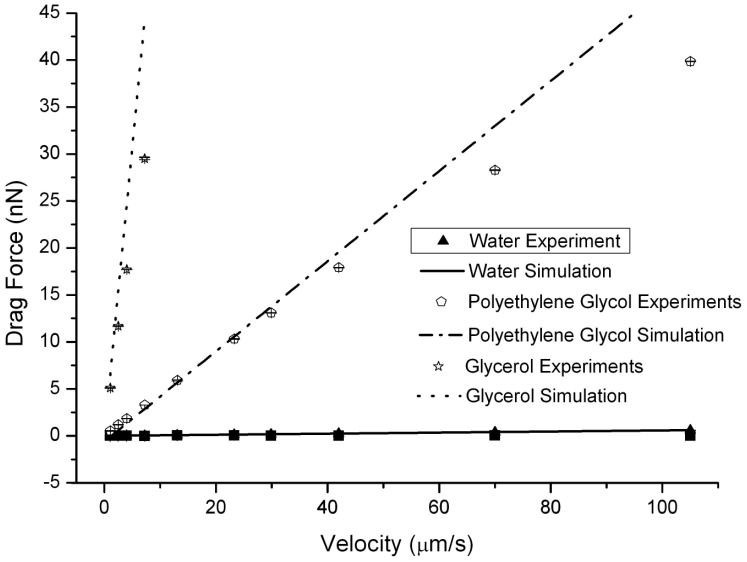

Figure 5.29 Glass substrate: drag force versus velocity for tip-surface separation of 300 nm.

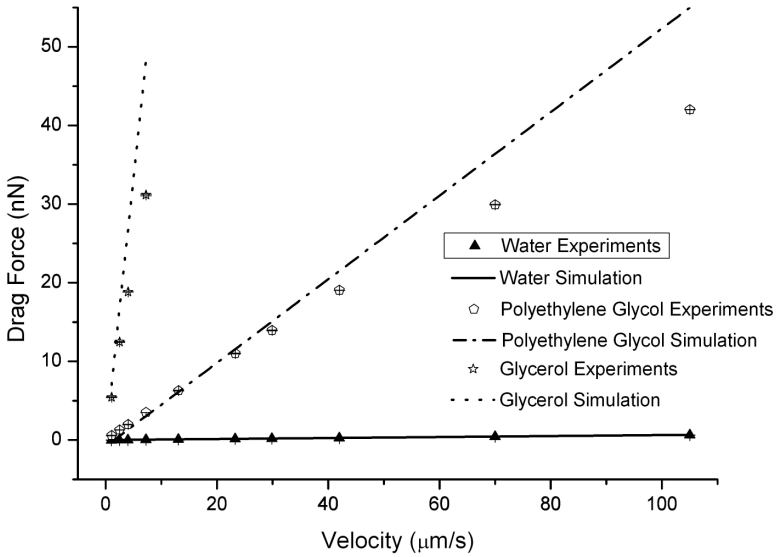

Figure 5.30 Glass substrate: drag force versus velocity for tip-surface separation of 0 nm.

5.6.3 The influence of tip-sample separation on hydrodynamic drag force

Figures 5.31, 5.32 and 5.33 are plots of drag force versus tip-surface separation for velocities of 1.05, 13.1 and 105 μm/s respectively for the three fluid media for the case of the glass substrate. It can be seen from these figures that the shape of the plots is similar in nature for the three tip velocities considered. Upon inspection of the experimental results shown in Figure 5.31, 5.32 and 5.33 it can be seen that an increase in drag force occurs as the cantilever tip approaches the surface. This is particularly discernible in the higher viscosity fluid media (polyethylene glycol and glycerol) and is in accordance with the findings of other researchers including Roters and Johannsmann 1996 [192] and Ma, Jimenez and Rajagopalan 2000 [170]. This increase in drag force at small tip-sample separations is also predicted by the numerical model. Once again, the influence of the fluid viscosity on drag force can be readily observed. The average error between the numerical predictions and the mean experimental results shown in Figures 5.31-5.33 is 7%. The biggest discrepancies between numerical drag force predictions and experimental results are found for the fluid of highest viscosity (glycerol) and as mentioned previously this could be explained by the fact that the linear relationship between the quadrant cell detector response to laser position is only valid up to a certain deviation from the centre of the QCD and that Hooke's Law, used to determine the force from the deflection of the cantilever, is only applicable for small deflections.

The average standard deviations (SD) for the experimental data shown in plots Figures 5.31, 5.32 and 5.33 can be found in Tables 5.9, 5.10 and 5.11 respectively.

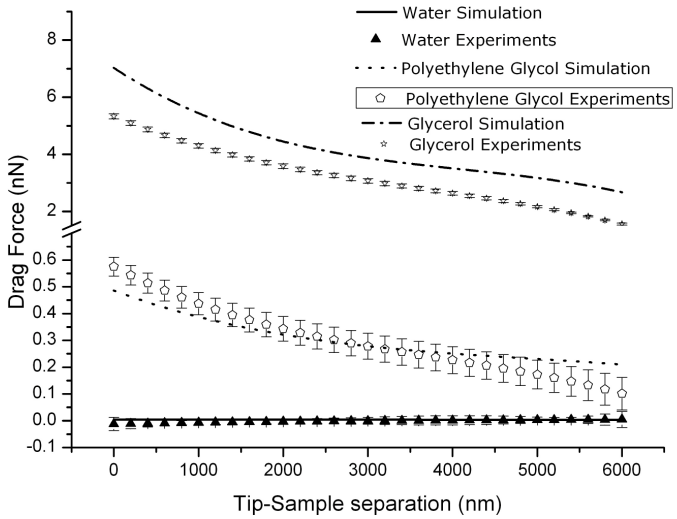

Figure 5.31 Glass substrate: drag force versus tip-surface separation for velocity of 1.05 µm/s

Fluid	Polyethylene	Water	Glycerol
SD (nN)	0.047819	0.02468	0.065195

Table 5.9 SD average for plot Figure 2.31

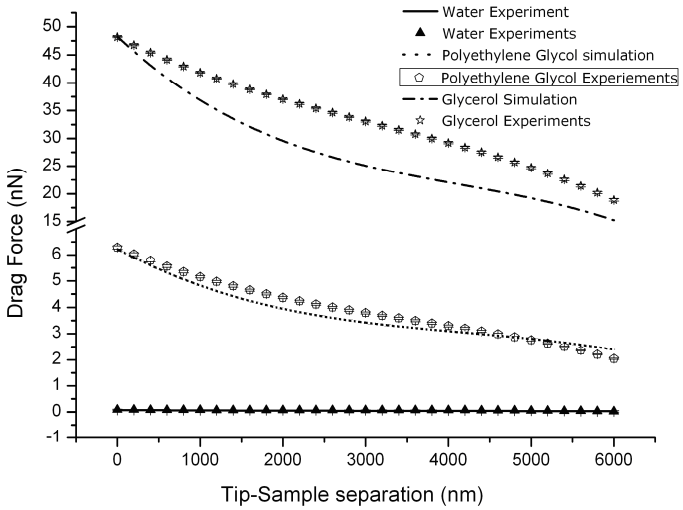

Figure 5.32 Glass substrate: drag force versus tip-surface separation for velocity of 13.1 µm/s

Fluid	Polyethylene	Water	Glycerol
SD (nN)	0.037254	0.008549	0.142091

Table 5.10 SD average for plot Figure 5.32

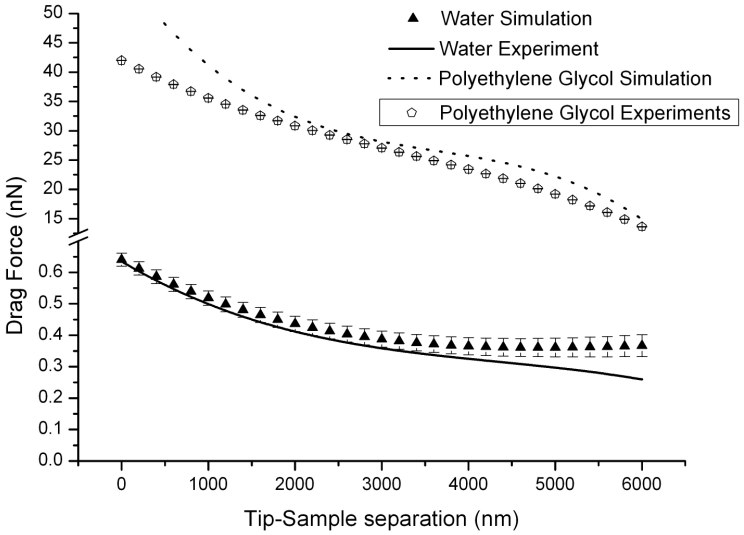

Figure 5.33 Glass substrate: drag force versus tip-surface separation for velocity of 105 μm/s

Fluid	Polyethylene	Water
SD (nN)	0.033868	0.026395

Table 5.11 SD average for plot Figure 5.33.

5.6.4 The influence of substrate material on hydrodynamic drag force

Figures 5.34 to 5.39 and 5.40 to 5.45 are the corresponding plots for the two additional substrates tested, mica and stainless steel respectively. Upon inspection of these figures it can be seen that the experimental results and numerical predictions are similar in form to those obtained for the glass substrate, shown in Figures 5.28 to 5.33. Therefore, the same discussions apply and similar conclusions can be drawn for the mica and stainless steel substrates as for the glass substrate.

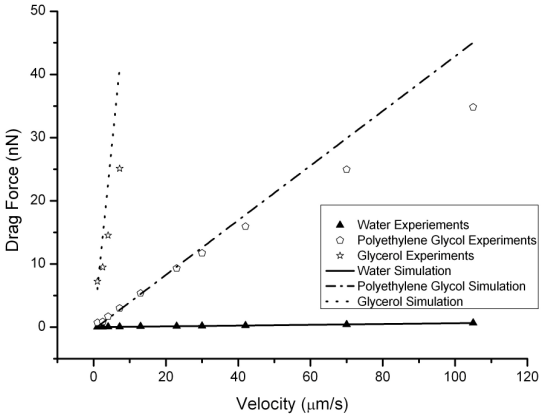

Figure 5.34 Mica substrate: drag force versus velocity for tip-surface separation of 600 nm.

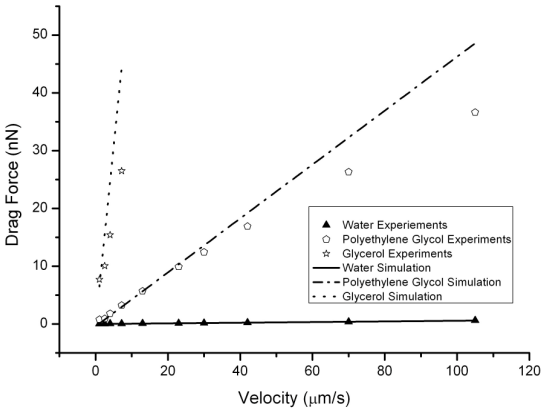

Figure 5.35 Mica substrate: drag force versus velocity for tip-surface separation of 300 nm

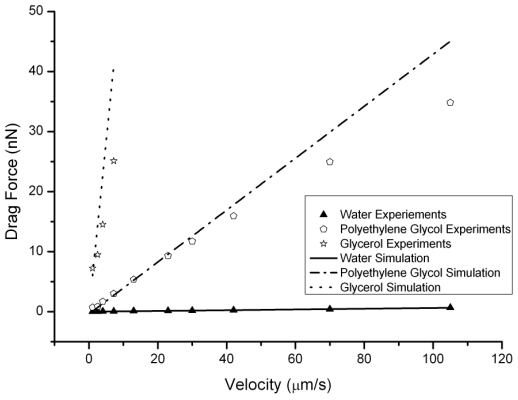

Figure 5.36 Mica substrate: drag force versus velocity for tip-surface separation of 0 nm

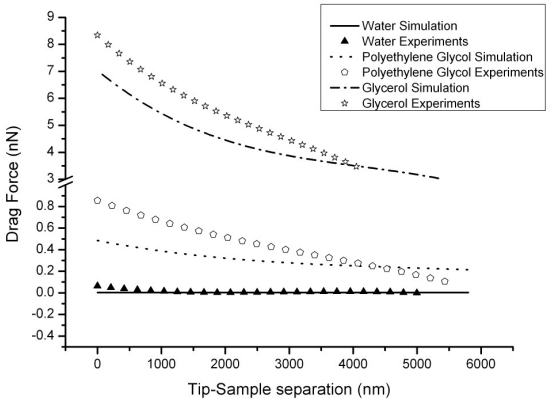

Figure 5.37 Mica substrate: drag force versus tip-surface separation for velocity of 1.05 μm/s

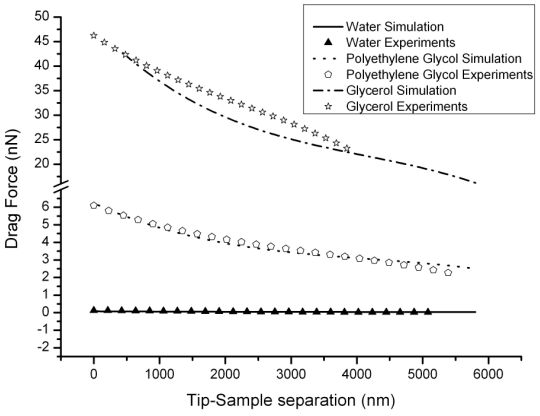

Figure 5.38 Mica substrate: drag force versus tip-surface separation for velocity of 13.1 μm/s.

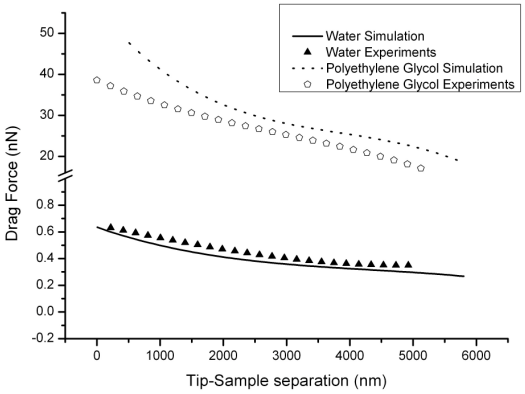

Figure 5.39 Mica substrate: drag force versus tip-surface separation for velocity of 105 μm/s.

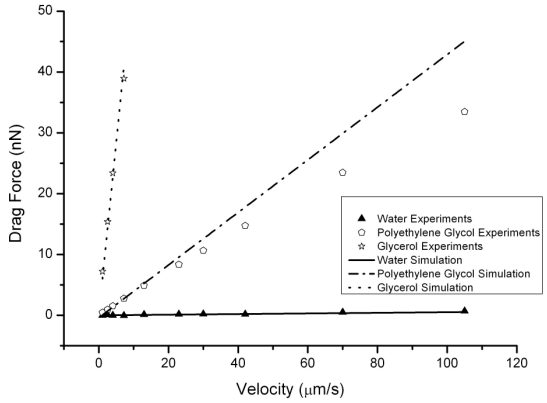

Figure 5.40 Metallic substrate: drag force versus velocity for tip-surface separation of 600 nm.

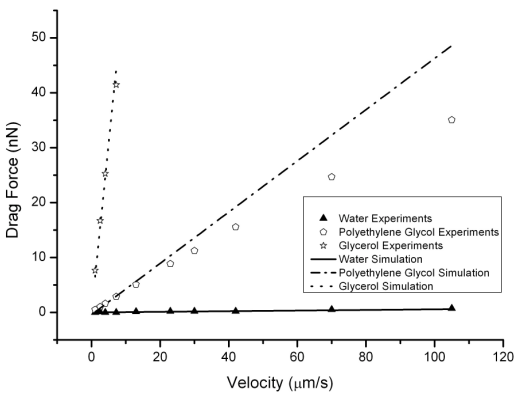

Figure 5.41 Metallic substrate: drag force versus velocity for tip-surface separation of 300 nm.

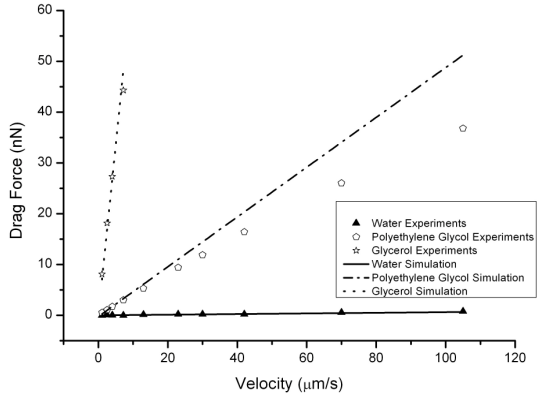

Figure 5.42 Metallic substrate: drag force versus velocity for tip-surface separation of 0 nm

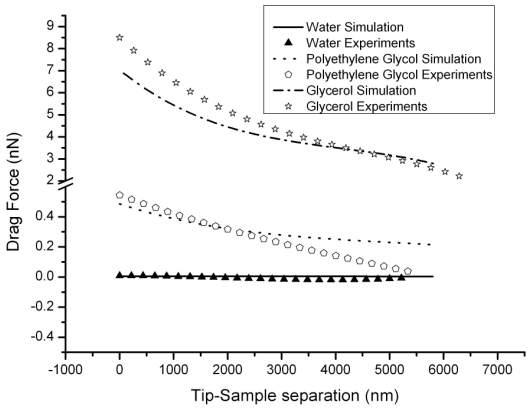

Figure 5.43 Metallic substrate: drag force versus tip-surface separation for velocity of 1.05 μm/s

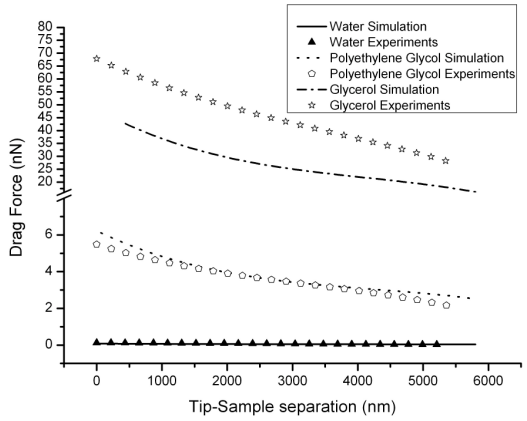

Figure 5.44 Metallic substrate: drag force versus tip-surface separation for velocity of 13.1 μm/s

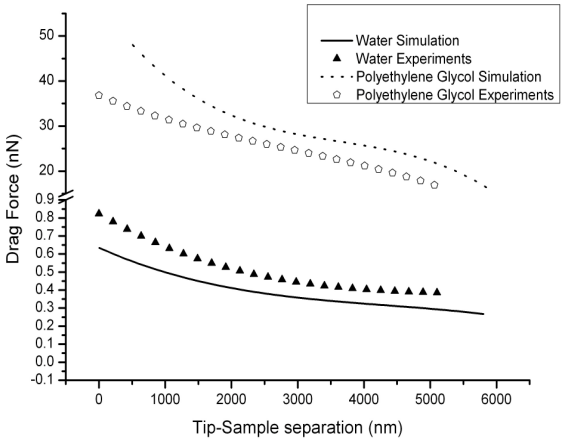

Figure 5.45 Metallic substrate: drag force versus tip-surface separation for velocity of 105 μm/s

Figure 5.46 is a plot of drag force versus tip velocity for a tip-surface separation of 300 nm for polyethylene glycol fluid on the glass, mica and metallic (stainless steel) substrates. Figure 5.47 shows a plot of drag force versus tip separation for a velocity of 13.1 μm/s for polyethylene fluid on the three substrates. The experimental results shown in Figures 5.46 and 5.47 indicate that whilst the results from the three substrates are similar, drag forces are generally greater for the glass substrate than for the mica and metallic substrates. In addition, drag forces are generally lower on the metallic substrate than on the mica substrate. The numerical predictions for the three substrates are however, identical which indicates that additional forces may be playing a role in the experimental results, forces which are not accounted for by the numerical model. Although the experimental results indicate that these additional forces are relatively small in magnitude, further investigation may reveal their source and enable the numerical model to be modified in order to take these forces into account.

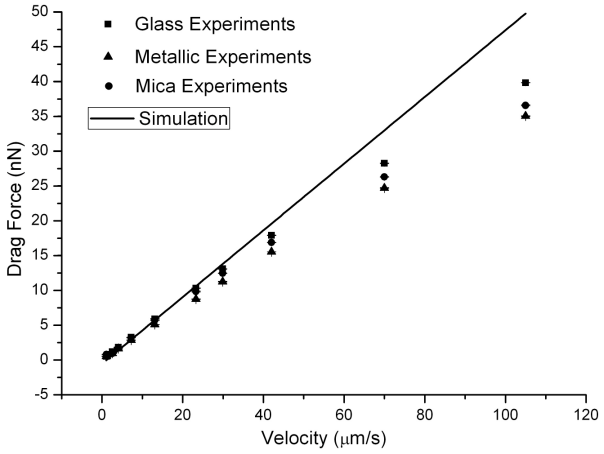

Figure 5.46 Drag force versus tip velocity for tip-surface separation of 300 nm for polyethylene fluid on glass, mica and metallic substrates.

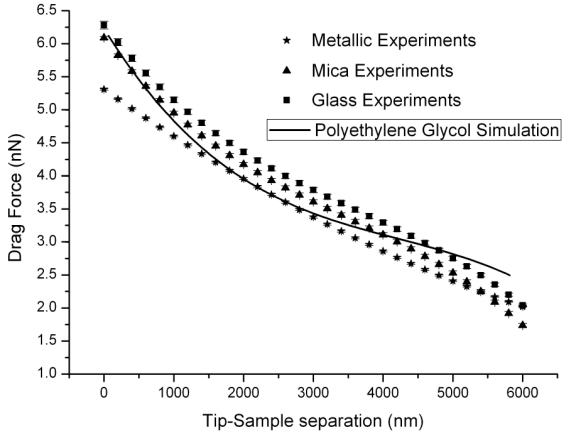

Figure 5.47 Drag force versus tip separation for a velocity of 13.1 μm/s for polyethylene fluid on glass, mica and metallic substrates.

5.7 Example of using the numerical model to correct for drag force in AFM measurements of keloid cells.

A primary motivation for developing the model described in this thesis was to be able to determine the mechanical properties of biological samples in fluids using AFM to high accuracy and to have increased confidence in the results obtained.

One application of particular interest to the author is the investigation of the mechanical properties of keloid cells. Having undertaken the testing and validation described previously, the numerical model was subsequently used to correct measurements undertaken on keloid cells using the AFM described in the experimental section of this thesis. The AFM was employed in contact mode and force-indentation curves were obtained for keloid cells in PBS using indentation velocities of 5, 10.5, 30 and 42 and 105 μm/s.

In order to demonstrate how the coupled model was employed to correct for drag force in the AFM investigation of keloid cells, consider the case of highest indentation velocity, 105 μm/s used in the experiments. Figure 5.48 is the approach curve for this case. Point **a** in Figure 5.48 corresponds to the initialization of the displacement, the point at which the platform holding the sample begins to move towards the cantilever and tip. Point **b** is the point at which the cantilever tip first makes contact with the sample. Therefore **a-b** represents the period during which the platform moves towards the sample, prior to contact. Between **b-c** the cell is being indented by the cantilever tip. Point **c** represents the point at which the cell has been penetrated completely, and the hard substrate (glass) is reached. Between **c-d** the plot is almost vertical, which is typical when a hard substrate is indented. Points **b** and **c** can be used to calculate the cell thickness, i.e. the distance in the Z sensor readings between points **b** to **c** is the cell thickness.

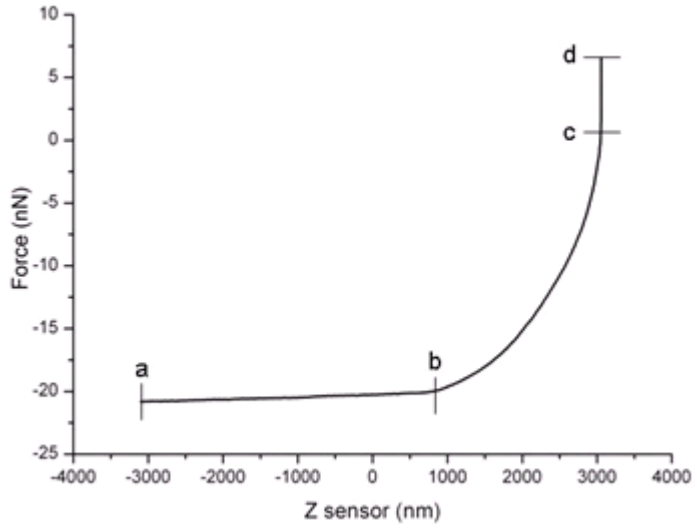

Figure 5.48 Approach force curve.

In order to determine the apparent Young's modulus from the experimental results it is convenient to consider the section of the plot between point **b** and **c** in more detail, as shown in Figure 5.49. Note that the origin of the X axis has been shifted from that in Figure 5.48 using the expression (Indentation =Z sensor – Deflection of the cantilever, δ), so that point **b,** the point at which the cantilever tip first makes contact with the sample, prior to cell penetration by the cantilever tip, is now located at zero displacement. This enables the X axis to be more conveniently relabelled as cell indentation rather than Z sensor displacement. The cell thickness can then be easily obtained from this plot, as it is now simply the indentation value at point **c**, which in this example is $2243\,nm$.

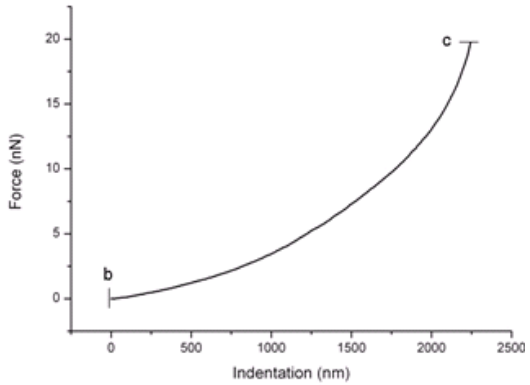

Figure 5.49 Force curve for the cell indentation example.

This implies that the cantilever tip is initially 2243 nm above the surface of the substrate at the point when it initially makes contact with the sample, very useful data that enables the value of the drag force in the cell experiments

where no samples were used to be determined at the point corresponding to the tip-sample contact point using the polynomial expression used to fit the experimental data, as described previously in section 5.5.2. This data can subsequently be used to correct measurements taken during the cell indentation tests. It also enables model predictions of hydrodynamic drag force to be obtained at the point corresponding to the tip sample contact point thus facilitating correction of experimental results obtained for cell indentation using coupled model predictions. Equation (5.7) below is the polynomial expression used to fit the experimental data obtained for the case of an indentation velocity of 105 μm/s in PBS, with no sample present. This expression for drag force is a function of tip-substrate separation, h. The initial value of h is the contact point, the point at which the cantilever tip first makes contact with the sample. This value, which corresponds to the cell thickness (see Figure 5.50), is calculated from the approach force indentation curve as previously described.

$$F_d = 2.394x10^{-12}(h)^3 + 3.14253x10^{-8}(h)^2 - 1.64971x10^{-4}(h) + 0.63521 \quad (5.7)$$

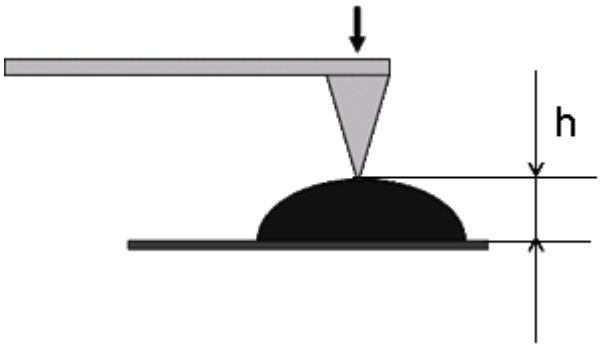

Figure 5.50 Thickness cell (h).

Initially no correction was made for the drag force and the apparent Young's modulus was calculated by fitting the force-indentation curve obtained from the cell indentation experimental results using Hertz's Model as shown in Figure 5.51.

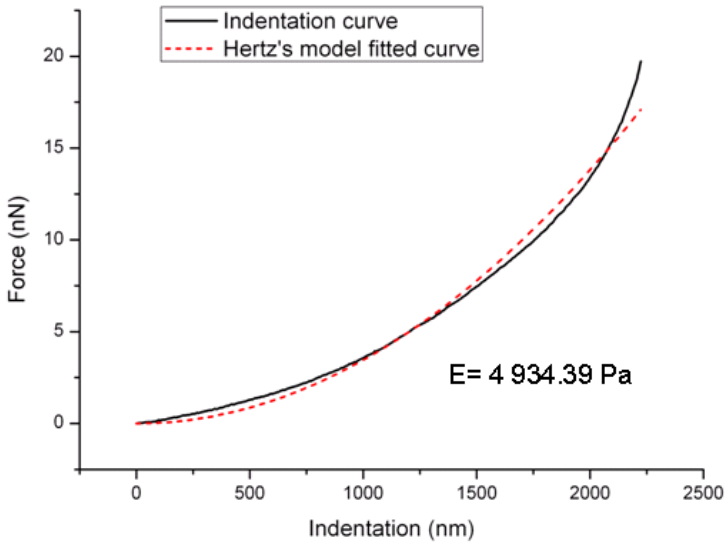

Figure 5.51 Fitted force-indentation curve for indentation velocity of 105 μm/s: no correction for drag force.

With no correction for drag force a value of 4934.39 Pa was obtained for Young's modulus.

Finally, the above exercise was repeated however in this case the force indentation curve was corrected using Equation (4.7). The resulting Young's modulus calculated using this corrected data was 4832.84 Pa, Figure 5.52.

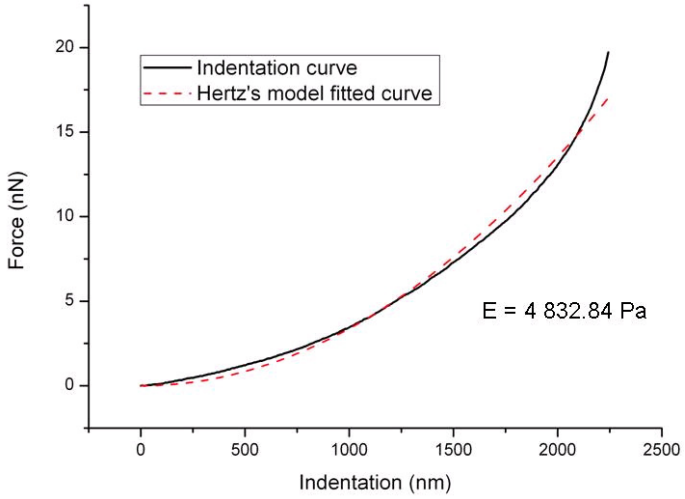

Figure 5.52 Fitted force-indentation curve for indentation velocity of 105 μm/s: with correction for drag force.

The difference in the uncorrected and corrected values for Young's modulus is approximately 3.25%, a relatively low value.

In order to further verify the process experiments were undertaken on an additional 6 keloid cells.

Indentation tests were performed on each cell for velocities of 5, 10.5, 30 and 42 μm/s. The apparent Young's modulus was calculated in each case using the fitting of force-indentation curve obtained from the experimental results using Hertz's Model. The numerical model was then used to correct the experimental results for hydrodynamic drag effects. The Young's modulus was then calculated using the corrected data. Tables 5.12-5.17 shows the results obtained in the measurements made on these 6 cells and the uncorrected and corrected apparent Young's modulus values. The percentage difference between the uncorrected and corrected values for Young's modulus (E) are also given.

Cell 1						
		Uncorrected for drag force		Corrected for drag force		
Velocity (μm/s)	Cell thickness (nm)	E (Pa)	Max. force (nN)	E (Pa)	Max. force (nN)	Error %
5	2334.4	2819.9	6.6	2815.6	6.5	0.15
10.5	2548.2	2384.6	6.7	2373.2	6.7	0.48
30	1472.4	7677	6.8	7615.5	6.8	0.8
42	1700.7	5787.5	7.3	5712.4	7.2	1.31

Table 5.12 Results for cell No 1.

Cell 2						
		Uncorrected for drag force		Corrected for drag force		
Velocity (μm/s)	Cell thickness (nm)	E (Pa)	Max. force (nN)	E (Pa)	Max. force (nN)	Error %
5	2084.3	3542.9	6.6	3537.8	6.6	0.14
10.5	1909.6	4083.1	6.4	4065.5	6.4	0.43
30	1723.8	5864.6	7.6	5816	7.6	0.83
42	1581.2	6549	7.3	6465.0	7.3	1.29

Table 5.13 Results for cell No 2.

Cell 3						
		Uncorrected for drag force		Corrected for drag force		
Velocity (μm/s)	Cell thickness (nm)	E (Pa)	Max. force (nN)	E (Pa)	Max. force (nN)	Error %
5	2745	1918.3	6.7	1915	6.7	0.17
10.5	2597.7	2550.4	8.0	2539.3	8	0.43
30	2078.9	3852.7	7.5	3816.5	7.4	0.94
42	1943.1	5314.8	8.9	5254.3	8.8	1.15

Table 5.14 Results for cell No 3.

Cell 4						
		Uncorrected for drag force		Corrected for drag force		
Velocity (μm/s)	Cell thickness (nm)	E (Pa)	Max. force (nN)	E (Pa)	Max. force (nN)	Error %
5	2514.3	3074.9	6.8	3070.5	6.8	0.14
10.5	2324.6	2513.1	7.6	2494.6	7.5	0.74
30	2270	4108.4	9.9	4070	9.7	0.94
42	2288.4	4443.1	10.2	4388.5	10	1.24

Table 5.15 Results for cell No 4.

Cell 5						
		Uncorrected for drag force		Corrected for drag force		
Velocity (μm/s)	Cell thickness (nm)	E (Pa)	Max. force (nN)	E (Pa)	Max. force (nN)	Error %
5	1934.5	3608.5	5.5	3602.8	5.5	0.14
10.5	1958.4	5404.5	8.9	5387.5	8.8	0.28
30	2082.6	5648.1	10.9	5612.1	10.8	0.58
42	1799.3	7278.5	11.2	7210.1	11.1	0.8

Table 5.16 Results for cell No 5.

Cell 6						
		Uncorrected for drag force		Corrected for drag force		
Velocity (μm/s)	Cell thickness (nm)	E (Pa)	Max. force (nN)	E (Pa)	Max. force (nN)	Error %
5	2270.2	3430.3	9.4	3435.45	9.4	0.14
10.5	2206.7	5226.3	7.6	5242.5	7.6	0.30
30	1879.2	5469.9	10.2	5504.91	10.1	0.63
42	1852.4	7100.3	10.2	7167.04	10.2	0.93

Table 5.17 Results for cell No 6.

Analysing the results shown in these tables it can be seen that the error in apparent Young's modulus by not accounting for hydrodynamic drag increases with indentation velocity, the highest error being for the velocity of 42 μm/s in each cell. Table 5.18 shows the average percentage errors for velocities of 5, 10.5, 30 and 42 μm/s.

Velocity (μm/s)	Error % average
5	0.15
10.5	0.44
30	0.79
42	1.12

Table 5.18 Error percentage average.

These results indicate that the percentage error between the uncorrected and the corrected Young's modulus calculations is relatively small for the keloid cells tested. Additional errors may be introduced, however, due to uncertainties in the selection of the contact point and uncertainties in the determination of the cantilever spring constant. Given these results it was decided that it would not be necessary to correct the Young's modulus in the cell experimental work detailed in Chapter 6. However, in low stiffness cases the correction of Young's modulus to take into account drag force is still necessary.

5.8 Drag force simulation including cell geometry.

The model utilised in the previous section to calculate hydrodynamic drag force does not consider the possible influence of the presence of the cell on the hydrodynamic drag forces generated. In this section the effect on hydrodynamic drag force of considered the physical presence of the cell is investigated. In order to calculate the drag forces when the cell is included in the model a modification to the previous model (section 5.4) is carried out. The simplified cell geometry shown in Figure 5.53 with dimensions detailed in Figure 5.54 was incorporated in the model. In practice the exact cell geometry is difficult to obtain and it varies enormously from cell to cell, however, the use of the approximate cell geometry shown in Figures 5.53 and 5.54 is adequate for this investigation.

The fluid geometry (section 5.4) was meshed with a combination of tetrahedral, pyramidal and prism elements: 470,840 4-noded linear tetrahedral elements, 1221 5-noded linear pyramidal elements and 3717 6-noded linear wedge prism elements were employed. The cantilever and tip geometry was meshed with 5522 10-noded quadratic tetrahedral structural solid elements. Water was considered as the fluid medium.

Eighteen time steps were used in the simulation as in this case the cantilever is displaced a sorter distance compared with previous model (section 5.4.3). The

cantilever tip is initially at a distance of d_c = 6000 nm above the platform and a cantilever tip velocity of 30 μm/s is employed. The total distance travelled in this simulation is (4000 nm).

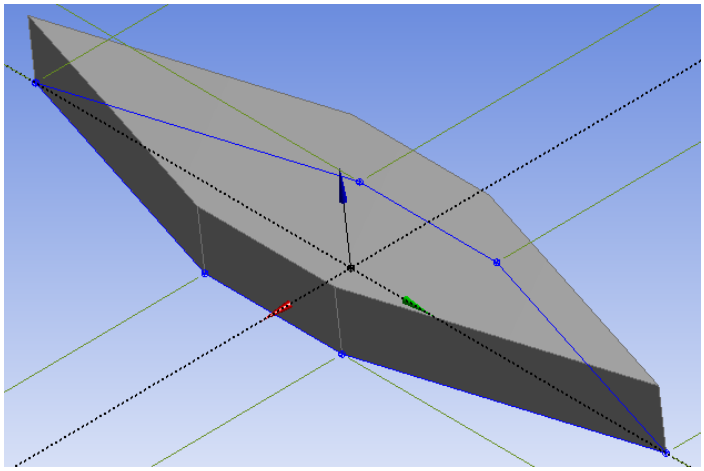

Figure 5.53 3D cell model.

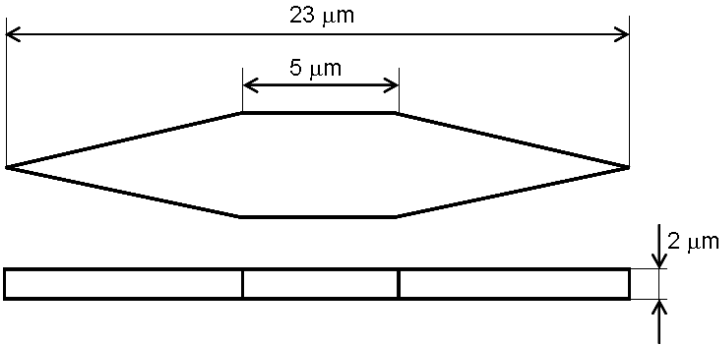

Figure 5.54 Cell dimensions.

To incorporate the cell into the model (see Figures 5.53 and 5.54), the cell's volume was subtracted from the original fluid model (section 5.4), leaving a well having the geometry of the cell (see Figures 5.55 and 5.56). The boundary condition applied to the fluid surfaces in contact with the cell is the same as that applied to the 'base' surface (see section 5.4.2.3) i.e. a no-slip boundary condition is applied.

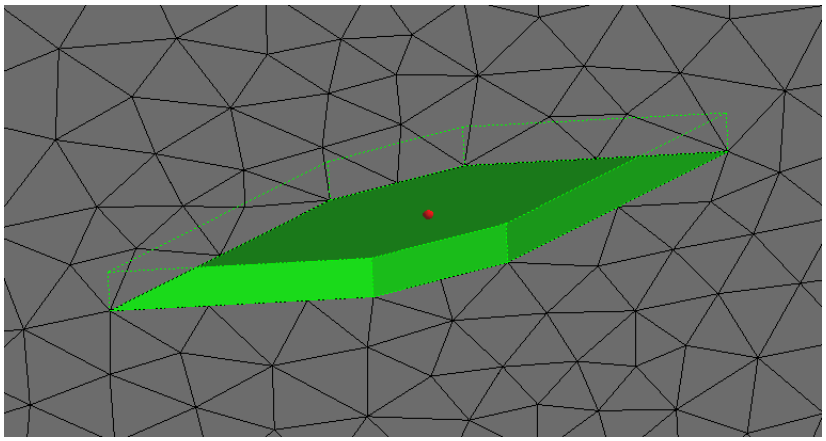

Figure 5.55 Well left after subtracting the cell volume from fluid used in section 5.4 .

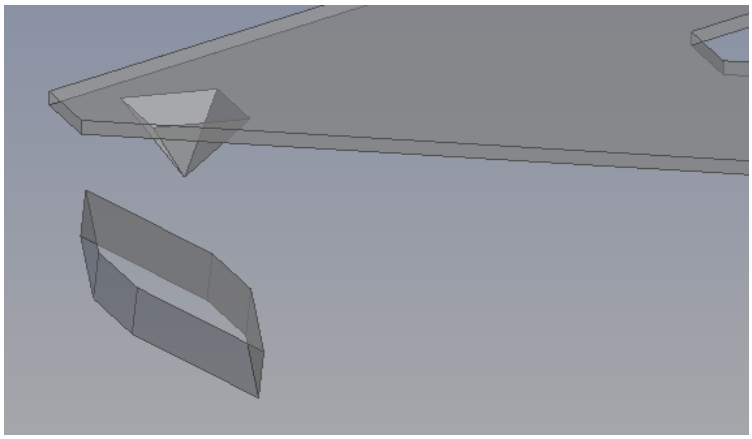

Figure 5.56 Cantilever tip and cell model.

Figure 5.57 shows the results of the investigation undertaken with and without the cell being included in the model. It can be seen upon inspection of this figure that the drag forces obtained in the model when the cell geometry was included are of bigger magnitude than the drag forces obtained in the model when the cell was not included; the difference in the results was being approximately 16.5%.

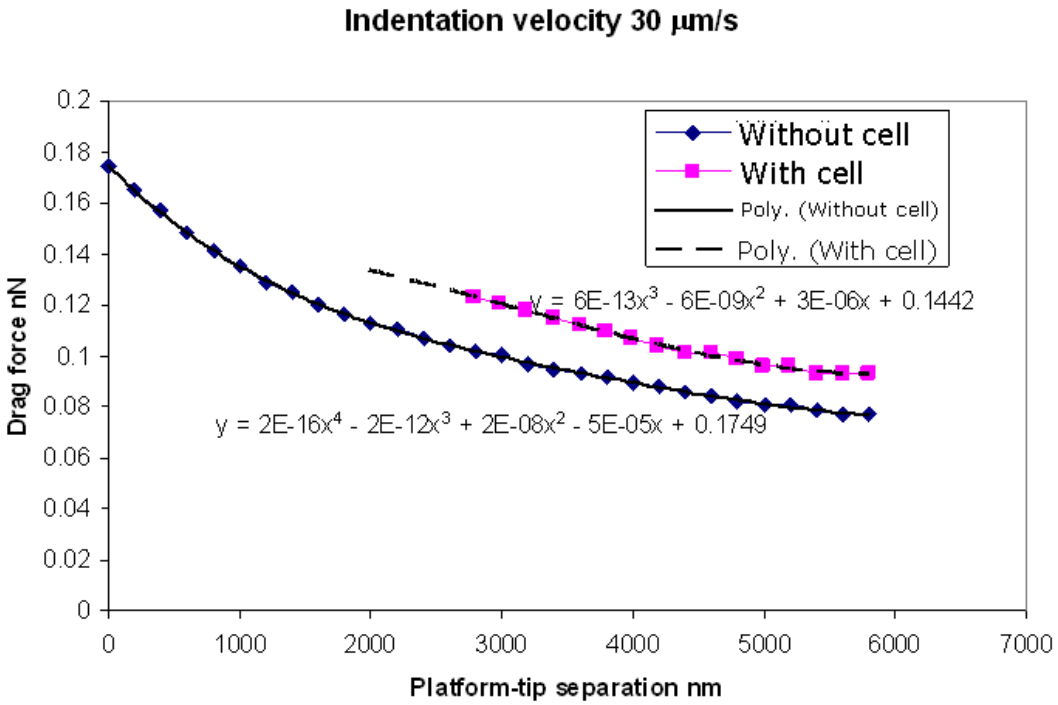

Figure 5.57 Drag force results of model with and without cell, water simulations.

Based in the investigation described in this Chapter it can be concluded that the finite element method is an extremely useful tool for predicting the drag force in AFM measurements in viscous fluid conditions. This technique has a number of advantages compared with empirical and analytical models, namely it is not necessary to determine empirical or geometrical factors before applying the model. In addition, the model can be easily modified for different cantilever geometries, materials and for different fluid media.

Chapter 6

Experimental work on cells.

6.1 Introduction.

In this chapter, the experimental methodology adopted to determine the apparent Young's modulus of adhered keloid and healthy cells is discussed. Indentations of single cells are performed to obtain a mechanical parameter that can be used to distinguish between normal and keloid cells. The Equipment and the experimental procedure used are described, and the results are discussed.

6.2 Materials.

AFM experiments in contact mode were carried out with an Picoforce Multimode AFM (Veeco, Cambridge, UK). Standard V-shaped silicon nitride probes from Veeco with a nominal spring constant of 0.06 N/m and tip radius of 10-40 nm were used. The nominal spring constants of the cantilevers used were calculated using the thermal tune method [159], which is built into the Picoforce Multimode AFM . It was found that the cantilevers used had values ranging from 0.032-0.0947 N/m. The cells were cultured on commercial glass slides with dimensions 5 x 5 mm and 0.5 mm thickness, from the same batch with a confluence of 50%, determined visually. Glass slides were cleaned by first being immersing in 100% methanol for 30 minutes and then washed with distilled water. The culture medium is described in section 6.3.

6.3 Cell preparation.

Primary human fibroblast cultures were obtained from fresh tissue punch biopsies (~6 mm). The samples were processed within 12-24 hours. The used tissues were washed thoroughly three times in 1 x phosphate buffered saline (PBS)(PAA, Germany) and incubated in freshly prepared DispaseII, 10mg/ml (Roche, UK), for 3 hours at 37 ºC. Epidermis and fat was carefully removed and dermis was minced and incubated in a solution of collagenase type I, 0.5 mg/mL (Roche, UK) and trypsin, 0.2 mg/mL (Roche, UK) at 37 ºC for 3 hours. Cells were pelleted and grown in the tissue culture flask. Fibroblasts were cultured in T25 CellBind flasks (Nunc, Life Technologies Ltd., Wiesbaden, Germany). Monolayer cultures were obtained in DMEM medium (PAA, Germany) supplemented with 2 mmol/L L-glutamine, 100 U/mL penicillin, and 100 U/mL streptomycin, 10% heat-inactivated fetal calf serum (FCS) (PPA, Germany), and 25 mmol/L N-2-Hydroxylpiperizine-N-O-2-ethanesulfonic acid (HEPES) (Cell Concepts, UK). Cells were incubated at 37 ºC in a 5% (v/v) CO_2 humidified atmosphere. The culturing media was replaced approximately every 48 hours, and cell passages were carried out at approximately 50% confluence using trypsin-ethylene diamine tetraacetic acid (200 mg L-ethylene diamine tetraacetic acid, 500 mg L-trypsin; Lonza). Full ethical approval and consent were obtained to conduct the study.

The cells used in experiments were frozen down in passage 5. This was carried out by re-suspension in freezing media (90% fetal bovine serum and 10 % dimethyl sulfoxide) following trypsin-ethylene diamine tetraacetic acid (EDTA) treatment, spinning at 1500-1800 rpm. The cells re-suspended in freezing media were placed at -80ºC. To reseed the cells, the frozen stock of cells was rapidly defrosted by placing in a 37ºC water bath. Following defrosting, the cell suspension was spun down using a centrifuge at 1500-1800 rpm. The cell pellet was resuspended in fibroblast culturing media and seeded onto the cut glass slide. Cells were seeded for about 4-6 days until approximately 50% confluence was obtained.

6.4 Cantilever Calibration.

6.4.1 Introduction.

In order to determine the indentation force Hooke's law ($F = \delta\ k$) was used, where F is indentation force, δ is the deflection of the cantilever determined by the AFM and k is the cantilever spring constant, a parameter that is determined using the thermal tune calibration method.

6.4.2 Thermal tune calibration.

The Thermal tune method was developed by Hutter and Bechhoefer [193]. The method is based on modelling the cantilever as a simple harmonic oscillator in equilibrium with its surroundings [193]. This system can be represented by the Hamiltonian equation:

$$H_a = \frac{p^2}{2m} + \frac{1}{2} m\omega_0^2 q^2 \tag{6.1}$$

where, H is the Hamiltonian equation, q is the displacement of the oscillator (cantilever), p is its momentum, m is the oscillating mass, and ω_0 is the resonant angular frequency of the system. By using the equipartition theorem [194] it is possible to relate the average value of each quadratic term in the Hamiltonian with $k_B T_{em} / 2$, where k_B is Boltzmann's constant and T_{em} is the temperature,

$$\left\langle \frac{1}{2} m\omega_0^2 q^2 \right\rangle = \frac{1}{2} k_B T_{em} \tag{6.2}$$

As $\omega_0^2 = k/m$ equation (6.2) becomes,

$$\left\langle \frac{1}{2} m\left(\frac{k}{m}\right) q^2 \right\rangle = \frac{1}{2} k_{\mathbf{B}} T_{em} \ ;\ \left\langle kq^2 \right\rangle = k_{\mathbf{B}} T_{em} \quad .$$

The above expression can be rearranged for k:

$$k = \frac{k_B T_{em}}{\left\langle q^2 \right\rangle} \tag{6.3}$$

Where, k_B is the Boltzmann constant, T_{em} is the temperature and $\langle q^2 \rangle$ is the mean square of the displacement of the cantilever.

In order to estimate the spring constant the AFM measures the cantilever's fluctuations in the time domain, after that the main square cantilever displacement is determined by integrating the area under a power spectral density curve.

6.4.3 Uncertainties in the calibration process.

Some of the main problems in k determination are the properties of the cantilever which can vary from batch to batch. For example in cantilevers commonly made of SiN_x the Young's modulus is in the range $\mathrm{E} \approx 130-385\ \mathrm{GPa}$, which leads to large uncertainties. Also, Poisson's ratio can range from $0.2-0.3$, with a less conservative estimate for Poisson's ratio being 0.25 ± 0.02, which includes most values as stated in the literature. Research has demonstrated that differences in the measured spring constant from cantilever to cantilever taken randomly from the same wafer can be as much as 2% [195].

6.5 Cell indentation.

In order to determine Young's modulus it is necessary to indent the samples. In the AFM it is possible to set up the desired cantilever deflection value, and relate this parameter using Hooke's law to determine the indentation depth. In these experiments the indentation depth has been varied in the range from 1200-2000 nm, using the microscope feedback to control the displacement of the scanner stopping it when the set value is reached.

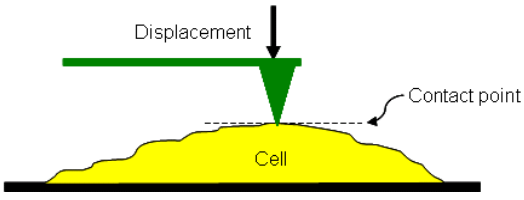

Figure 6.1 Cantilever-cell contact.

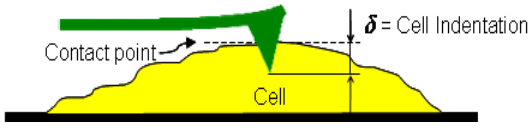

Figure 6.2 Cell indentation.

Figure 6.1 shows the first stage of cell indentation, when the cantilever tip is brought into contact with the cell. This contact is very important because

indentation starts at this point. As the displacement of the cantilever continues, the cantilever tip penetrates further into the cell shown in Figure 6.2. When the cantilever reaches the pre-set maximum deflection, then retraction begins.

6.6 Force curves.

The information obtained from an AFM experiment can be displayed in an x-y plot. For Young's modulus determination usually Force vs Indentation plots are used, however in this section also Force vs Z sensor (displacement of scanner) will be used because it is possible to obtain directly this information from the AFM raw data. Figure 6.3 shows a typical plot obtained from a hard material (for example glass) in an air fluid experiment. The dashed and the full lines are the approach and retraction curves respectively. As the cantilever is brought very close to the surface it remains almost undisturbed, but as the cantilever moves still closer a disturbance makes the cantilever jump, this is due to condensed water on the surface and also forces such as electrostatic, chemical and van der Waal's force are present. This jump is important because it facilitates the location of the cantilever-surface sample contact point, which can be clearly seen in the force curve in air fluid of the hard material (contact point is the vertex of the jump disturbance) shown in Figure 6.3. After the contact point the sample is indented by the cantilever tip; this indentation can be used to study the mechanical properties of the sample. After the force and indention reach their peak, the cantilever is moved in reverse. In an air-hard materials test, before the cantilever becomes unattached completely from the substrate it experiences a strong adhesive force.

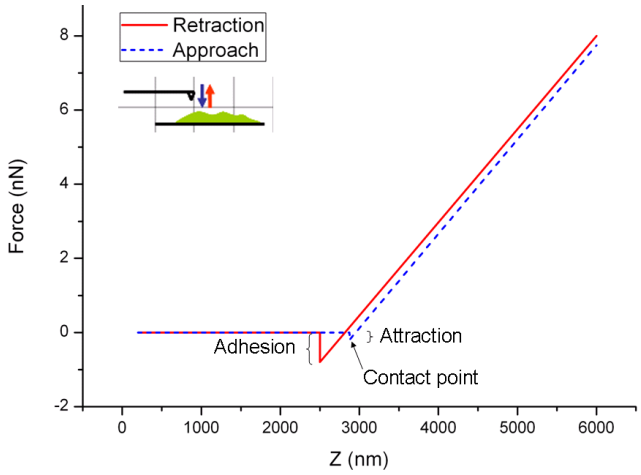

Figure 6.3 Force curve for a hard material.

In this thesis measurements were made on soft samples in fluids, therefore the force curves differ from those obtained in the case of hard materials. Figure 6.4. is an example of the force curve obtained for a soft sample (normal skin fibroblast) in PBS fluid on glass substrate. It can be seen that in this case there is not a clear contact point; this is mainly due to the fact that the fluid works as a damper, which makes it difficult to locate the contact point precisely.

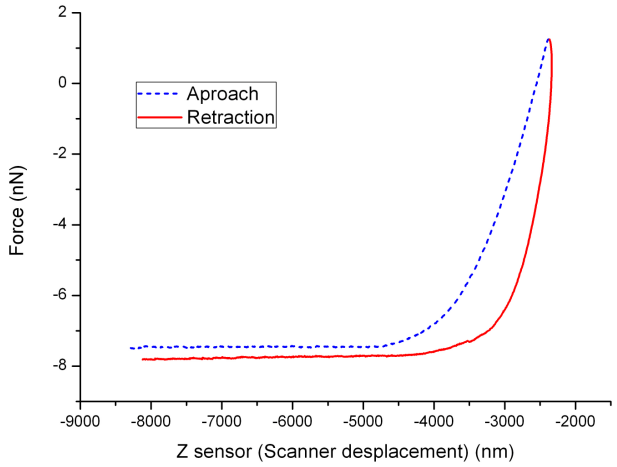

Figure 6.4 Example of a normal fibroblast cell 30 μm/s velocity completed cycle.

6.7 Contact point location.

The curve used for analysis in this work is the approach curve, selected due to fits reasonably well with Hertz's model (section 6.8) enabling the calculation of the apparent Young's modulus for the sample; therefore, from here onwards only the approach curves are considered.

The contact point location was obtained visually, by enlarging the force curves around the contact area. Figure 6.5 shows an enlarged contact point area of an approach curve shown in Figure 6.4. Inset (**a**) shows the contact region in yet more detail. In this case the contact point can be located relatively easily. In the vast majority of the cases considered in this thesis the results are similar to this case, with the contact point being located without significant problem.

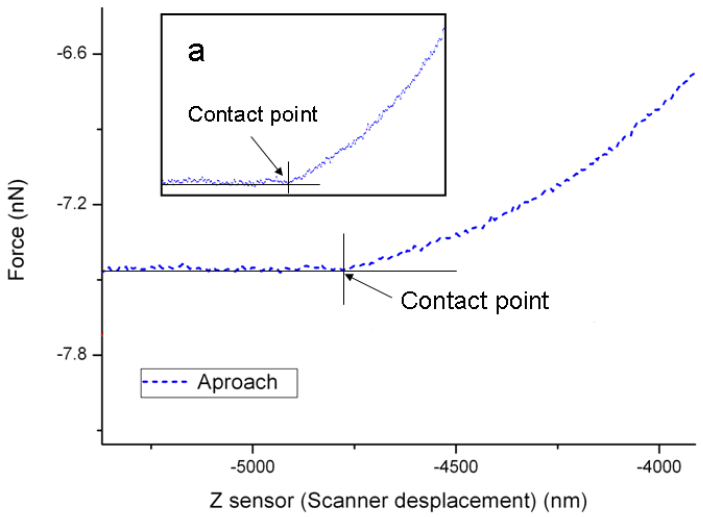

Figure 6.5 Zooming into the contact point.

Figure 6.6 shows 4 approach curves for velocities ranging 5 - 42 $\mu m/s$. In each of the curves the force is almost constant until the cantilever is close to the surface where a jump can be observed. A better view of the jump phenomenon can be seen in Figure 6.7 which shows the contact regions for the 4 curves in more detail. This increase in measured force may be attributed to surface forces (section 4.1.1). In some cases the jump behaviour proved useful in helping to determine the location of the contact point.

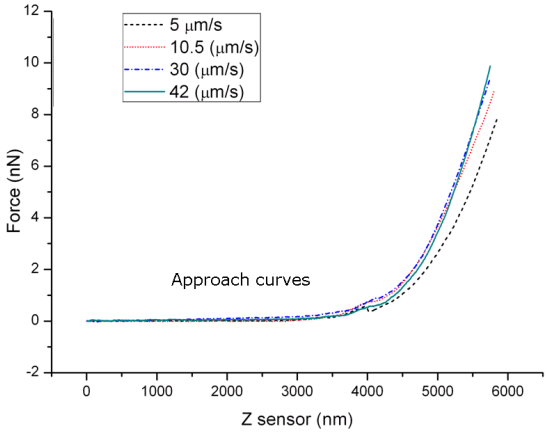

Figure 6.6 Approach force curves, 5, 10, 30, and 42 µm/s.

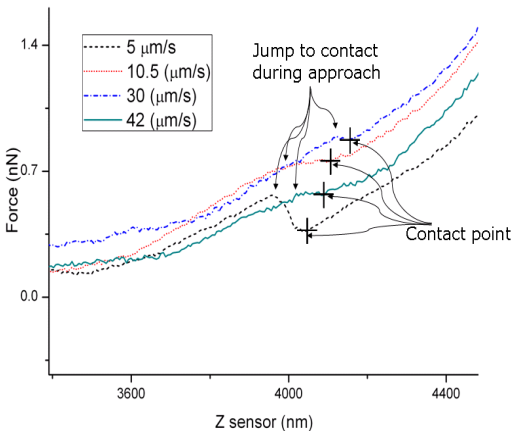

Figure 6.7 Contact point in more detail.

Another characteristic of the curves that can be used to facilitate the location of the contact point can be seen in the enlarged view of the contact region inset in Figure 6.8. In the contact region inset the location of the contact point is marked by a filled circle. The force signal was relatively noisy, oscillating with relatively

large amplitude prior to the contact point. However, this oscillation appears to stop abruptly at the contact point where the force rises but with almost no noise in the signal.

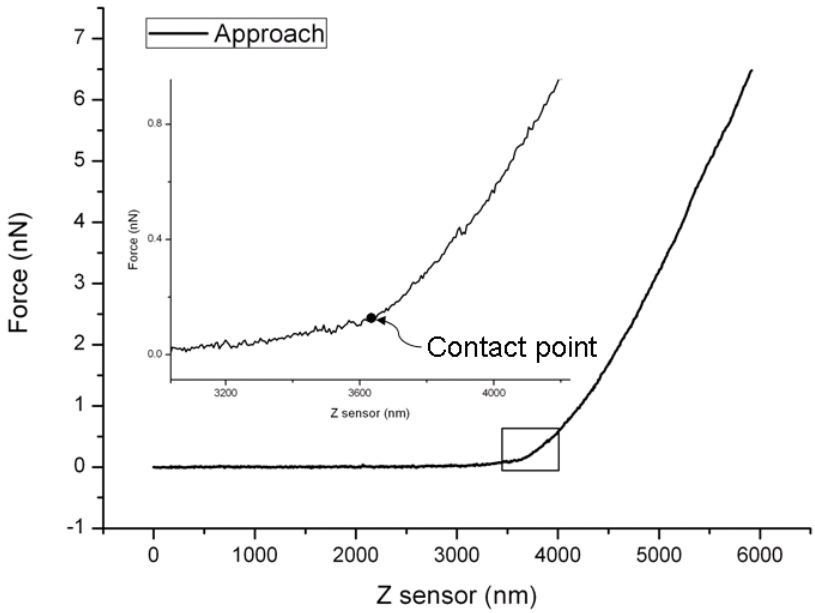

Figure 6.8 Contact point location.

The combination of these observations is used in the force curve analysis to accurately locate the contact point. It is important to accurately determine this point because the calculation of the apparent Young's modulus depends on the contact point selection. In most of the cases in these experiments the contact point was easily found. Note, the most difficult cases to find the contact points are those that involve low velocities because in these cases the force curves show perturbations close to the contact point, due to the surfaces forces (F_{sur}) (section 4.1.2.1), that make the contact point difficult to locate. In the relative high velocity cases ($>30\,\mu m/s$), the contact point can be found more easily. This is due to the fact that at these velocities drag forces tend to be higher than surface forces, $F_g > F_{sur}$, so the perturbations near to contact point don't disturb the force curve and the contact point is visually easy to locate.

6.8 Hertz's Model.

Hertz's model describes a solution for a normal contact problem between two elastic spheres. Hertz's theory predicts the stress distribution in the contact zone between two bodies having a surface of revolution. A very useful result of this theory is an equation that can be used to study the indentation for sphere to

sphere contact [196]. Hertz's model is based on several assumptions: the material of the contacting bodies is linearly elastic in nature, which means that the bodies behave according to Hooke's law, also the material is isotropic and homogeneous, the applied load is static, the strains are small, the contact surfaces are considered frictionless and each elastic body is considered as an elastic half-space. Hertz's model can be expressed in the following form:

$$F = \frac{4}{3} K R^{(1/2)} \delta^{(3/2)} \tag{6.4}$$

where, F is the normal force pressing the solids together, K, is the effective stiffness, R is the effective radius of curvature of the bodies and δ, is the total deformation of both surfaces.

The effective stiffness is defined using the expression for K:

$$\frac{1}{K} = \frac{1-\nu_1^2}{E_1} + \frac{1-\nu_2^2}{E_2} \tag{6.5}$$

Where E_1 and E_2 is the Young's modulus of body 1 and 2 respectively, ν_1 and ν_2 is the Poisson's ratio of body 1 and 2 respectively.

The effective radius of curvature R_E is defined as:

$$\frac{1}{R_E} = \frac{1}{R_1} + \frac{1}{R_2} \tag{6.6}$$

Hertz's model can be used to study the contact between a sphere and a flat body, for example in the case of cell indentation (Figure 6.9) the cell can be considered as a flat surface. Adopting this assumption, $R_1 = \infty$, hence the effective radius of curvature becomes $1/R_E = 1/R_2$. This assumption is valid especially when the indenter is very small compared with cell area. It can also be assumed that Young's modulus of the indenter, E_2, is much higher than that of the cell, E_1, therefore $1-\nu_2^2/E_2$ becomes negligible, and the effective stiffness becomes $1/K = (1-\nu_1^2)/E_1$. Note, in this case δ is the indentation of the cell.

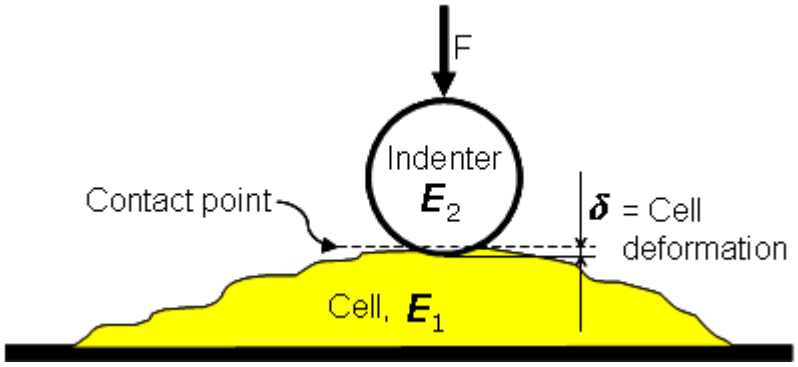

Figure 6.9 Indentation of a cell with a spherical indenter.

By rearranging expression (6.4) an expression for a spherical indenter can be obtained:

$$F = \frac{4}{3}\frac{E_1}{(1-\nu_1^2)} R_2^{\frac{1}{2}} \delta^{\frac{3}{2}} \tag{6.7}$$

Based on Hertz's model Bilodeau [197] determined the expression for a 4 sided pyramidal indenter [82]. This expression is as follows:

$$F = \frac{3}{4}\frac{E}{(1-\nu^2)} \tan\theta \ \delta^2 \tag{6.8}$$

Where F corresponds to the normal force applied, E is the apparent Young's modulus, θ is the cantilever tip half angle, ν is Poisson's ratio (assumed to be 0.5 [93]) and δ is the sample indentation.

Even when the cell is not homogenous and does behave as a linear elastic material, Hertz's model can describe its behaviour reasonably well, therefore Hertz's model was used to determine the apparent Young's modulus, E, from the experimental results.

The cantilever tip angle and cell Poisson's ratio (ν) are given in Table 6.1.

Variable	Symbol	Value
Tip front angle	θ	35 º
Poisson ratio cell [93, 198]	ν	0.5

Table 6.1 DNP-20 Veeco cantilever half angle and Poisson ratio of cell.

By substituting cantilever tip angle and cell Poisson's ratio, Equation (6.8) becomes:

$$F = 0.7002\, E\, \delta^2 \tag{6.9}$$

The apparent Young's modulus can then be determined by fitting equation (6.9) (exponential equation) to the force (F) versus indentation (δ) curve as shown in Figure 6.10.

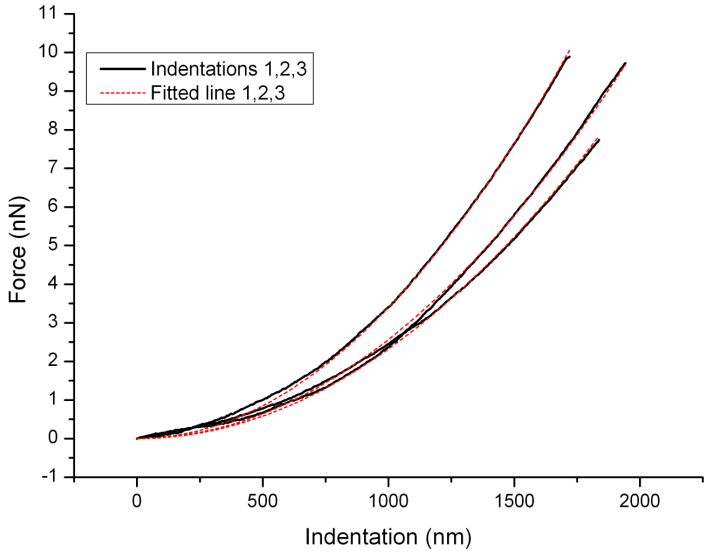

Figure 6.10 Hertz's model fitting in three force curve examples.

It is also possible to determine the apparent Young's modulus by rearranging Equation (6.8) and comparing to the equation of a straight line. Rearranging Equation (6.8) for E yields:

$$E = \frac{4F(1-\nu^2)}{3\tan\theta\,\delta^2} \tag{6.10}$$

Substituting the cantilever tip angle θ and cell Poisson's ratio ν from Table 6.1 then simplifying and comparing with the equation of a straight line gives:

$$E = \frac{1.428\,F}{\delta^2} = m = \frac{Y}{X} \tag{6.11}$$

where m is the slope of the line (see Figure 6.11).

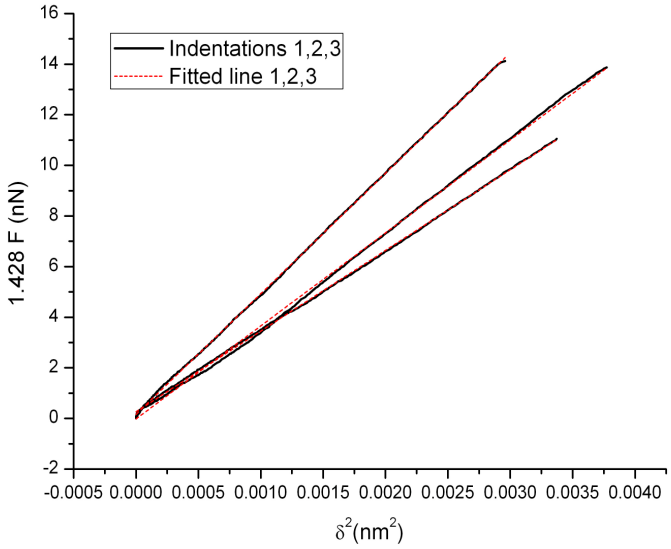

Figure 6.11 Determination of Young's modulus from the slope of the line (Equation 6.8)

Table 6.2 shows the Young's modulus results obtained from three indentation tests performed on normal fibroblast cells in PBS medium. Young's modulus values calculated using both the exponential fitting (Equation 6.9) and line fitting (Equation 6.11) techniques are given in this table. Upon inspection of Table 6.2 it can be seen that the differences in the Young's modulus values calculated using the line-fitting and exponential fitting techniques is relatively low; the largest difference 4%, occurred for the case of Indentation 1.

	E Pa ($F=0.7002E\delta^2$)	Line fitting ($E=Y/X$)	Error (%)
Indentation 1	3317	3188	4.0
Indentation 2	3667	3676	0.2
Indentation 3	4856	4767	1.86

Table 6.2 Comparison of Young's modulus values obtained by line-fitting vs. exponential fitting.

6.8.1 AFM measurements and organelles relationship.

Figure 6.12 shows 6 force curves obtained in measurements made on a single normal (healthy) cell, at different locations. The corresponding apparent Young's modulus value calculated using Hertz's model for each of the curves is given in the plot legend. These results are also plotted in Figure 6.13, where upon inspection, it can be seen that the calculated values vary enormously, with the difference between the lowest and the highest Young's modulus values being approximately 300 %. This large variation in calculated Young's modulus can be attributed to the cell's heterogeneity.

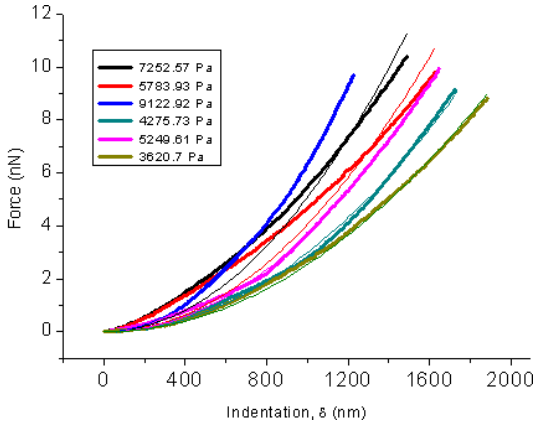

Figure 6.12 Indentations on a single cell.

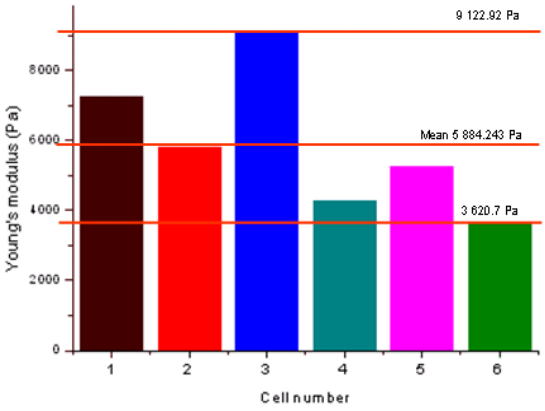

Figure 6.13 Young's modulus determined using Hertz's model.

The heterogeneity of the cell and the technical optical limitations in the AFM make it difficult to precisely locate the indenter over the cell, therefore the measurements obtained in the experiments can correspond to any cell location for example they may correspond to positions a), b), c) or d) in Figure 6.14. Even when the cantilever is located in the widest zone of the cell and it is assumed that the cantilever is located over the nucleus (position c) in Figure 6.14) due to it being the biggest cell organelle, this may in fact not be the case. Figure 6.14 shows a schematic diagram of a typical adhered cell tested in the experiments. The shape of the adhered cell facilitates a more precise location of the indenter in relation to the cell, in contrast to highly spread cells which are hard to locate under the AFM camera (Figure 6.18).

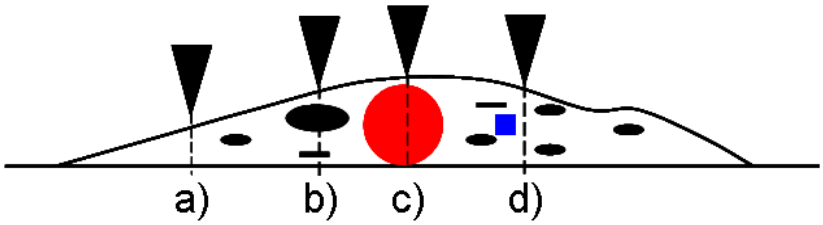

Figure 6.14 Graphic representation of the cell heterogeneity.

The precise location of the indentation site on the cell is difficult to determine, for the previously discussed reasons, therefore different values for Young's modulus can be determined depending of the cantilever tip location on the cell and the location of the internal components of the cell at the particular indentation point. To explain these differences in Young's modulus 4 different cases for cell indentation will be considered, as shown in Figure 6.15.

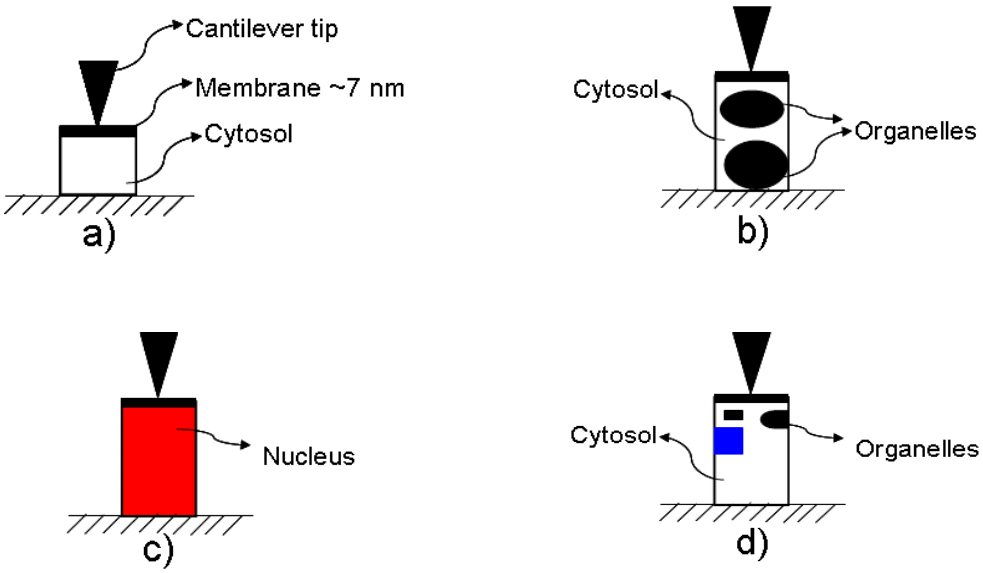

Figure 6.15 Four indentation cases.

In Case a) the indentation is performed on the membrane and cytosol. It is expected that the lowest Young's modulus will be obtained in this situation as the cytosol consists mainly of water [199]. Figure 6.16 shows the corresponding force curve (line fitting) for this case.

In Case b) the cantilever tip is located over one or more organelles. Initially the membrane and possibly the cytosol are indented. Subsequently the tip reaches an organelle that is pushed down and partially indented. Figure 6.17 shows a characteristic force curve (line fitted) for this case. Three distinct sections are clearly visible in this plot. The first section corresponds to the period when the tip initially indents the soft cell zone (membrane and cytosol). Following further indentation, a second distinct section can be observed which corresponds to the tip contacting a harder cell zone (organelle or rearranged cytoskeleton). The final section illustrates the case when the tip reaches an even harder cell zone, corresponding to further indentation of an organelle(s). This is easily observed when, as shown in Figure 6.17, the AFM data are plotted to fit Equation (6.8) (Figure 6.11) where the slope represent the apparent Young's modulus as discussed in 6.8.

In Case c) the cantilever tip is located over the nucleus of the cell resulting in first the membrane then the nucleus is being indented. Figure 6.16 shows the corresponding force curve (line fitting) for this case. Figure 6.18 shows a normal fibroblast cell adhered to the substrate. The cell, labelled 'Tested Cell' in Figure 6.18 is similar to the cells used in the experimental work described in this thesis.

It can be seen that the central part of this cell, containing the nucleus, is relatively wide. These types of cells are clearly visible under the AFM microscope, and it is therefore relatively easy to locate the cantilever tip in this area which makes it more likely that the indentation in the experimental tests was carried out on the nucleus, the most rigid organelle in the cell [77].

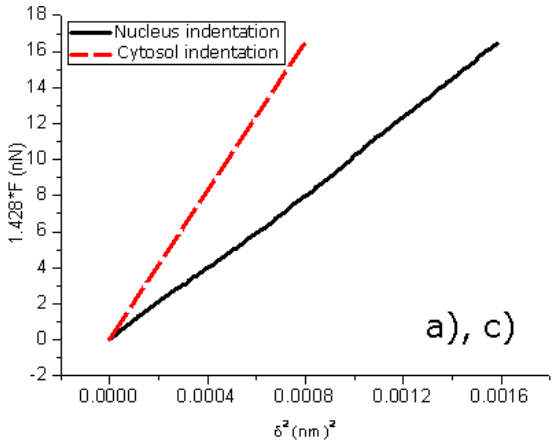

Figure 6.16 Case a) indentation of soft cell part, c) indentation of hard cell part.

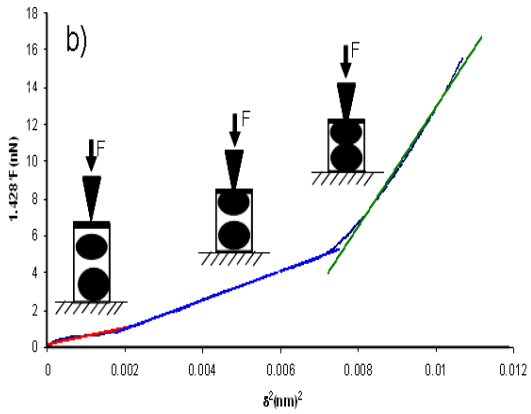

Figure 6.17 Case b) multiple Young's modulus.

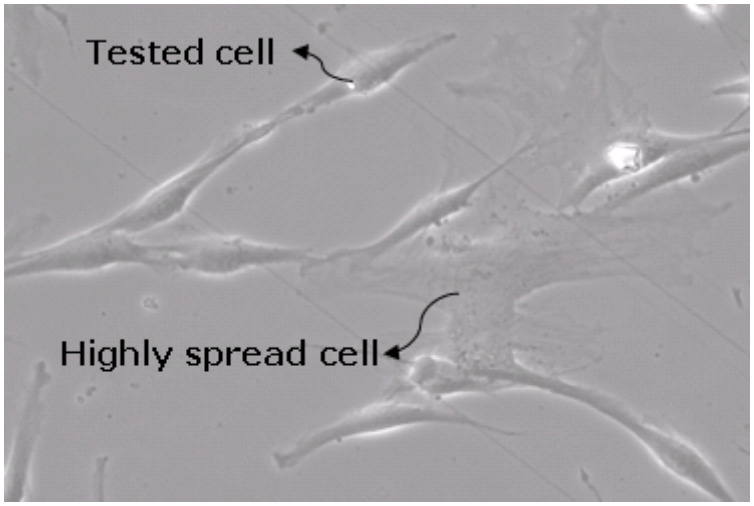

Figure 6.18 Normal skin fibroblast cells adhered to glass.

Case d) illustrates the fourth scenario (see Figure 6.19), where forces curve with disturbances is shown. This phenomenon could be due to tip interactions with nearby organelles together with cytoskeleton rearrangement. Despite these disturbances, Hertz's model can be used to describe the relationship $F-\delta$ in most of the cases with acceptable accuracy.

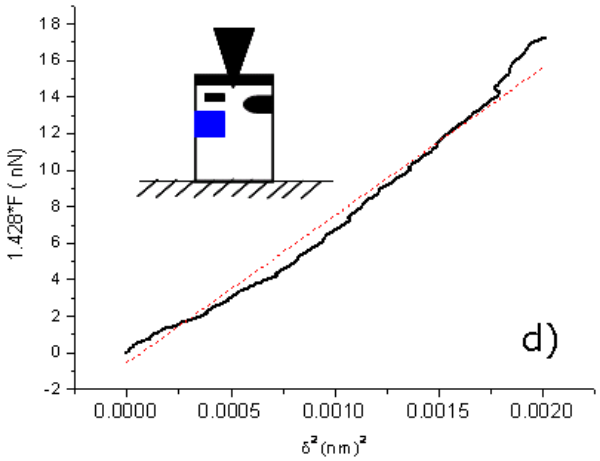

Figure 6.19 Case d) Perturbations in the indentation.

The force curves used in this thesis are examples of cases a), c) and d), in which it was found that Hertz's model could be used.

6.9 Experimental Tests.

The experimental tests were divided into two parts:

1) Comparison of normal and keloid cells, passage 6 from 5 patients.

2) Comparison of normal and keloid cells passage 2, 3, 4, and 6 from a single patient.

In both experiments normal and keloid cells were indented with 4 velocities: 5, 10.5, 30 and 42 μm/s. The selection of velocities was undertaken with the objective of determining the Young's modulus of the cells and considering dynamic cell response. The technical limitations of the AFM had also to be taken into account in the velocity selection as the velocities available with the AFM depend on the specified ramp size (6 μm) selected and the number of captured data points per cycle (1028 points in this case). Therefore, four velocities were selected to cover the range of velocities available. The lowest velocity of 5 μm/s was expected to capture the static response of the cells. The velocities of 10.5, 30 and 42 μm/s were expected to produce a component of dynamic cell response to the applied load. Each of the cells tested was indented in a single location using the aforementioned velocities. The cells were cultured on 3-4 pieces of cut glass slide for a period of 4-6 days until the cell confluence was approximately 50%.

The glass slide for each patient was taken out of the incubator at the moment of testing. Each glass slide was picked up from the Petri dish and washed with PBS warmed up to 37ºC to remove the unattached cells, then the Petri dish base was dried and put on a metallic disk designed to attach magnetically to the AFM scanner. Once the glass slide was in position, approximately 30 μml of PBS was dropped onto the glass slide. With the glass slide and AFM head and chip holder in place, single cells were located and indented in their widest section, see Figure 6.18.

The number of cells tested in the case of experimental work part **1** was:

A total of 14 normal cells and 14 keloid cells for each patient were selected. In this experiment each cell was indented 7 times for each velocity, therefore the total indentation per patient for each velocity was 14x7=98.

The number of cells tested in the case of experimental work part **2** was:

In the case of passages 2, 3, and 4 a total of 14 normal and 14 keloid cells were tested, and the number of indentations per velocity was 3. The total indentation per velocity in each passage was therefore 14x3=42. For passage 6, 50 normal and 50 keloid cells were indented, so the total number of indentations per velocity in this case was 50x3=150.

6.10 Young's modulus of keloid cells, passage 6 from 5 patients.

The objective of this experiment was to examine the results obtained from different patients and based on these results to plan and undertake a second and more detailed set of experiments using samples from a single patient.

In order to be able to compare the Young's modulus the results of normal and keloid cells were plotted as shown in Figure 6.20. This figure shows the results corresponding to 14 keloid cells obtained in experiment 2, passage 2. For visual clarity the information is organised from lowest to highest Young's modulus average (the average result for the 7 indentations performed at each velocity are displayed in Figure 6.20) for the 4 velocities tested for each cell. The wide variation of Young's modulus values that can be seen in Figure 6.20 may be due to the factors discussed in section 6.8.1. The horizontal solid red line in Figure

6.20 is the mean Young's modulus which has a value of 7361 Pa; the highest and the lowest values are also indicated in the plot, being 22715.5 Pa and 1974 Pa respectively. Between the highest and lowest values, Young's modulus values are divided into 4 zones. The boundary between zones 1 and 2 is halfway between the mean and the maximum Young's modulus value. The boundary between zones 3 and 4 is halfway between the mean and the lowest Young's modulus value. Section 6.8.1 explained how the variation of Young's modulus may be due to the heterogeneity of the cell. The cases that each zone in the plot may represent are shown on the right hand side of Figure 6.20; these cases are a) cytosol indentation, d) indentation affected by nearby organelles and cytoskeleton rearrangement and c) nucleus indentation.

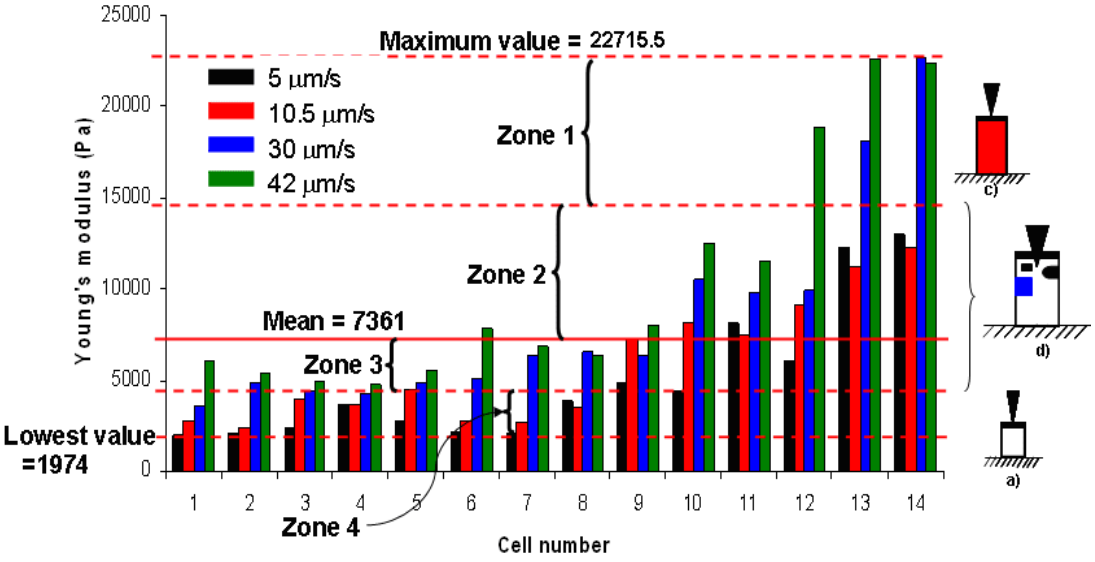

Figure 6.20 Experiment 2, passage 2, keloid cells.

6.10.1 Comparison of normal and keloid cells, passage 6 from 5 patients.

In this experiment normal and keloid skin fibroblasts cells, passage 6 from 5 different patients were tested. The cells were cultured according to the process described in section 6.3. The results obtained for the 5 patients are shown in Figure 6.21, 6.23, 6.25, 6.27 and 6.29, where each column represents the average Young's modulus obtained at each velocity (the average result for the 7 indentations performed at each velocity are displayed for every cell). The results for keloid and normal cells are shown in the same plot for each patient.

6.10.1.1 Patient 1.

The results for Patient 1 shown in Figure 6.21 clearly indicate a difference between the apparent Young's modulus of keloid and normal cells, with keloid cells having higher Young's modulus values than normal cells. In addition, it can be seen from Figure 6.21 that Young's modulus values vary according to the indentation velocity, generally increasing with velocity. This effect can be attributed to cytoskeleton reorganisation. Similar observations were seen in all the patients.

The mean apparent Young's modulus for the keloid cells is 27124 Pa and for normal cells it is 8807 Pa. The mean values were calculated taking into account the 4 velocities. These results indicate that keloid cells are 207% stiffer than normal cells.

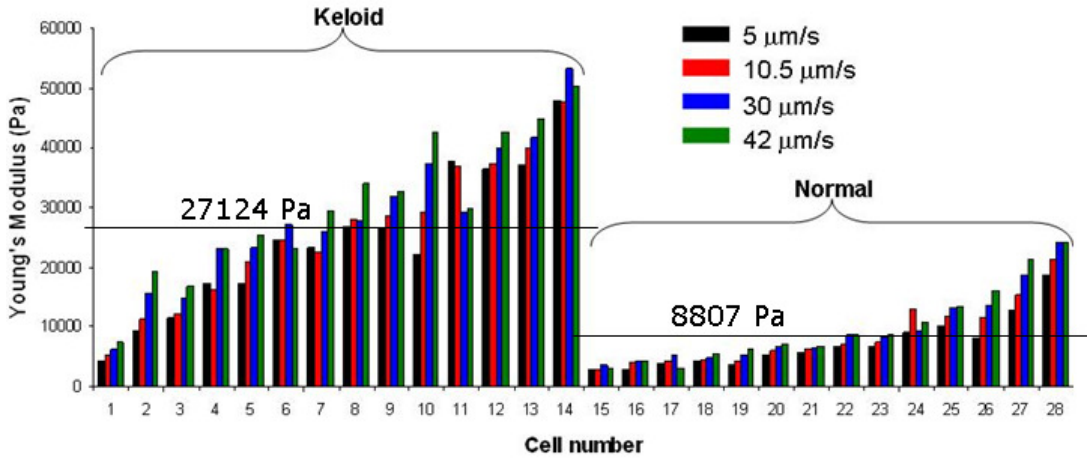

Figure 6.21 Indentation velocities 5, 10.5, 30 and 42 μm/s. Patient 1.

In Figure 6.22, 6.24, 6.26, 6.28 and 6.30 the average Young's modulus obtained for normal and keloid cells at each of the velocities tested is shown, the bars correspond to the standard deviation values, also it is important to mention that for convenience in these figures there is no significance to the cell numbers or order of each indentation experiment. Tables 6.3, 6.5, 6.7, 6.9 and 6.11 contain the respectively values used in the plots for the 5 patients.

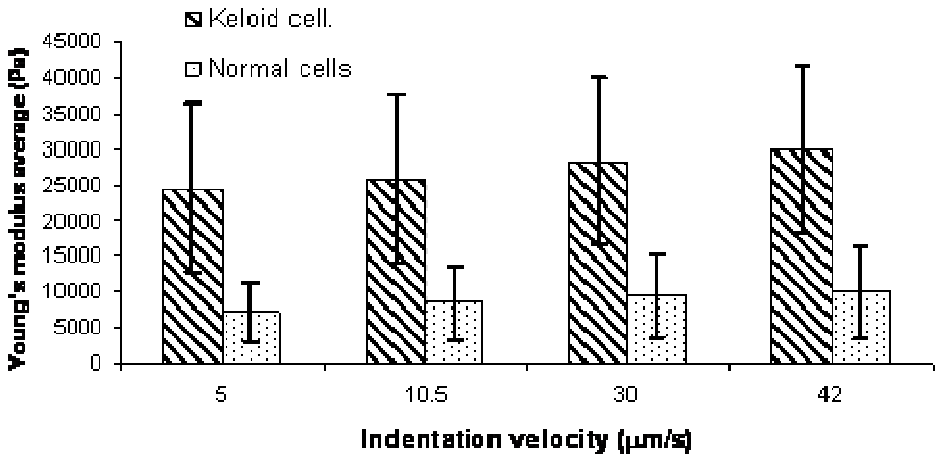

Figure 6.22 Young's modulus average vs Indentation velocity. Patient 1

Patient 1	Keloid cells.		Normal cells.	
Indentation velocity (μm/s)	E average (Pa)	S D	E average (Pa)	S D
5	24494.1	11819.7	7212.9	4232.5
10.5	25839.7	11676.5	8559.3	5168.3
30	28373.0	11712.4	9502.4	5798.9
42	30093.1	11635.0	9956.9	6318.7

Table 6.3 Young's modulus average and standard deviation. Patient 1

Upon inspection of Figure 6.22 it can be seen that even though the standard deviation is high in the Young's modulus values obtained for both keloid and normal cells, at each velocity there is no overlap between the values obtained for the two types of cells which suggests that the results obtained are significantly different. However, in order to verify that there are significant differences between both kinds of cells a t-test is applied.

6.10.1.2 T-test

In order to investigate if there is a significance difference between the Young's modulus values calculated for keloid and normal cells a significance test was performed. If it is assumed that the distribution of the results is normal then a t-test [200] can be applied. Equation (6.12) applies for a population in which the standard deviations are different.

$$t_t = \frac{(\bar{x}_1 - \bar{x}_2)}{\sqrt{\frac{s_1^2}{n_1} + \frac{s_2^2}{n_2}}} \tag{6.12}$$

Where $\overline{x}$, is the arithmetic mean of the sample, s, is the standard deviation of the sample, n, is the sample size, index 1 denotes the keloid cells and index 2 the normal cells. In such cases the degrees of freedom (DF) are determined using Equation (6.13).

$$\text{Degrees of freedom (DF)} = \frac{\left(\frac{s_1^2}{n_1} + \frac{s_2^2}{n_2}\right)^2}{\frac{s_1^4}{n_1^2(n_1 - 1)} + \frac{s_2^4}{n_2^2(n_2 - 1)}} \tag{6.13}$$

The degrees of freedom are used to obtain the critical value t_c using widely available tables [200] using a significance of 0.05 (95%) which means that there is 95% of probability that the confidence interval contains the true mean value, it is important to say that equation 6.13 is used because the variances of each sample set are different.

The t-test will be used to probe a null hypothesis, for this case the hypothesis is that the Young's modulus value for keloid and normal cells is the same. This hypothesis is evaluated by comparing t_t against t_c, with the two possible results being:

- $t_t > t_c$, the hypothesis is rejected; this means that there is enough evidence to say that the mean concentration of the Young's modulus values differs between keloid and normal cells.

- $t_t < t_c$, the hypothesis is accepted; this means that there is no evidence to say that the mean concentration of the Young's modulus values differs between keloid and normal cells.

Table 6.4 shows the t_t and t_c values calculated using the Young's modulus data obtained for patient 1. Upon inspection of Table 6.4 it can be see that $t_t > t_c$ for all the velocities tested. It can be concluded, therefore, that there is enough evidence to say that the mean concentration of the Young's modulus values differs between keloid and normal cells.

Patient 1									
Velocity μm/s	$\bar{x}_1$	$\bar{x}_2$	s1	s2	n1	n2	DF	t_t	t_c
5	24494.1	7212.9	11819.7	4232.5	98	98	121.4	13.63	2.01
10.5	25839.7	8559.3	11676.5	5168.3	98	98	133.6	13.40	2.01
30	28373.0	9502.4	11712.4	5798.9	98	98	141.8	14.29	2.01
42	30093.1	9956.9	11635.0	6318.7	98	98	149.6	15.06	2.01

Table 6.4 Significance difference between keloid and normal cell. Patient 1

6.10.1.3 Patient 2.

The results obtained for patient 2 are shown in Figures 6.23 and 6.24 and Table 6.5. From Figure 6.24 it can be observed that for patient 2 the differences between the average Young's modulus values calculated for normal and keloid cells are less marked than for patient 1, in this case the mean average Young's modulus for the keloid cells is 21858 Pa and for the normal cells it is 14673 Pa. Comparing the mean values calculated shows that keloid cells stiffness is 48% higher than normal cells.

In this case the use of a t-test is very useful in establishing if there is a significant statistical difference between the Young's modulus values for the two types of cells.

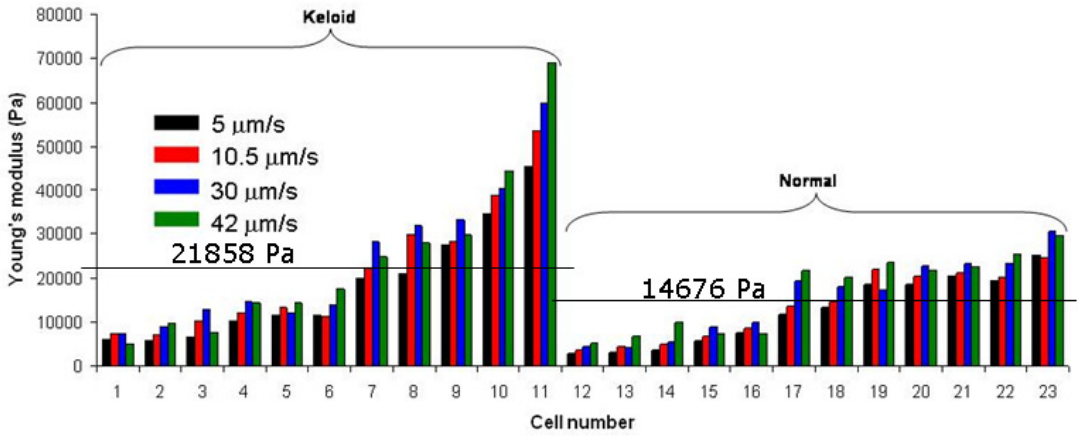

Figure 6.23 Indentation velocities 5, 10.5, 30 and 42 μm/s. Patient 2.

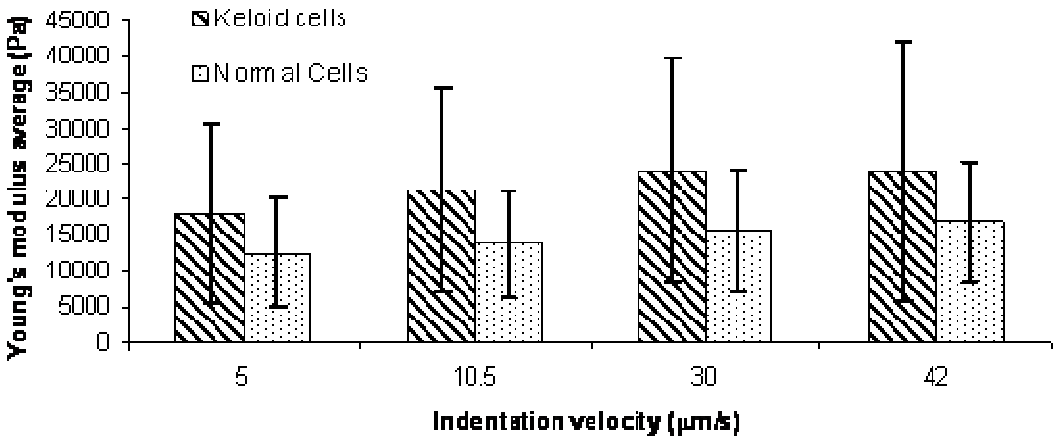

Figure 6.24 Young's modulus average vs Indentation velocity. Patient 2

Patient 2	Keloid cells		Normal cells.	
Indentation velocity (μm/s)	Average Pa	S D	Average Pa	S D
5	18167.9	12398.7	12510.7	7480.4
10.5	21282.9	14285.1	13784.3	7419.5
30	23926.9	15650.3	15647.5	8423.0
42	24057.9	17995.2	16751.9	8339.8

Table 6.5 Young's modulus average and standard deviation. Patient 2

Comparing the calculated t_t and t_c values for patient 2 given in Table 6.6 it can be seen that $t_t > t_c$ for all the velocities, indicating that, as for patient 1, the mean concentration of Young's modulus values differs between keloid and normal cells.

Patient 2									
Velocity μm/s	$\overline{x}_1$	$\overline{x}_2$	s1	s2	n1	n2	DF	t_t	t_c
5	18167.9	12510.7	12398.7	7480.4	77	84	122.6	3.47	2.01
10.5	21282.9	13784.3	14285.1	7419.5	77	84	111.9	4.12	2.01
30	23926.9	15647.5	15650.3	8423.0	77	84	114.3	4.13	2.01
42	24057.9	16751.9	17995.2	8339.8	77	84	105.1	3.26	2.01

Table 6.6 Significance difference between keloid and normal cell. Patient 2

6.10.1.4 Patient 3.

The results obtained for patient 3 are shown in Figures 6.25 and 6.26 and Table 6.7. Upon inspection of these results it can be seen that the Young's modulus average for keloid cells is 36043 Pa and for normal cells it is 11219 Pa, which means that keloid cells show a higher Young's modulus, in fact keloid cell stiffness is 221% higher than normal cells.

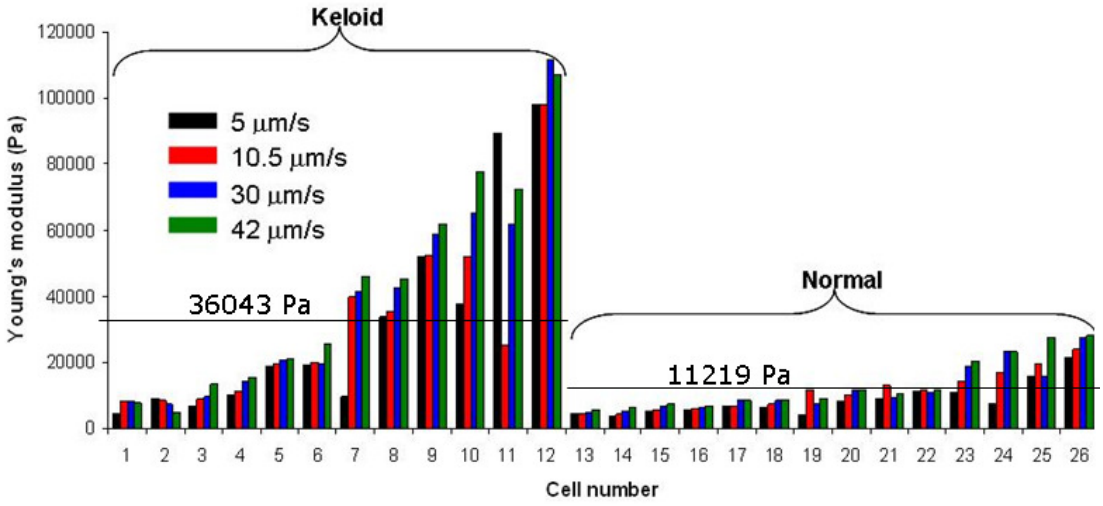

Figure 6.25 Indentation velocities 5, 10.5, 30 and 42 μm/s. Patient 3.

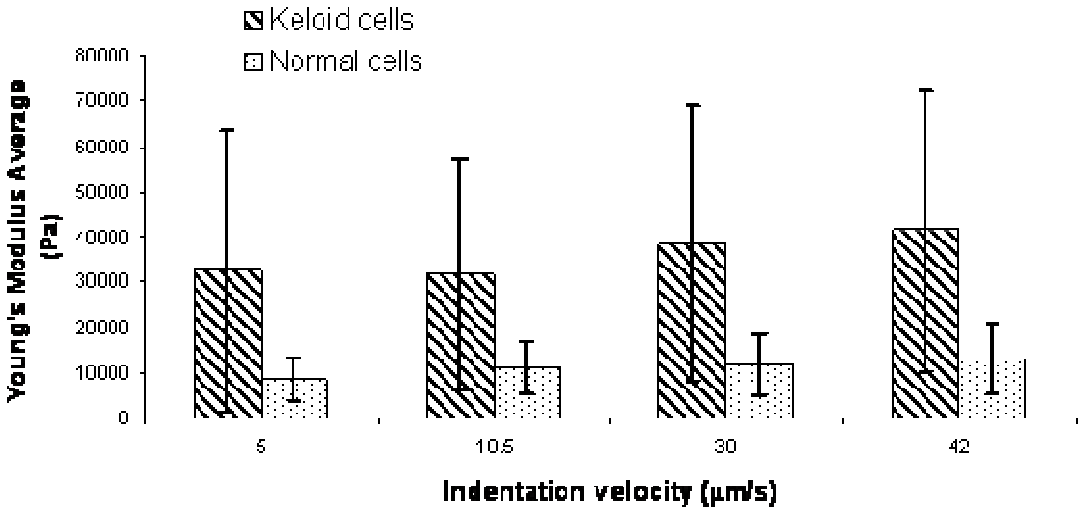

Figure 6.26 Young's modulus average vs Indentation velocity. Patient 3

Patient 3	Keloid cells		Normal cells	
Indentation velocity (μm/s)	Average (Pa)	S D	Average (Pa)	S D
5	32503.4	30771.4	8641.3	4826.5
10.5	31645.9	25322.1	11217.2	5705.8
30	38484.1	30286.0	11793.3	6739.8
42	41541.1	31067.9	13225.7	7732.8

Table 6.7 Young's modulus average and standard deviation. Patient 3

Comparing the calculated t_t and t_c values for patient 3 given in Tables 6.8 it can be seen that $t > t_c$ for all the velocities, indicating that the difference between the Young's modulus values calculated for the normal and keloid cells is statistically significant.

Patient 3									
Velocity μm/s	$\overline{x}_1$	$\overline{x}_2$	s1	s2	n1	n2	DF	t_t	t_c
5	32503.4	8641.3	30771.4	4826.5	84	98	86.5	7.03	2.01
10.5	31645.9	11217.2	25322.1	5705.8	84	98	90.2	7.24	2.01
30	38484.1	11793.3	30286.0	6739.8	84	98	90.0	7.91	2.01
42	41541.1	13225.7	31067.9	7732.8	84	98	91.8	8.14	2.01

Table 6.8 Significance difference between keloid and normal cell. Patient 3

6.10.1.5 Patient 4.

The results obtained for patient 4 are shown in Figures 6.27 and 6.28 and Table 6.9. In this case the apparent Young's modulus for keloid cells is 14668 Pa and for normal cells it is 7234 Pa. Keloid cells are 102% stiffer than normal cells, this difference is less marked compared with patient 3 where the difference was 221%.

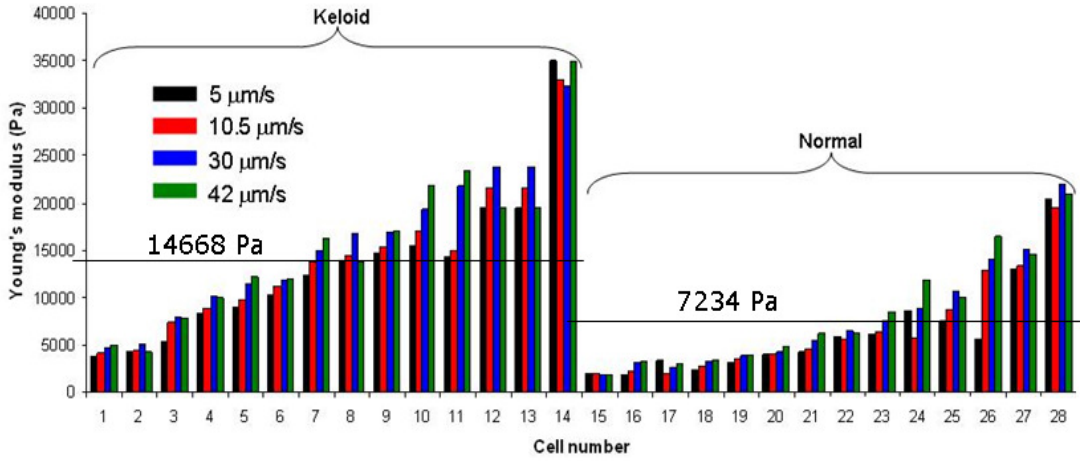

Figure 6.27 Indentation velocities 5, 10.5, 30 and 42 μm/s. Patient 4

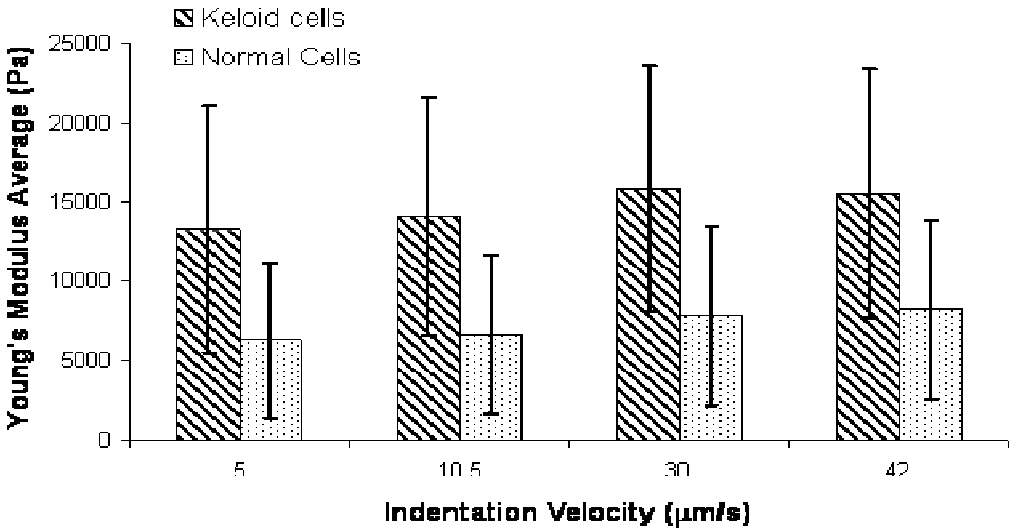

Figure 6.28 Young's modulus average vs Indentation velocity. Patient 4

Patient 4	Keloid cells		Normal cells.	
Indentation velocity (μm/s)	Average (Pa)	D S	Average (Pa)	S D
5	13250.9	7760.4	6286.3	4869.8
10.5	14098.8	7438.0	6643.9	4999.9
30	15814.6	7665.9	7798.7	5607.6
42	15510.0	7844.2	8210.6	5607.9

Table 6.9 Young's modulus average and standard deviation. Patient 4

The t_t and t_c values calculated for patient 4 are given in Tables 6.10. The values calculated for these parameters again indicate that the difference

between the normal and keloid cell Young's modulus values is statistically significant.

Patient 4									
Velocity μm/s	$\bar{x}_1$	$\bar{x}_2$	s1	s2	n1	n2	DF	t_t	t_c
5	13250.9	6286.3	7760.4	6286.3	98	98	185.9	6.90	2.01
10.5	14098.8	6643.9	7438.0	6643.9	98	98	191.5	7.40	2.01
30	15814.6	7798.7	7665.9	7798.7	98	98	193.9	7.26	2.01
42	15510.0	8210.6	7844.2	8210.6	98	98	193.6	6.36	2.01

Table 6.10 Significance difference between keloid and normal cell. Patient 4

6.10.1.6 Patient 5.

The results obtained for patient 5 are shown in Figures 6.29 and 6.30 and Table 6.11. From Figure 6.29 it can be observed that there are differences between keloid and normal cells, with keloid cells exhibiting a 104% greater stiffness compared with normal cells. The apparent Young's modulus average is 19834 Pa for the keloid cells and 9709 Pa for the normal cells.

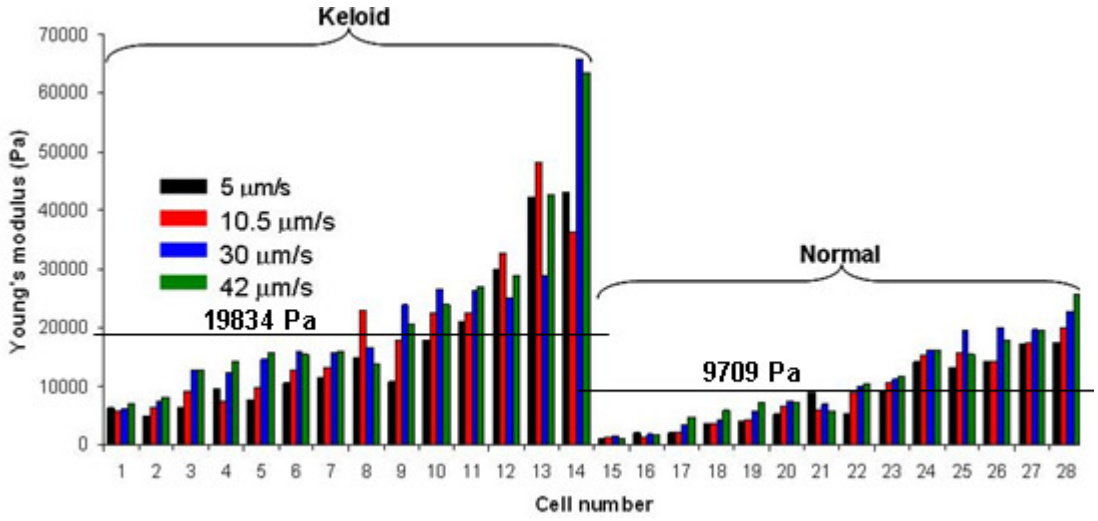

Figure 6.29 Indentation velocities 5, 10.5, 30 and 42 μm/s. Patient 5.

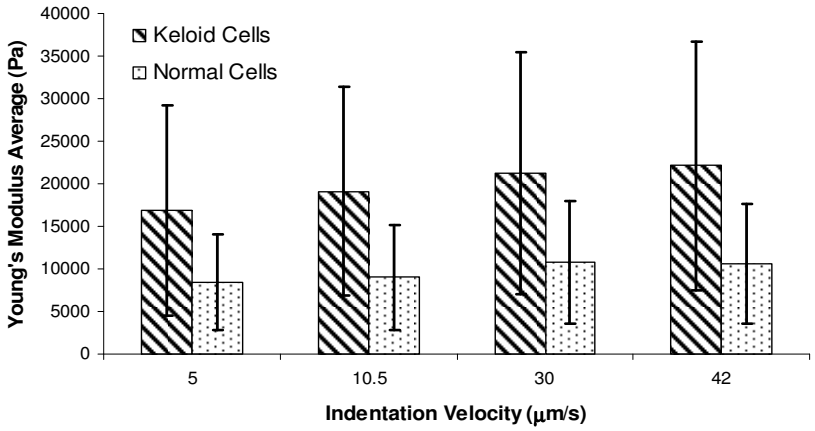

Figure 6.30 Young's modulus average vs Indentation velocity. Patient 5

Patient 5	Keloid cells		Normal cells	
Indentation velocity (μm/s)	Average, E (Pa)	S D	Average, E (Pa)	S D
5	16885.3	12374.5	8407.5	5647.6
10.5	19065.4	12266.6	9037.2	6182.0
30	21278.8	14190.6	10709.8	7188.2
42	22109.6	14567.1	10685.0	7027.8

Table 6.11 Young's modulus average and standard deviation. Patient 5

The results of the t-test analysis shown in Table 6.12 are in agreement with the results obtained for patients 1, 2, 3 and 4, demonstrating that statistically, there is a significant difference between the normal and keloid cell Young's modulus values.

Patient 5									
Velocity μm/s	$\overline{x}_1$	$\overline{x}_2$	s1	s2	n1	n2	DF	t_t	t_c
5	16885.3	8407.5	12374.5	5647.6	98	98	135.7	6.17	2.01
10.5	19065.4	9037.2	12266.6	6182.0	98	98	143.2	7.23	2.01
30	21278.8	10709.8	14190.6	7188.2	98	98	143.7	6.58	2.01
42	22109.6	10685.0	14567.1	7027.8	98	98	139.8	6.99	2.01

Table 6.12 Significance difference between keloid and normal cell. Patient 5

The apparent Young's modulus average values determined for the 5 patients considered are summarised in Figures 6.31 for keloid and 6.32 normal cells, where upon inspection it can be seen that the Young's modulus average (the average was obtained considering the 4 velocity results for each patient) is 23921 Pa. For normal cells, Figure 6.32, the average is 10329 Pa. Overall, the keloid cells were on average 131% stiffer than normal cells.

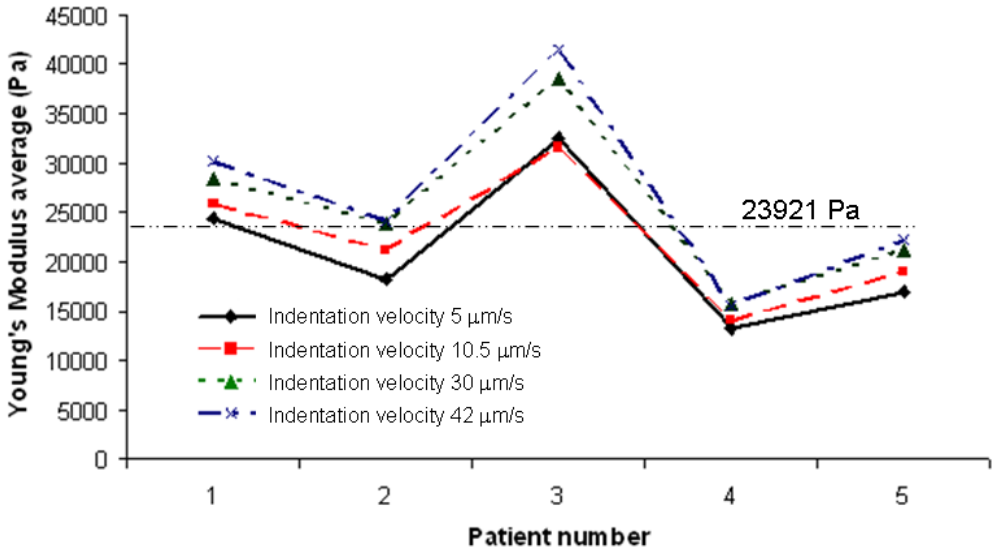

Figure 6.31 Young's modulus average of the 5 patients, corresponding to keloid cells.

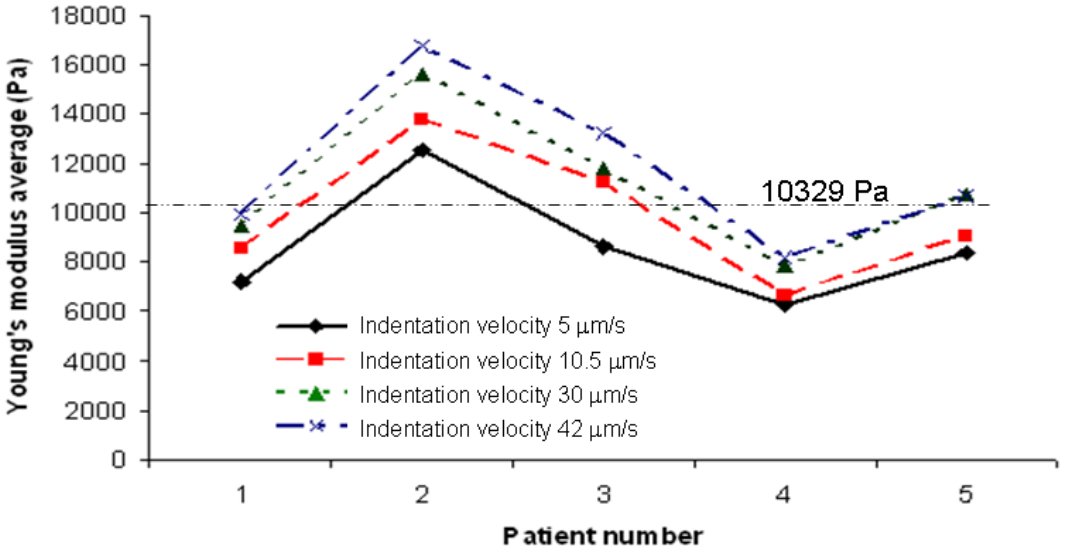

Figure 6.32 Young's modulus average of the 5 patients, corresponding to normal cells.

Differences between keloid and normal cell Young's modulus values were found for all the patients tested. These differences were measured using AFM in all the patients. Keloid cells were found to be stiffer than normal cells. Based on these results, a further set of tests was planned and undertaken to measure the apparent Young's modulus values for keloid and normal cells considering early passages, as Wozniak et al. [201] discovered that the stiffness of the cells tends to be higher in early passages. These tests are detailed in the next section.

6.11 Comparison of normal and keloid cells passage 2, 3, 4, and 6 from a single patient.

In this experiment normal and keloid skin fibroblast cells for passages 2, 3, 4 and 6 from a single patient were tested. Passages 2, 3, and 4, were cultured according to the process described previously in section 6.3. For passage 6 the cultured process was modified, In passage 5 the fetal calf serum was reduced to 5% in order to reduce the growth rate then these cell were sat on a glass slide at passage 6 to be indented in the AFM.

The results obtained are shown in Figure 6.33, 6.35, 6.37, 6.39 and 6.40, where the results for both normal and keloid cells are displayed in order to facilitate a comparison of the results.

6.11.1 Passage 2.

The results obtained for passage 2 are shown in Figures 6.33 and 6.34 and Table 6.13. The Young's modulus average for the keloid cells is 7361 Pa and for normal the cells it is 4511 Pa, indicating that keloid cells are 63% stiffer than normal cells. In both cases the Young's modulus values found are not concentrated around the mean with values varying considerably from cell to cell. For example in the case of the keloid cells for a velocity of 5 μm/s the Young's modulus varies between 2500 Pa and 12500 Pa, a difference of about 500%.

In a similar manner to the previous experiments, t-test calculations were performed to establish if the difference between the normal and keloid cell results are statistically significant.

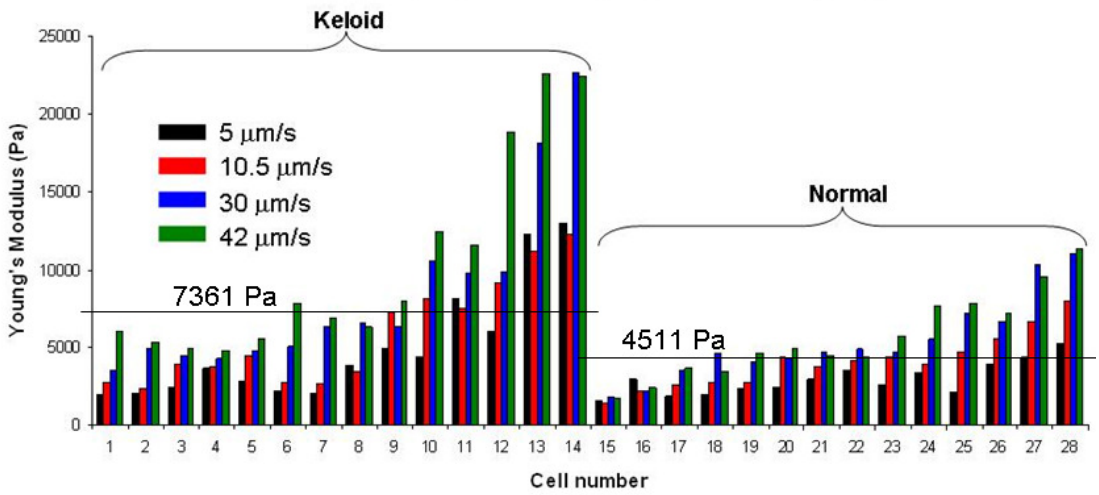

Figure 6.33 Indentation velocities 5, 10.5, 30 and 42 μm/s. Passage 2.

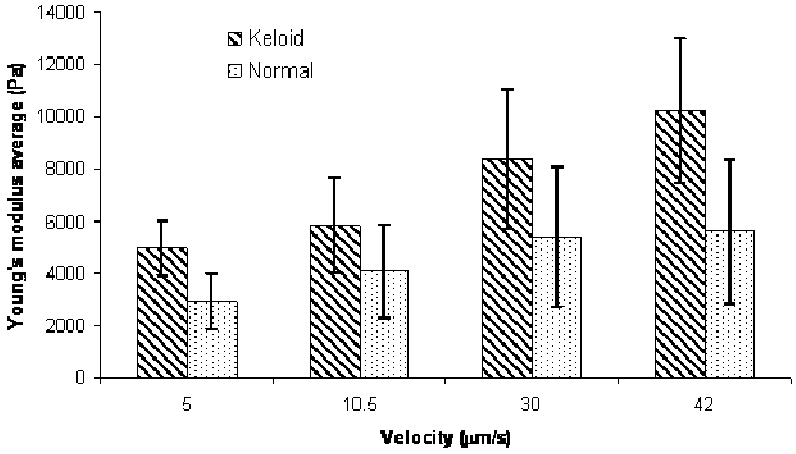

Figure 6.34 Young's modulus average vs Indentation velocity. Passage 2

Passage 2	Keloid Cells		Normal Cells	
Indentation velocity (μm/s)	Average, E (Pa)	S D	Average, E (Pa)	S D
5	4979.8	3688.0	2934.6	1043.1
10.5	5837.7	3371.8	4086.0	1787.8
30	8383.4	5631.7	5407.4	2652.0
42	10246.8	6453.0	5620.2	2748.4

Table 6.13 Young's modulus average and standard deviation. Passage 2

Table 6.14 shows the corresponding t-test results for this case (passage 2). The values calculated for t_t and t_c confirm previous results, indicating that there is a statistically significant difference between the Young's modulus values calculated for the keloid and normal cells.

Passage 2									
Velocity μm/s	$\bar{x}_1$	$\bar{x}_2$	s1	s2	n1	n2	DF	t_t	t_c
5	4979.8	2934.6	3688.0	1043.1	42	42	47.5	3.46	2.01
10.5	5837.7	4086.0	3371.8	1787.8	42	42	62.3	2.97	2.01
30	8383.4	5407.4	5631.7	2652.0	42	42	58.3	3.10	2.01
42	10246.8	5620.2	6453.0	2748.4	42	42	55.4	4.27	2.01

Table 6.14 Significance difference between keloid and normal cell. Passage 2

6.11.2 Passage 3.

The results obtained for passage 3 are shown in Figures 6.35 and 6.36 and Table 6.15. The results show that in the case of normal cells the standard deviation is relatively small which means that the majority of the results are concentrated around the mean, which has a value of 5108 Pa. In contrast, the keloid cell results show that the Young's modulus values are spread widely around the mean, which has a value of 9719 Pa. These results show that keloid cells are stiffer than normal cells.

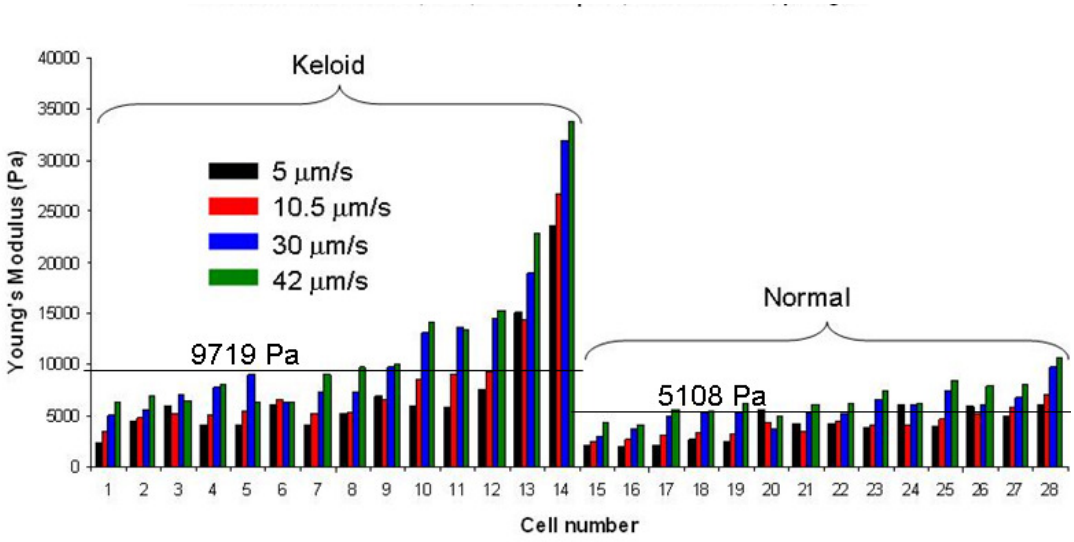

Figure 6.35 Indentation velocities 5, 10.5, 30 and 42 μm/s. Passage 3.

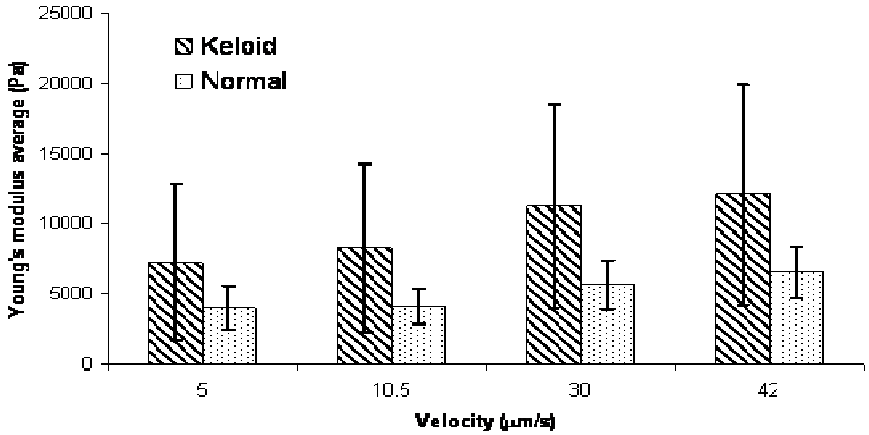

Figure 6.36 Young's modulus average vs Indentation velocity. Passage 3

Passage 3	Keloid Cells		Patient KS 107, Normal Cells	
Indentation velocity (μm/s)	Average, E (Pa)	S D	Average, E (Pa)	S D
5	7257.9	5551.3	4033.5	1543.7
10.5	8292.0	5964.0	4162.3	1250.3
30	11258	7181.0	5673.7	1725.5
42	12069.7	7825.0	6564.8	1810.9

Table 6.15 Young's modulus average and standard deviation. Passage 3

Table 6.16 shows the corresponding t-test results for the case of passage 3. The t-test results indicate that there is a statistically significant difference between the Young's modulus values calculated for the keloid and normal cells.

Passage 3									
Velocity μm/s	$\overline{x}_1$	$\overline{x}_2$	s1	s2	n1	n2	DF	t_t	t_c
5	7257.9	4033.5	5551.3	1543.7	42	42	47.3	3.63	2.01
10.5	8292.0	4162.3	5964.0	1250.3	42	42	44.6	4.39	2.01
30	11258	5673.7	7181.0	1725.5	42	42	45.7	4.90	2.01
42	12069.7	6564.8	7825.0	1810.9	42	42	45.3	4.44	2.01

Table 6.16 Significance difference between keloid and normal cell. Passage 3

6.11.3 Passage 4.

The results obtained for passage 4 are shown in Figures 6.37 and 6.38 and Table 6.17. If cell 28 is not considered then the standard deviation is small, similar to the normal cell results for passage 3, with Young's modulus values concentrated around the mean, which has a value of 5000 Pa. The mean Young's modulus value for the keloid cells is 11137 Pa. Comparing the Young's modulus mean values shows that keloid cells are 122% stiffer than normal cells.

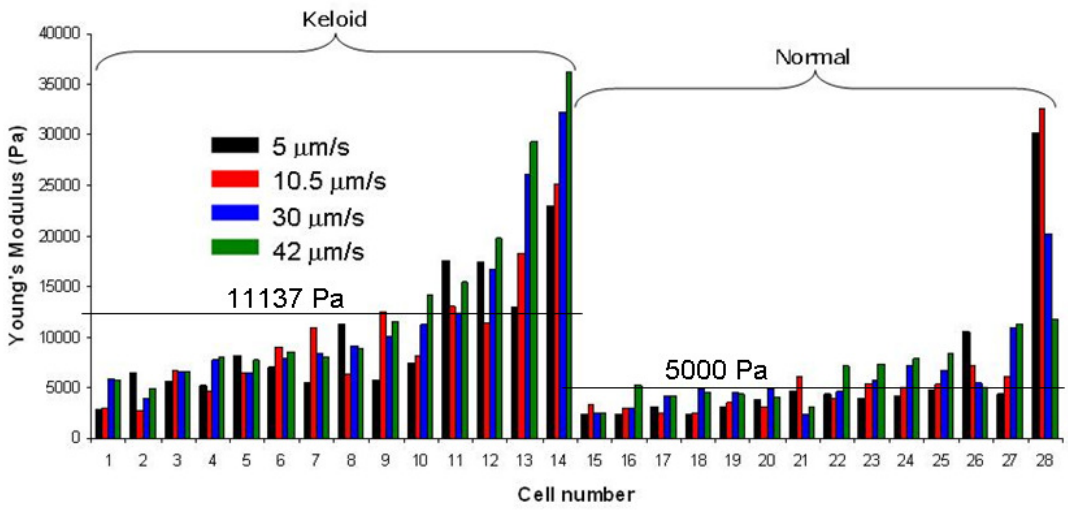

Figure 6.37 Indentation velocities 5, 10.5, 30 and 42 µm/s. Passage 4.

In Figure 6.38 can be observed that the standard deviation bar for 5 and 10.5 µm/s is very wide, this effect is also due to cell 28 which if removed with a statistical test like the q test might be similar to passage 3.

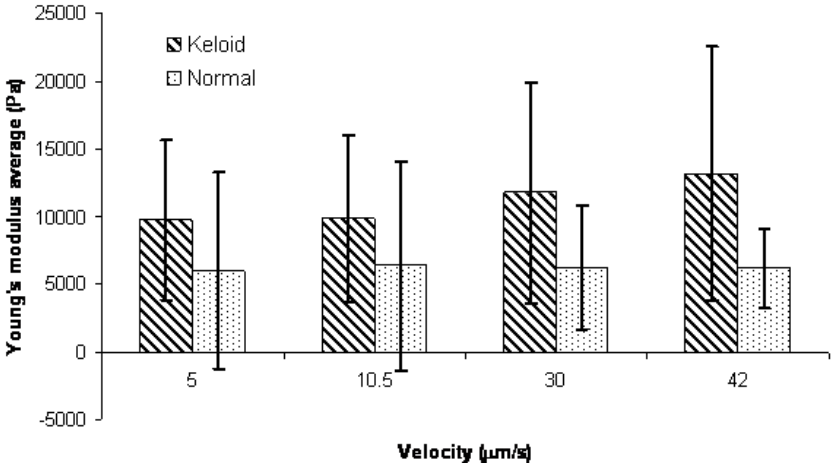

Figure 6.38 Young's modulus average vs Indentation velocity. Passage 4

Passage 4	Keloid Cells		Normal Cells	
Indentation velocity (µm/s)	Average, E (Pa)	S D	Average, E (Pa)	S D
5	9718.4	5902.9	5996.3	7235.5
10.5	9879.1	6140.7	6375.9	7695.0
30	11752.9	8124.9	6232.2	4561.7
42	13200.5	9341.0	6180.8	2868.2

Table 6.17 Young's modulus average and standard deviation. Passage 4

Table 6.18 shows the t-test results for passage 4. The t-test results indicate that there is a statistically significant difference between the Young's modulus values for the keloid and normal cells.

Passage 4									
Velocity μm/s	$\bar{x}_1$	$\bar{x}_2$	s1	s2	n1	n2	DF	t_t	t_c
5	9718.4	5996.3	5902.9	7235.5	42	42	78.8	2.58	2.01
10.5	9879.1	6375.9	6140.7	7695.0	42	42	78.1	2.31	2.01
30	11752.9	6232.2	8124.9	4561.7	42	42	64.5	3.84	2.01
42	13200.5	6180.8	9341.0	2868.2	42	42	48.6	4.66	2.01

Table 6.18 Significance difference between keloid and normal cell. Passage 4

6.11.4 Passage 6.

In passage 6 the number of cells tested was increased. Figures 6.39, 6.40 and 6.41 and Table 6.19 show the results obtained for this case. The increased number of cells tested makes a visual comparison between the calculated Young's modulus values for the normal cells (Figure 6.39) and keloid cells (Figure 6.40) more difficult. The Young's modulus average for keloid cells is 8319 Pa and for normal cell it is 6537 Pa. Keloid cells are therefore 22% stiffer than normal cells; this percentage is low compared with passages 3 and 4, and may due to the change in the cell culture process. However the t-test results shown in Table 6.20 indicate that effectively there are significant differences between the normal and keloid cell Young's modulus values in this passage.

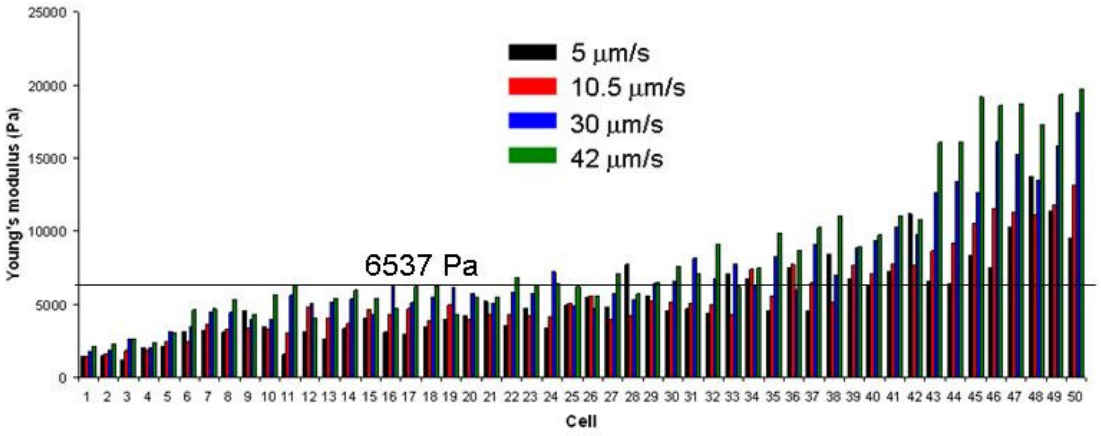

Figure 6.39 Indentation velocities 5, 10.5, 30 and 42 μm/s. Passage 6, normal.

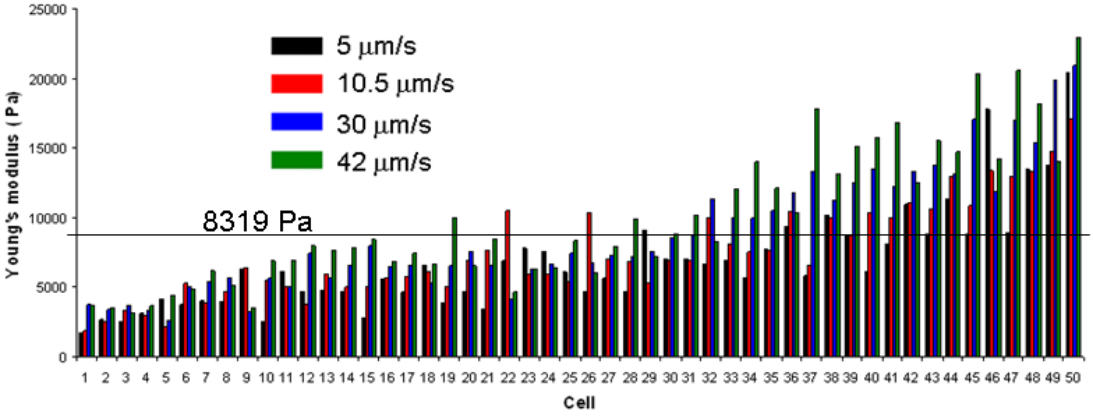

Figure 6.40 Indentation velocities 5, 10.5, 30 and 42 μm/s. Passage 6, keloid.

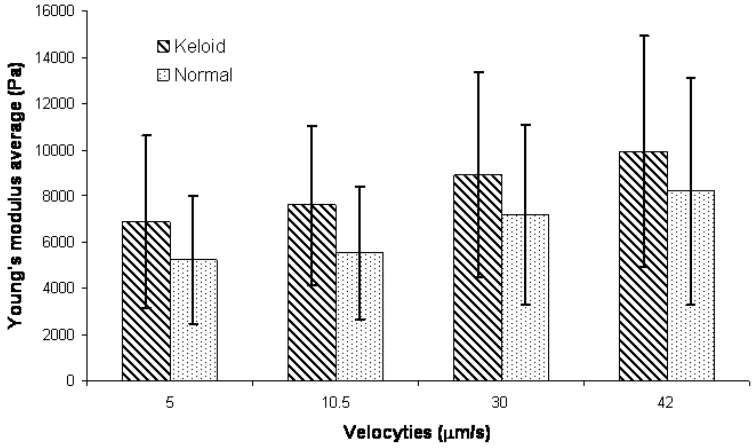

Figure 6.41 Young's modulus average vs Indentation velocity. Passage 6

Passage 6	Keloid Cells		Normal Cells	
Velocity μm/s	Average	SD	Average	SD
5	6885.5	3716.0	5233.5	2779.2
10.5	7584.3	3443.9	5541.3	2866.9
30	8896.3	4415.7	7174.1	3885.2
42	9912.4	4993.5	8200.6	4910.2

Table 6.19 Young's modulus average and standard deviation. Passage 6

Analysing the results of the t-test analysis shown in Table 6.20, it can be concluded that there is a statistically significant difference between the Young's modulus values for the keloid and normal cells, therefore it can be said that keloid and normal cells are different.

Passage 6									
Velocity μm/s	$\bar{x}_1$	$\bar{x}_2$	s1	s2	n1	n2	DF	t_t	t_c
5	6885.5	5233.5	3716.0	2779.2	150	150	275.9	4.36	1.96
10.5	7584.3	5541.3	3443.9	2866.9	150	150	288.5	5.58	1.96
30	8896.3	7174.1	4415.7	3885.2	150	150	293.2	3.59	1.96
42	9912.4	8200.6	4993.5	4910.2	150	150	297.9	2.99	1.96

Table 6.20 Significance difference between keloid and normal cell. Passage 6

The Young's modulus averages for the keloid cells for each velocity of passage 2, 3, 4 and 6 corresponding to the results shown Tables 6.13, 6.15, 6.17 and 6.19, are plotted in Figure 6.42. In this plot the stiffness of the cells can be seen to increase with passage, up to passage 4, with the same phenomenon occurring for all the velocities. However in passage 6 the Young's modulus decreases, which may be attributed to the change in the cell culture procedure that was undertaken in passage 6.

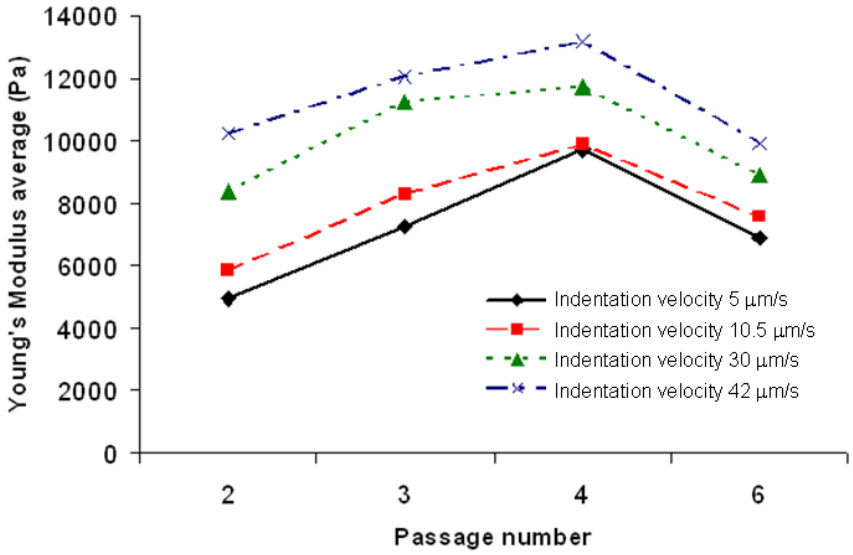

Figure 6.42 Young's modulus of keloid cells, corresponding to passage 2, 3, 4 and 6.

The Young's modulus averages for the normal cells for each velocity of passage 2, 3, 4 and 6 corresponding to the results shown Tables 6.13, 6.15, 6.17 and 6.19, are plotted in Figure 6.43. In this case it can be seen that the cell stiffness in passages 2, 3 and 4 increases in a similar manner to the keloid cells results, however in passage 6 the Young's modulus continues to increase for velocities of 30 and 42 μm/s whereas for velocities of 5 and 10.5 mm/s it reduces. This change in the trend may be due to the change in the cell culture procedure, which consisted of decreasing the fetal calf serum from 10 to 5% or

alternatively, the change could be a normal cell stiffness change which would indicate that cell stiffness reduces in the late cell culture passage.

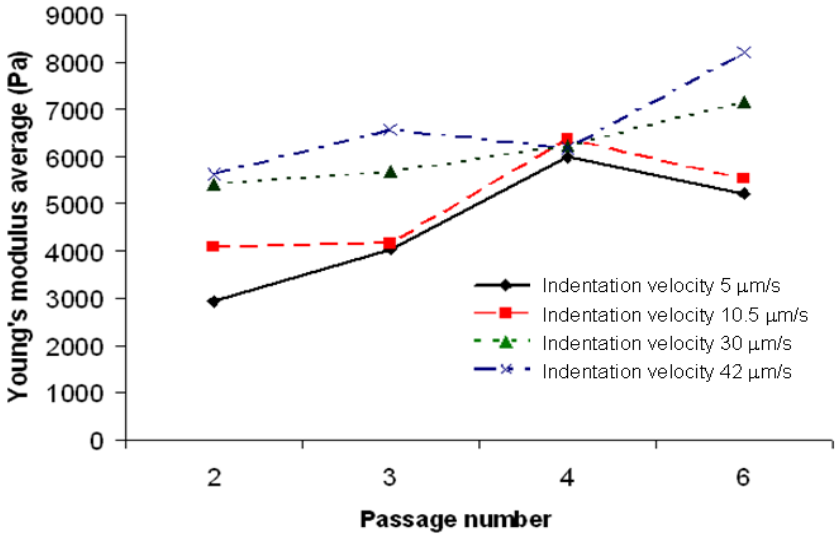

Figure 6.43 Young's modulus of normal cells, corresponding to passage 2, 3, 4 and 6.

Table 6.21 shows the apparent Young's modulus averages for the keloid and normal cells for each velocity for experiments 1 and 2. Experiments 1 and 2 demonstrate that it is possible and practical to measure the mechanical properties of cells with the AFM. The results also indicate that keloid cells are in general stiffer than normal cells. The average Young's modulus value for the keloid cells calculated from the data obtained from experiments 1 and 2 over the range of velocities tested is 17349.4 Pa (see Table 6.21). The corresponding average value for the normal cells is 8222.2 Pa.

	Keloid	Normal	% difference
Velocity µm/s	E (Pa), average per velocity	E (Pa) average per velocity	
5	14904.8	6806.3	118
10.5	15947.3	7711.9	106
30	18685.3	8882.1	110
42	19860.1	9488.5	109
Average 4 velocities	17349.4	8222.2	111

Table 6.21 Apparent Young's modulus average per velocity and total for the 4 velocities considering experiments 1 and 2.

From Table 6.21 it can be deduced that keloid cells are approximately 111% stiffer than normal cells.

6.12 Dynamic response of cells.

Figures 6.44-6.53 are apparent Young's modulus vs Indentation velocity plots corresponding to the 5 patients from experiment 1. Only the cases in which the apparent Young's modulus of the cell increased with the indentation velocity are shown. Such phenomenon is not present in all the cells tested, with the reason being unclear. However, this behaviour may be explained by the fact that the location of the cantilever tip (see section 6.8.1) influences cell behaviour. Upon inspection of Figures 6.44-6.53 it can be seen that the increase of apparent Young's modulus with velocity follows an approximately linear trend. The same phenomenon was observed in the results of experiment 2 (not plotted here).

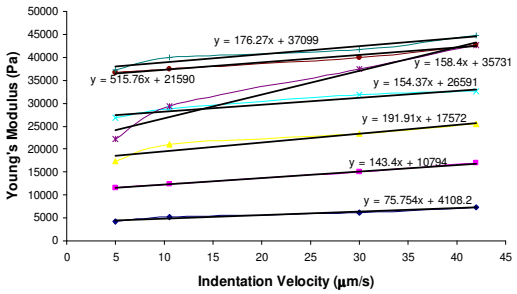

Figure 6.44 Keloid cells, patient 1.

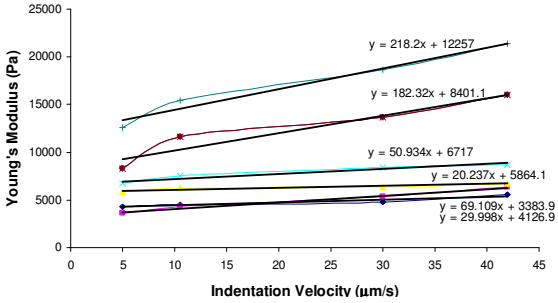

Figure 6.45 Normal cell, patient 1.

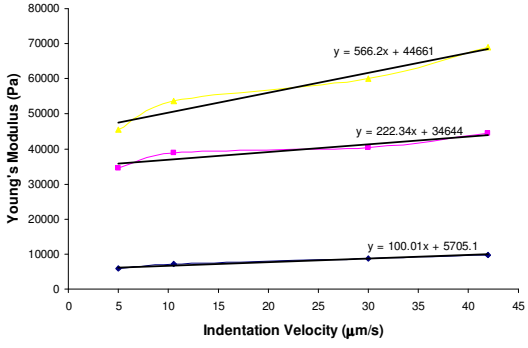

Figure 6.46 Keloid cells, patient 2.

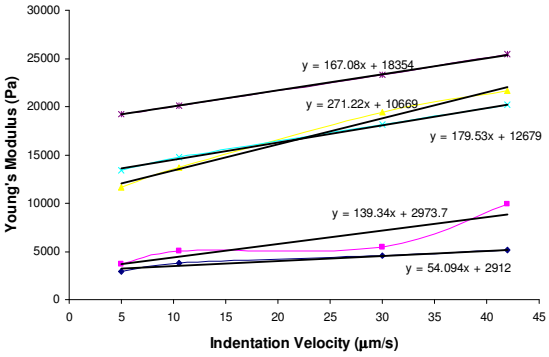

Figure 6.47 Normal, patient 2.

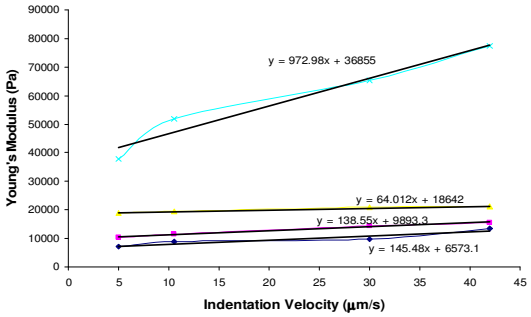

Figure 6.48 Keloid cells, patient 3.

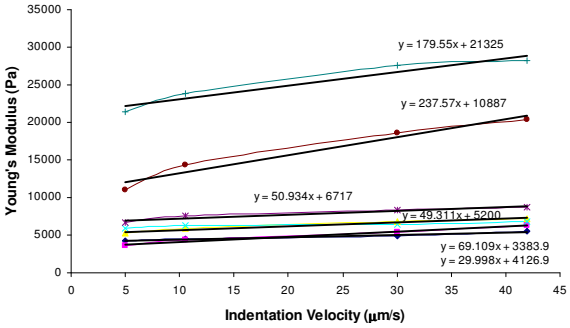

Figure 6.49 Normal cells, patient 3.

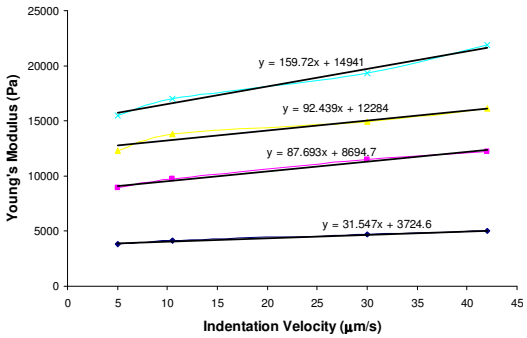

Figure 6.50 Keloid cells, patient 4.

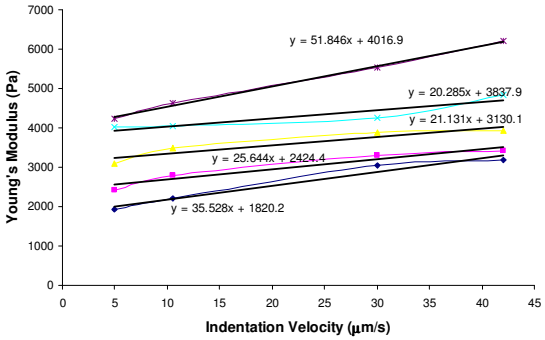

Figure 6.51 Normal cells, patient 4.

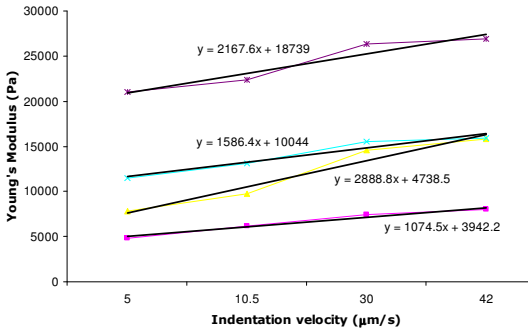

Figure 6.52 Keloid cells, patient 5.

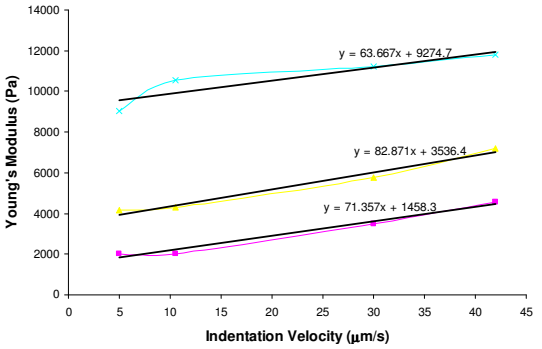

Figure 6.53 Normal cells, patient 5.

Chapter 7

Conclusions.

7.1 Introduction.

This thesis has described an investigation into the mechanical properties of single keloid and normal skin fibroblast cells for the purpose of establishing if there is a quantitative difference between the mechanical behaviour of the two types of cells. Experiments consisting of using an AFM to indent single Keloid and normal skin fibroblast cells from five patients were described. Values for the apparent Young's modulus of the cells were then calculated by fitting the experimental data obtained using Hertz's model. In addition, a novel, coupled numerical model was developed that provides accurate quantification of the hydrodynamic drag forces present during AFM measurements of soft samples in fluids without the need to determine empirical coefficients or extrapolate data.

7.2 Keloid scars and mechanical properties of cells.

In Chapters 2 and 3 the functions of the human skin were discussed and the normal wound healing process was described. Keloid scars, which form as a result of excessive tissue repair, were introduced and their prevalence, symptoms and impact on sufferers was highlighted. It was revealed that the mechanism by which keloid scars form is currently not well understood and consequently no effective treatments exist to date. Current ideas and theories

related to the keloid scar formation process were discussed and current treatments were described. The structure and properties of living cells was then discussed. It was highlighted that biological organisms are under direct influence of mechanical loads during their life cycle and that an understanding of the mechanical behaviour of living cells can be of great benefit. It was revealed that to date, no experimental work has been published on the mechanical properties of single keloids cells but that such information, if it was available, could be of significant importance in the future to researchers looking to develop effective treatments for the prevention, reduction or removal of keloid scars.

7.3 Experimental techniques to study mechanical properties of single cells.

Chapter 3 revealed that the need to understand the mechanical properties of cells and their relationship with their chemical and biological functions had prompted researchers to look for ways to investigate these relationships. Five types of techniques were identified that have been used to date to study the mechanical properties of living cells. The five technique types: micropipette aspiration, optical tweezers, engineering substrates, magnetic methods and AFM were described and discussed in detail. The versatility of AFM and its usefulness for investigating the mechanical properties of living cells was highlighted.

7.4 Drag forces.

In Chapter 4 the forces present in contact mode AFM experimentation in fluids were discussed and the advantages and disadvantages of undertaking AFM experimentation in an aqueous medium were highlighted. It was revealed that the use of AFM for soft samples in fluid environments results in the introduction of a hydrodynamic drag force due to viscous friction of the cantilever with the surrounding fluid through which it moves and that in cases where the magnitudes of the measured forces are low, this drag force can be of a similar order to the reaction force of the sample. It was concluded that under such circumstances if allowance is not made for the hydrodynamic drag force then significant errors in measurement can occur. Drag force was analysed in detail and existing mathematical drag force models were reviewed. It was noted that many previous attempts to correct AFM measurements for hydrodynamic drag effects had consisted of estimating the drag force at some distance above the specimen then using this value to correct the measurements taken on contact. It

was argued however, that these approaches would lead to significant underestimation of the actual hydrodynamic drag at contact. A further drawback of existing models was highlighted, that they generally rely on empirical coefficients which must be determined through experimentation.

7.5 Coupled drag force model.

Chapter 5 described a novel, coupled finite element based model that provides quantification of the drag force in AFM measurements of soft specimens in fluids, consequently enabling more accurate interpretation of the data obtained from AFM experimentation. In order to investigate hydrodynamic drag force effects, data from AFM experimentation in fluid media using a V-shaped cantilever fitted with a pyramidal tip was presented. The experimental data obtained was used to validate the model, which was shown to accurately account for drag forces in AFM in fluid media over a wide range of tip velocities, tip-sample separations and fluid viscosities. Average errors of 15% were observed between model predictions and experimental results. The model was also compared with an existing analytical model that attempts to quantify hydrodynamic drag force effects in AFM in fluid media. The comparison highlighted the capabilities and advantages of the novel model with accurate results being obtained without the need to determine model parameters from experimental data prior to its use. The investigation confirmed that drag force dependence on tip speed is essentially linear in nature. In addition, the expected increase in drag force at distances close to the sample was observed both in the experimental tests and in the numerical predictions from the model. In order to demonstrate its usefulness and value, the novel model was used to correct AFM measurements for indentation tests on a number of keloid cells in a fluid medium (PBS). In the particular examples considered the effect of correcting for drag force resulted in a maximum 3.25% difference in the resulting Young's modulus calculated. It is expected that the model will enable increased accuracy to be obtained particularly in the case of AFM studies of biological samples in fluids where in vitro measurements are of importance.

7.6 Experimental work.

Chapter 6 described extensive experimental work undertaken in order to establish if the mechanical behaviour of keloid cells differs from normal skin fibroblast cells. The indentation of single keloid and normal skin fibroblast cells

from five patients using AFM were detailed. The methodology for obtaining values for apparent Young's modulus from the experimental data was presented. A significant difference was found between the apparent Young's modulus values of keloid cells compared to normal cells, with keloid cells exhibiting substantially greater stiffness. Extensive statistical significance tests (t-tests) were performed on the data. These tests confirmed that the mean concentration of the Young's modulus values differs between keloid and normal cells. Apparent Young's modulus values of both keloid and normal cells were found to increase with velocity. This effect was attributed to the cytoskeleton reorganisation. In addition, it was argued that the variation in apparent Young's modulus values obtained for different indentations of the same individual cell at a given indentation velocity was due to heterogeneity of the cell and the uncertainty surrounding cell indentation location. It was noted that the results of this extensive experimental investigation will be of benefit to researchers looking for a better understanding of the keloid formation mechanism and for those seeking improved treatments. In addition, it was demonstrated that the AFM is a versatile and accurate instrument that can be used to investigate the mechanical properties of living cells.

7.7 Recommendations for future work.

A potential source of uncertainty in AFM investigations of cells is the inability to accurately determine cell contact point location. This uncertainty makes comparison of experimental data and mechanical properties calculated from such data difficult. Further work is required in order to establish an accurate mechanism that enables specific cell areas to be located for indentation testing purposes. This would possibly require an improvement in the microscope optic system of the AFM.

The investigation described in this thesis is a first step towards an increased understanding of the keloid scar formation process. One possible next step would be to set up a device that can be used to apply stresses on normal cells in order to investigate whether applied stresses are sufficient to trigger changes which could alter the normal wound healing process in such a manner that could lead to keloid scar formation.

List of publications supporting this thesis.

Submitted:

Méndez M. J. V., Alonzo R. T., Snook R, Correia F. E., A Novel Model to Account for the Hydrodynamic Drag Force in AFM Measurements Undertaken in Fluid. Langmiur 2010.

In Process:

Méndez M. J. V., Alonzo R. T., Snook R, Correia F. E., Mechanical properties of single keloid and normal skin fibroblast measured using AFM. Journal of Biomechanics 2010.

Méndez M. J. V., Alonzo R. T., Snook R, Correia F. E., Drag force in AFM including cell geometry. Langmiur 2010.

Conferences:

Modeling of a keloid cell and the used of the atomic force microscope to determine experimental dragging force. 5CIIES, México.

References.

1. Diegelmann, R.F. and Evans, M.C., *Wound healing: An overview of acute, fibrotic and delayed healing.* Frontiers in Bioscience, 2004. **9**: p. 283.

2. Tuan, T.L. and Nichter, L.S., *The molecular basis of keloid and hypertrophic scar formation.* Molecular Medicine Today, 1998. **4**(1): p. 19.

3. Sato, M., Ohshima, N. and Nerem, R.M., *Viscoelastic properties of cultured porcine aortic endothelial cells exposed to shear stress.* Journal of Biomechanics, 1996. **29**(4): p. 461.

4. Sato, M., Levesque, M.J. and Nerem, R.M., *Micropipette aspiration of cultured bovine aortic endothelial cells exposed to shear stress.* Arteriosclerosis, 1987. **7**(3): p. 276.

5. Svoboda, K. and Block, S.M., *Biological applications of optical forces.* Annual review of biophysics and biomolecular structure, 1994. **23**: p. 285.

6. Fabry, B., Maksym, G. N.,Hubmayr, R. D., Butler, J.P., Fredberg J. J., *Implications of heterogeneous bead behaviour on cells mechanical properties measured with magnetic twisting cytometry.* Journal of Magnetism and Magnetic Materials., 1999. **194**: p. 120-125.

7. Nagayama, K., Nagano, Y., Sato, M. and Matsumoto, T., *Effect of actin filament distribution on tensile properties of smooth muscle cells obtained from rat thoracic aortas.* Journal of Biomechanics, 2006. **39**(2): p. 293.

8. Lim, C.T., Zhou, E.H. and Quek, S.T., *Mechanical models for living cells-a review.* Journal of Biomechanics, 2006. **39**(2): p. 195.

9. Miyazaki, H., Hasegawa, Y. and Hayashi, K., *Tensile properties of contractile and synthetic vascular smooth muscle cells.* JSME International Journal, Series C: Mechanical Systems, Machine Elements and Manufacturing, 2002. **45**(4): p. 870.

10. Wang, N., Butler, J.P. and Ingber, D.E., *Mechanotransduction across the cell surface and through the cytoskeleton.* Science, 1993. **260**(5111): p. 1124.

11. Dao, M., Lim, C.T. and Suresh, S., *Mechanics of the human red blood cell deformed by optical tweezers.* Journal of the Mechanics and Physics of Solids, 2003. **51**(11-12): p. 2259.

12. Rockwell, W.B., Cohen, I.K. and Ehrlich, H.P., *Keloids and Hypertrophic Scars: A Comprehensive Review* Plastic and Reconstructive Surgery., 1989. **84**(5): p. 827-837.

13. Suresh, S., Spatz, J., Mills, J.P., Micoulet, A., Dao, M., Lim, C.T., Beil, M. and Seufferlein, T., *Connections between single-cell biomechanics and human disease states: Gastrointestinal cancer and malaria.* Acta Biomaterialia, 2005. **1**(1): p. 15.

14. Yamazaki, D., Kurisu, S. and Takenawa, T., *Regulation of cancer cell motility through actin reorganization.* Cancer Science, 2005. **96**(7): p. 379.

15. Rotsch, C., Jacobson, K. and Radmacher, M., *Dimensional and mechanical dynamics of active and stable edges in motile fibroblasts investigated by using atomic force microscopy.* Proceedings of the National Academy of Sciences of the United States of America, 1999. **96**(3): p. 921.

16. Liu, W.F. and Chen, C.S., *Engineering biomaterials to control cell function.* Materials Today, 2005. **8**(12): p. 28.

17. Brock, A., Chang, E., Ho, C.C., LeDuc, P., Jiang, X., Whitesides, G.M. and Ingber, D.E., *Geometric determinants of directional cell motility revealed using microcontact printing.* Langmuir, 2003. **19**(5): p. 1611.

18. Dembo, M. and Wang, Y.L., *Stresses at the cell-to-substrate interface during locomotion of fibroblasts.* Biophysical Journal, 1999. **76**(4): p. 2307.

19. Pelham Jr, R.J. and Wang, Y.L., *High resolution detection of mechanical forces exerted by locomoting fibroblasts on the substrate.* Molecular Biology of the Cell, 1999. **10**(4): p. 935.

20. Binnig, G., and Rohrer, H., *"Scanning Tunneling Microscopy - From Birth to Adolescence".* Nobel lecture, December 8. 1986.

21. Bayat, A., Bock, O., Mrowietz, U., Ollier, W.E. and Ferguson, M.W., *Genetic susceptibility to keloid disease and hypertrophic scarring: Transforming growth factor beta1 common polymorphisms and plasma levels.* Plastic and Reconstructive Surgery, 2003. **111**(2): p. 535.

22. Breasted, J.H., *The Edwin Smith surgical papyrus.* Chiacago: University of Chicago Press., 1930. **1** p. 403-406.

23. Murray, J.C., Pollack, S.V. and Pinnell, S.R., *Keloids: A review.* Journal of the American Academy of Dermatology, 1981. **4**(4): p. 461.

24. Niessen, F.B., Spauwen, P.H., Schalkwijk, J. and Kon, M., *On the Nature of Hypertrophic Scars and Keloids: A Review.* American Society of Plastic Surgeons, 1999. **104**(5).

25. Kanitakis, J., *Anatomy, histology and immunohistochemistry of normal human skin.* European Journal of Dermatology, 2002. **12**(4): p. 390.

26. MacNeil, S., *Progress and opportunities for tissue-engineered skin.* Nature, 2007. **445**(7130): p. 874-880.

27. Martin, P., *Wound healing - Aiming for perfect skin regeneration.* Science, 1997. **276**(5309): p. 75.

28. Slemp, A.E. and Kirschner, R.E., *Keloids and scars: A review of keloids and scars, their pathogenesis, risk factors, and management.* Current Opinion in Pediatrics, 2006. **18**(4): p. 396.

29. Bayat, A., McGrouther, D.A. and Ferguson, M.W.J., *Skin scarring.* British Medical Journal, 2003. **326**(7380): p. 88.

30. Brody, G.S., Peng, S.T.J. and Landel, R.F., *The etiology of hypertrophic scar contracture: Another view.* Plastic and Reconstructive Surgery, 1981. **67**(5): p. 673.

31. Neely, A.N., Clendening, C.E., Gardner, J., Greenhalgh, D.G. and Warden, G.D., *Gelatinase activity in keloids and hypertrophic scars.* Wound Repair and Regeneration, 1999. **7**(3): p. 166.

32. Zimin, W., Zhongyu, G., Yi, S., Yi, S., Zihao, L., Hua, J., Tiesheng, H., Qiugen, W., Xiangbin, Y., Xiaohai, Z., Hong, W., and Youxin, J., *Inhibition of Smad3 expression decreases collagen synthesis in keloid disease fibroblasts.* Journal of plastic, reconstructive & aesthetic surgery : JPRAS, 2007. **60**(11): p. 1193.

33. Gira, A.K., Brown, L.F., Washington, C.V., Cohen, C. and Arbiser, J.L., *Keloids demonstrate high-level epidermal expression of vascular endothelial growth factor.* Journal of the American Academy of Dermatology, 2004. **50**(6): p. 850.

34. Al-Attar, A., Mess, S., Thomassen, J.M., Kauffman, C.L. and Davison, S.P., *Keloid Pathogenesis and Treatment.* Plastic & Reconstructive Surgery, 2006. **117**(1): p. 286-300.

35. Hillmer, M.P. and MacLeod, S.M., *Experimental Keloid Scar Models: A Review of Methodological Issues.* Journal of Cutaneous Medicine and Surgery: Incorporating Medical and Surgical Dermatology, 2002. **6**(4): p. 354.

36. Lee, J.S., *Cytokine delivery and tissue engineering.* Yonsei Medical Journal, 2000. **41**(6): p. 704-719.

37. Bock, O., Yu, H., Zitron, S., Bayat, A., Ferguson, M.W.J. and Mrowietz, U., *Studies of transforming growth factors beta 1-3 and their receptors I and II in fibroblast of keloids and hypertrophic scars.* Acta Dermato-Venereologica, 2005. **85**(3): p. 216.

38. Butler, P.D., Wang, Z., Ly, D.P., Longaker, M.T., Koong, A.C. and Yang, G.P., *Unfolded Protein Response Regulation in Keloid Cells.* Journal of Surgical Research.

39. Marneros, A.G., Norris, J.E.C., Olsen, B.R. and Reichenberger, E., *Clinical Genetics of Familial Keloids.* Archives of Dermatology, 2001. **137**(11): p. 1429.

40. Ogawa, R., *Keloid and hypertrophic scarring may result from a mechanoreceptor or mechanosensitive nociceptor disorder.* Medical Hypotheses, 2008. **71**(4): p. 493.

41. Babu, M., Diegelmann, R. and Oliver, N., *Fibronectin is overproduced by keloid fibroblasts during abnormal wound healing.* Molecular and Cellular Boilogy, 1989. **9**(4): p. 1642-1650.

42. Border, W.A. and Noble, N.A., *Transforming Growth Factor {beta} in Tissue Fibrosis.* The New England Journal of Medicine, 1994. **331**(19): p. 1286.

43. Nathan, C. and Sporn, M., *Cytokines in context.* The Journal of Cell Biology, 1991. **113**(5): p. 981.

44. Bao, G. and Suresh, S., *Cell and molecular mechanics of biological materials.* Nat Mater, 2003. **2**(11): p. 715-725.

45. Guanbin, S., Weiqun, Y., Baoan, L., Mian, L., Zezhi, W. and Bochu, W., *Investigation on the viscoelasticity of synchronous hepatocellular carcinoma cells.* Colloids and Surfaces B: Biointerfaces, 2002. **24**(3-4): p. 327.

46. Satoshi, A., Rei, O. and Hiko, H., *Keloid and hypertrophic scar: Neurogenic inflammation hypotheses.* Medical hypotheses, 2008. **71**(1): p. 32.

47. Gilmore, A.P. and Romer, L.H., *Inhibition of focal adhesion kinase (FAK) signaling in focal adhesions decreases cell motility and proliferation.* Molecular Biology of the Cell, 1996. **7**(8): p. 1209-1224.

48. Calnan, J.S. and Copenhagen, H.J., *Autotransplantation of keloid in man.* British Journal of Surgery, 1967. **54**(5): p. 330.

49. Donkor, P., *Head and Neck Keloid: Treatment by Core Excision and Delayed Intralesional Injection of Steroid.* Journal of Oral and Maxillofacial Surgery, 2007. **65**(7): p. 1292.

50. Anderson, T.L., *Fracture mechanics: Fundamentals and applications*. Second ed. 1995: CRC Press.

51. Zheng, M. and Niem, E., *Analysis of the stress concentration factor for a shallow notch by the slip-line field method.* International Jornal of Fatigue, 1997. **19**(3): p. 191-194.

52. Prendergast, P. and Huiskes, R., *The Biomechanics of Wolff's law: Recent advances.* Irish Journal of Medical Science, 1995. **164**(2): p. 152.

53. Akaishi, S., Ogawa, R. and Hyakusoku, H., *Treatment of recurrent earlobe keloids with surgery and high-dose-rate brachytherapy.* Plastic and Reconstructive Surgery, 2009. **123**(1): p. 424.

54. Morosolli, A.R.C., De Oliveira Moura Cardoso, G., Murilo-Santos, L. and Niccoli-Filho, W., *Surgical treatment of earlobe keloid with CO2 laser radiation: Case report and clinical standpoints.* Journal of Cosmetic and Laser Therapy, 2008. **10**(4): p. 226.

55. Meythiaz, A.M., de Mey, A., Lejour, M., *Treatment of keloids by excision and postoperative radiotherapy.* Plastic Surgery, 1992. **15**: p. 13-16.

56. Reiffel, R.S., *Prevention of hypertrophic scars by long-term paper tape application.* Plastic and Reconstructive Surgery, 1995. **96**(7): p. 1715.

57. Philipp, C.M., Scharschmidt, D. and Berlien, H.P., *Laser treatment of scars and keloids - How we do it.* Medical Laser Application, 2008. **23**(2): p. 79.

58. Chrisostomidis, C., Konofaos, P., Chrisostomidis, G., Vasilopoulou, A., Dimitroulis, D., Frangoulis, M. and Papadopoulos, O., *Management of external ear keloids using form-pressure therapy.* Clinical and Experimental Dermatology, 2008. **33**(3): p. 273.

59. Roques, C. and Téot, L., *The use of corticosteroids to treat keloids: A review.* International Journal of Lower Extremity Wounds, 2008. **7**(3): p. 137.

60. De Giorgi, V., Sestini, S., Mannone, F., Papi, F., Alfaioli, B., Gori, A. and Lotti, T., *The use of silicone gel in the treatment of fresh surgical scars: A randomized study.* Clinical and Experimental Dermatology, 2009. **34**(6): p. 688.

61. Liu, W., Wu, X., Gao, Z. and Song, N., *Remodelling of keloid tissue into normal-looking skin.* Journal of Plastic, Reconstructive and Aesthetic Surgery, 2008. **61**(12): p. 1553.

62. Davison, S.P., Dayan, J.H., Clemens, M.W., Sonni, S., Wang, A. and Crane, A., *Efficacy of Intralesional 5-Fluorouracil and Triamcinolone in the Treatment of Keloids.* Aesthetic Surgery Journal, 2009. **29**(1): p. 40.

63. Krusche, T. and Worret, W.-I., *Mechanical properties of keloids in vivo during treatment with intralesional triamcinolone acetonide.* Archives of Dermatological Research, 1995. **287**(3): p. 289.

64. Parikh, D.A., Ridgway, J.M. and Ge, N.N., *Keloid banding using suture ligature: A novel technique and review of literature.* Laryngoscope, 2008. **118**(11): p. 1960.

65. Har-Shai, Y., Brown, W., Labbé, D., Dompmartin, A., Goldine, I., Gil, T., Mettanes, I. and Pallua, N., *Intralesional cryosurgery for the treatment of hypertrophic scars and keloids following aesthetic surgery: The results of a prospective observational study.* International Journal of Lower Extremity Wounds, 2008. **7**(3): p. 169.

66. Caille, N., Thoumine, O., Tardy, Y. and Meister, J.J., *Contribution of the nucleus to the mechanical properties of endothelial cells.* Journal of Biomechanics, 2002. **35**(2): p. 177.

67. Chen, A. and Moy, V.T., *Cross-linking of cell surface receptors enhances cooperativity of molecular adhesion.* Biophysical Journal, 2000. **78**(6): p. 2814.

68. Bausch, A.R. and Kroy, K., *A bottom-up approach to cell mechanics.* Nat Phys, 2006. **2**(4): p. 231.

69. Raucher, D., Stauffer, T., Chen, W., Shen, K., Guo, S., York, J.D., Sheetz, M.P. and Meyer, T., *Phosphatidylinositol 4,5-bisphosphate functions as a second messenger that regulates cytoskeleton-plasma membrane adhesion.* Cell, 2000. **100**(2): p. 221.

70. Alberts, B., Johnson, A., Lewis, J., Raff, M., Roberts, K. and Walter, P., *Molecular Biology of the Cell, Fourth Edition*. 2002: Garland.

71. Mohandas, N. and Evans, E., *Mechanical Properties of the Red Cell Membrane in Relation to Molecular Structure and Genetic Defects.* Annual Review of Biophysics and Biomolecular Structure, 2003. **23**(1): p. 787.

72. Zahalak, G.I., McConnaughey, W.B. and Elson, E.L., *Determination of Cellular Mechanical Properties by Cell Poking, With an Application to Leukocytes.* Journal of Biomechanical Engineering, 1990. **112**(3): p. 283.

73. Suresh, S., *Biomechanics and biophysics of cancer cells.* Acta Biomaterialia, 2007. **3**(4): p. 413.

74. Alberts, B., Johnson, A., Lewis, J., Raff, M., Roberts, K. and Walter, P., *Molecular Biology of the Cell, Fifth Edition*. 2008: Garland Science.

75. Darnell, J.E., Lodish, H. F., Baltimore, D.,, *Molecular cell biology*. 2nd ed. ed. 1990: New York : New York ; Oxford : Scientific American Books ; Distributed by W.H. Freeman.

76. Carmo-Fonseca, M. and David-Ferreira, J.F., *Interactions of intermediate filaments with cell structures.* Electron Microscopy Reviews, 1990. **3**(1): p. 115.

77. Guilak, F., Tedrow, J.R. and Burgkart, R., *Viscoelastic properties of the cell nucleus.* Biochemical and Biophysical Research Communications, 2000. **269**(3): p. 781.

78. Bruce Alberts, D.B., Karen Hopkin, Alexander Johnson, Julian Lewis, Martin Raff, Keith Roberts, Peter Walter, *Essential Cell Biology*. Second Edition ed. 2003: Garland Science/Taylor & Francis Group

79. Sorrell, J.M., Caplan, A.I. and Kwang, W.J., *Chapter 4 Fibroblasts--A Diverse Population at the Center of It All*, in *International Review of Cell and Molecular Biology*. 2009, Academic Press. p. 161-214.

80. Bonn, D., Coussot, P., Huynh, H.T., Bertrand, F. and Debregeas, G., *Rheology of soft glassy materials.* EPL (Europhysics Letters), 2002. **59**(5): p. 786.

81. Fabry, B., Maksym, G.N., Butler, J.P., Glogauer, M., Navajas, D. and Fredberg, J.J., *Scaling the microrheology of living cells.* Physical Review Letters, 2001. **87**(14): p. 148102/1.

82. Alcaraz, J., Buscemi, L., Grabulosa, M., Trepat, X., Fabry, B., Farré, R. and Navajas, D., *Microrheology of Human Lung Epithelial Cells Measured by Atomic Force Microscopy.* Biophysical Journal, 2003. **84**(3): p. 2071.

83. Smith, B.A., Tolloczko, B., Martin, J.G. and Grütter, P., *Probing the Viscoelastic Behavior of Cultured Airway Smooth Muscle Cells with Atomic Force Microscopy: Stiffening Induced by Contractile Agonist.* Biophysical Journal, 2005. **88**(4): p. 2994.

84. Cua, A.B., Wilhelm, K.P. and Maibach, H.I., *Elastic properties of human skin: relation to age, sex, and anatomical region.* Archives of Dermatological Research, 1990. **282**(5): p. 283.

85. Mitchison, J.M. and Swann, M.M., *The Mechanical Properties of the Cell Surface: I. The Cell Elastimeter.* Journal of Experimental Biology, 1954. **31**(3): p. 443.

86. Merkel, R., Nassoy, P., Leung, A., Ritchie, K. and Evans, E., *Energy landscapes of receptor-ligand bonds explored with dynamic force spectroscopy.* Nature, 1999. **397**(6714): p. 50.

87. Waugh, R. and Evans, E.A., *Thermoelasticity of red blood cell membrane.* Biophysical Journal, 1979. **26**(1): p. 115.

88. Liu, K.-K.a.L.C., *Optical tweezers for nanomechanical manipulation and characterization of biological cells.* Keele University, Uk.

89. Wells, P.B., Harris, J.L. and Humphrey, J.D., *Altered Mechanical Behavior of Epicardium Under Isothermal Biaxial Loading.* Journal of Biomechanical Engineering, 2004. **126**(4): p. 492.

90. Bershadsky, A.D., Balaban, N.Q. and Geiger, B., *Adhesion-Dependent Cell Mechanosensitivity*, in *Annual Review of Cell and Developmental Biology*. 2003. p. 677.

91. Petronis, S., Gold, J. and Kasemo, B., *Microfabricated force-sensitive elastic substrates for investigation of mechanical cell-substrate interactions.* Journal of Micromechanics and Microengineering, 2003. **13**(6): p. 900.

92. Chen, C.S., Alonso, J.L., Ostuni, E., Whitesides, G.M. and Ingber, D.E., *Cell shape provides global control of focal adhesion assembly.* Biochemical and Biophysical Research Communications, 2003. **307**(2): p. 355.

93. Solon, J., Levental, I., Sengupta, K., Georges, P.C. and Janmey, P.A., *Fibroblast Adaptation and Stiffness Matching to Soft Elastic Substrates.* 2007. **93**(12): p. 4453.

94. Thoumine, O., Cardoso, O. and Meister, J.-J., *Changes in the mechanical properties of fibroblasts during spreading: a micromanipulation study.* European Biophysics Journal, 1999. **28**(3): p. 222.

95. Lin, S., Chen, J.-L. and Lin, H.-W., *Measurements of the forces in protein interactions with atomic force microscopy.* Current Proteimics., 2005. **2**: p. 55-81.

96. Maksym, G.N., Fabry, B., Butler, J.P., Navajas, D., Tschumperlin, D.J., Laporte, J.D. and Fredberg, J.J., *Mechanical properties of cultured human airway smooth muscle cells from 0.05 to 0.4 Hz.* Journal of Applied Physiology, 2000. **89**(4): p. 1619.

97. Fabry, B., Maksym, G.N., Shore, S.A., Moore, P.E., Panettieri Jr, R.A., Butler, J.P. and Fredberg, J.J., *Selected contribution: Time course and heterogeneity of contractile responses in cultured human airway smooth muscle cells.* Journal of Applied Physiology, 2001. **91**(2): p. 986.

98. Shin, D. and Athanasiou, K., *Cytoindentation for obtaining cell biomechanical properties.* Journal of Orthopaedic Research, 1999. **17**(6): p. 880.

99. Lai, K.W.C., and Li. W. J., *Fabrication of High-Aspect-Ratio Probes for Potential Applications in Biological Cellular Surgery.* Centre for Micro and Nano Systems,The Chinese University of Hong Kong.

100. Yan, J., Skoko, D. and Marko, J.F., *Near-field-magnetic-tweezer manipulation of single DNA molecules.* Physical Review E - Statistical, Nonlinear, and Soft Matter Physics, 2004. **70**(1 1): p. 011905.

101. Chowdhury, T.K., *Fabrication of extremely fine glass micropipette electrodes.* Journal of Physics E: Scientific Instruments, 1969. **2**(12): p. 1087.

102. Hanein, Y., Schabmueller, C.G.J., Holman, G., Lücke, P., Denton, D.D. and Böhringer, K.F., *High-aspect ratio submicrometer needles for intracellular applications.* Journal of Micromechanics and Microengineering, 2003. **13**(4): p. S91.

103. Terreros, D.A. and Grantham, J.J., *Marshall Barber and the origins of micropipette methods.* The American journal of physiology, 1982. **242**(3): p. F293.

104. Hochmuth, R.M., *Micropipette aspiration of living cells.* Journal of Biomechanics, 2000. **33**(1): p. 15.

105. Wolfe, J. and Steponkus, P.L., *Mechanical Properties of the Plasma Membrane of Isolated Plant Protoplasts : Mechanism of Hyperosmotic and Extracellular Freezing Injury.* Plant Physiology, 1983. **71**(2): p. 276.

106. Schmid-Schönbein, G.W., Sung, K.L., Tözeren, H., Skalak, R. and Chien, S., *Passive mechanical properties of human leukocytes.* Biophysical Journal, 1981. **36**(1): p. 243.

107. Evans, E.A., Waugh, R. and Melnik, L., *Elastic area compressibility modulus of red cell membrane.* Biophysical Journal, 1976. **16**(6): p. 585.

108. Shao, J.Y. and Hochmuth, R.M., *Micropipette suction for measuring piconewton forces of adhesion and tether formation from neutrophil membranes.* Biophysical Journal, 1996. **71**(5): p. 2892.

109. Ashkin, A., *Optical trapping and manipulation of neutral particles using lasers.* Proceedings of the National Academy of Sciences of the United States of America, 1997. **94**(10): p. 4853.

110. Neuman, K.C. and Block, S.M., *Optical trapping.* Review of Scientific Instruments, 2004. **75**(9): p. 2787.

111. Williams, M.C., *Optical Tweezers: Measuring Piconewton Forces.* North-eastern University, 2002.

112. Mammen, M., Helmerson, K., Kishore, R., Choi, S.-K., Phillips, W.D. and Whitesides, G.M., *Optically controlled collisions of biological objects to evaluate potent polyvalent inhibitors of virus-cell adhesion.* Chemistry & Biology, 1996. **3**(9): p. 757.

113. Mangeol, P., Côte, D., Bizebard, T., Legrand, O. and Bockelmann, U., *Probing DNA and RNA single molecules with a double optical tweezer.* European Physical Journal E, 2006. **19**(3): p. 311.

114. Zhuang, X., *Unraveling DNA condensation with optical tweezers.* Science, 2004. **305**(5681): p. 188.

115. Day, C., *Optical trap resolves the stepwise transfer of genetic information from DNA to RNA.* Physics Today, 2006. **59**(1): p. 26.

116. Bouchiat, C., Wang, M.D., Allemand, J.F., Strick, T., Block, S.M. and Croquette, V., *Estimating the persistence length of a worm-like chain molecule from force-extension measurements.* Biophysical Journal, 1999. **76**(1 I): p. 409.

117. Abbondanzieri, E.A., Greenleaf, W.J., Shaevitz, J.W., Landick, R. and Block, S.M., *Direct observation of base-pair stepping by RNA polymerase.* Nature, 2005. **438**(7067): p. 460.

118. Kimura, Y. and Bianco, P.R., *Single molecule studies of DNA binding proteins using optical tweezers.* Analyst, 2006. **131**(8): p. 868.

119. Ashkin, A. and Dziedzic, J.M., *Optical trapping and manipulation of single living cells using infra-red laser beams.* Berichte der Bunsengesellschaft/Physical Chemistry Chemical Physics, 1989. **93**(3): p. 254.

120. Ashkin, A., Dziedzic, J.M., Bjorkholm, J.E. and Chu, S., *Observation of a single-beam gradient force optical trap for dielectric particles.* Optics Letters, 1986. **11**(5): p. 288.

121. Lang, M.J., Fordyce, P.M. and Block, S.M., *Combined optical trapping and single-molecule fluorescence.* Journal of Biology, 2003. **2**(1).

122. Sow, C.H., Bettiol, A.A., Lee, Y.Y.G., Cheong, F.C., Lim, C.T. and Watt, F., *Multiple-spot optical tweezers created with microlens arrays fabricated by proton beam writing.* Applied Physics B: Lasers and Optics, 2004. **78**(6): p. 705.

123. Mills, J.P., Qie, L., Dao, M., Lim, C.T. and Suresh, S., *Nonlinear elastic and viscoelastic deformation of the human red blood cell with optical tweezers.* Mechanics & chemistry of biosystems : MCB., 2004. **1**(3): p. 169.

124. Wottawah, F., Schinkinger, S., Lincoln, B., Ananthakrishnan, R., Romeyke, M., Guck, J. and Käs, J., *Optical Rheology of Biological Cells.* Physical Review Letters, 2005. **94**(9): p. 098103.

125. Takano, H., Sul, J.Y., Mazzanti, M.L., Doyle, R.T., Haydon, P.G. and Porter, M.D., *Micropatterned substrates: Approach to probing intercellular communication pathways.* Analytical Chemistry, 2002. **74**(18): p. 4640.

126. Balaban, N.Q., Schwarz, U.S., Riveline, D., Goichberg, P., Tzur, G., Sabanay, I., Mahalu, D., Safran, S., Bershadsky, A., Addadi, L., and Geiger, B., *Force and focal adhesion assembly: A close relationship studied using elastic micropatterned substrates.* Nature Cell Biology, 2001. **3**(5): p. 466.

127. Zamir, E. and Geiger, B., *Molecular complexity and dynamics of cell-matrix adhesions.* Journal of Cell Science, 2001. **114**(20): p. 3583.

128. Shaikh Mohammed, J., DeCoster, M.A. and McShane, M.J., *Fabrication of interdigitated micropatterns of self-assembled polymer nanofilms containing cell-adhesive materials.* Langmuir, 2006. **22**(6): p. 2738.

129. Sorribas, H., Padeste, C. and Tiefenauer, L., *Photolithographic generation of protein micropatterns for neuron culture applications.* Biomaterials, 2002. **23**(3): p. 893.

130. Gray, D.S., Tien, J. and Chen, C.S., *Repositioning of cells by mechanotaxis on surfaces with micropatterned Young's modulus.* Journal of Biomedical Materials Research - Part A, 2003. **66**(3): p. 605.

131. Harris, A.K., Wild, P. and Stopak, D., *Silicone rubber substrata: a new wrinkle in the study of cell locomotion.* Science, 1980. **208**(4440): p. 177-179.

132. Harris, A.K., *Fibroblasts and myofibroblasts. Methods Enzymol.* Methods Enzymol, 1988. **163**: p. 623-642.

133. Kleinschmidt, A., Büchel, C., Zeki, S. and Frackowiak, R.S.J., *Human brain activity during spontaneously reversing perception of ambiguous figures.* Proceedings of the Royal Society B: Biological Sciences, 1998. **265**(1413): p. 2427.

134. Matthews, B.D., Overby, D.R., Alenghat, F.J., Karavitis, J., Numaguchi, Y., Allen, P.G. and Ingber, D.E., *Mechanical properties of individual focal adhesions probed with a magnetic microneedle.* Biochemical and Biophysical Research Communications, 2004. **313**(3): p. 758.

135. Meyer, C.J., Alenghat, F.J., Rim, P., Fong, J.H.J., Fabry, B. and Ingber, D.E., *Mechanical control of cyclic AMP signalling and gene transcription through integrins.* Nature Cell Biology, 2000. **2**(9): p. 666.

136. Bausch, A.R., Möller, W. and Sackmann, E., *Measurement of local viscoelasticity and forces in living cells by magnetic tweezers.* Biophysical Journal, 1999. **76**(1 I): p. 573.

137. Van Vliet, K.J., Bao, G. and Suresh, S., *The biomechanics toolbox: Experimental approaches for living cells and biomolecules.* Acta Materialia, 2003. **51**(19): p. 5881.

138. Tortonese, M., Barrett, R.C. and Quate, C.F., *Atomic resolution with an atomic force microscope using piezoresistive detection.* Applied Physics Letters, 1993. **62**(8): p. 834.

139. Binnig, G., Quate, C.F. and Gerber, C., *Atomic Force Microscope.* Physical Review Letters, 1986. **56**(9): p. 930.

140. Florin, E.L., Rief, M., Lehmann, H., Ludwig, M., Dornmair, C., Moy, V.T. and Gaub, H.E., *Sensing specific molecular interactions with*

the atomic force microscope. Biosensors and Bioelectronics, 1995. **10**(9-10): p. 895.

141. Lu, G. and Zangari, G., *Electrodeposition of platinum nanoparticles on highly oriented pyrolitic graphite: Part II: Morphological characterization by atomic force microscopy.* Electrochimica Acta, 2006. **51**(12): p. 2531.

142. Li, Z.H., Wang, X.Q., Wang, M., Wang, F.F. and Ge, H.L., *Preparation and tribological properties of the carbon nanotubes-Ni-P composite coating.* Tribology International, 2006. **39**(9): p. 953.

143. Sudam, B.M. and Nichols, M.F. *Surface roughness of plasma polymerized films by AFM*. in *Annual International Conference of the IEEE Engineering in Medicine and Biology - Proceedings*. 1994.

144. Ryan, G.W., *Anisotropy of surface roughness on aluminium sheet studied by atomic force microscopy.* Microscopy and Microanalysis, 2000. **6**(2): p. 137.

145. Koinkar, V.N. and Bhushan, B., *Microtribological studies of unlubricated and lubricated surfaces using atomic force/friction force microscopy.* Journal of Vacuum Science and Technology A: Vacuum, Surfaces and Films, 1996. **14**(4): p. 2378.

146. Tambe, N.S. and Bhushan, B., *A new atomic force microscopy based technique for studying nanoscale friction at high sliding velocities.* Journal of Physics D: Applied Physics, 2005. **38**(5): p. 764.

147. Janovjak, H., Müller, D.J. and Humphris, A.D.L., *Molecular force modulation spectroscopy revealing the dynamic response of single bacteriorhodopsins.* Biophysical Journal, 2005. **88**(2): p. 1423.

148. Willemsen, O.H., Snel, M.M.E., Cambi, A., Greve, J., De Grooth, B.G. and Figdor, C.G., *Biomolecular Interactions Measured by Atomic Force Microscopy.* Biophysical Journal, 2000. **79**(6): p. 3267.

149. Hansma, H.G. and Pietrasanta, L., *Atomic force microscopy and other scanning probe microscopies.* Current Opinion in Chemical Biology, 1998. **2**(5): p. 579.

150. Wu, Y., Cai, J., Cheng, L., Xu, Y., Lin, Z., Wang, C. and Chen, Y., *Atomic force microscope tracking observation of Chinese hamster ovary cell mitosis.* Micron, 2006. **37**(2): p. 139.

151. Kasas, S., Thomson, N.H., Smith, B.L., Hansma, P.K., Miklossy, J. and Hansma, H.G., *Biological applications of the AFM: From single molecules to organs.* International Journal of Imaging Systems and Technology, 1997. **8**(2): p. 151.

152. Li, J., Casell, A. and Dai, H. , *Carbon Nanotube tips for MAC mode AFM measurements in liquids, Aplication note.* Chemistry Department, Stanford University, Agilent technologies.

153. Bykov, V.A., Novikov, Y.A., Rakov, A.V. and Shikin, S.M., *Defining the parameters of a cantilever tip AFM by reference structure.* Ultramicroscopy, 2003. **96**(2): p. 175.

154. Dorrestijn, M., Bietsch, A., Gerber, C. and Meyer, E., *A tunnelling displacement sensor based on a squeezable molecular bilayer.* Nanotechnology, 2006. **17**(9): p. 2242.

155. Brugger, J., Buser, R.A. and De Rooij, N.F., *Micromachined atomic force microprobe with integrated capacitive read-out.* Journal of Micromechanics and Microengineering, 1992. **2**(3): p. 218.

156. Yacoot, A. and Koenders, L., *From nanometric to millimetre: A feasibility study of the combination of scanning probe microscopy and combined optical and x-ray interferometry.* Measurement Science and Technology, 2003. **14**(9): p. N59.

157. Stark, R.W., *Optical lever detection in higher eigenmode dynamic atomic force microscopy.* Review of Scientific Instruments, 2004. **75**(11): p. 5053.

158. Young-Sik, K., Hyo-Jin, N., Seong-Moon, C., Dong-Chun, K. and Jong-Uk, B. *A self-actuating PZT cantilever integrated with piezoresistor sensor for AFM with high speed parallel operation*. in *Micro Electro Mechanical Systems, 2002. The Fifteenth IEEE International Conference on*. 2002.

159. Ohler, B., *Practical Advice on the Determination of Cantilever Spring Constants.* Veeco Instruments inc., 2007: p. 1-12.

160. Beil, M., Micoulet, A., Von Wichert, G., Paschke, S., Walther, P., Omary, M.B., Van Veldhoven, P.P., Gern, U., Wolff-Hieber, E., Eggermann, J., Waltenberger, J., Adler, G., Spatz, J., and Seufferlein, T., *Sphingosylphosphorylcholine regulates keratin network architecture and visco-elastic properties of human cancer cells.* Nature Cell Biology, 2003. **5**(9): p. 803.

161. Cole, K.S., *Surface forces of the arbacia egg.* Journal of Cellular and Comparative Physiology, 1932. **1**(1).

162. Radmacher, M., Fritz, M., Cleveland, J.P., Walters, D.A. and Hansma, P.K., *Imaging adhesion forces and elasticity of lysozyme adsorbed on mica with the atomic force microscope.* Langmuir, 2002. **10**(10): p. 3809.

163. Vinckier, A. and Semenza, G., *Measuring elasticity of biological materials by atomic force microscopy.* FEBS Letters, 1998. **430**(1-2): p. 12.

164. Alcaraz, J., Buscemi, L., Puig-De-Morales, M., Colchero, J., Baró, A. and Navajas, D., *Correction of microrheological measurements of soft samples with atomic force microscopy for the hydrodynamic drag on the cantilever.* Langmuir, 2002. **18**(3): p. 716.

165. Sadewasser, S., Carl, P., Glatzel, T. and Lux-Steiner, M.C., *Influence of uncompensated electrostatic force on height measurements in non-contact atomic force microscopy.* Nanotechnology, 2004. **15**(2): p. S14.

166. Flügge, W., *Viscoelasticity*. 1967: Blaisdell Publishing Company.

167. Butt, H.J., *Measuring electrostatic, van der Waals, and hydration forces in electrolyte solutions with an atomic force microscope.* Biophysical Journal, 1991. **60**(6): p. 1438.

168. Frisbie, C.D., Rozsnyai, L.F., Noy, A., Wrighton, M.S. and Lieber, C.M., *Functional Group Imaging by Chemical Force Microscopy.* Science, 1994. **265**(5181): p. 2071.

169. Noy, A., Vezenov, D.V. and Lieber, C.M., *CHEMICAL FORCE MICROSCOPY.* Annual Review of Materials Science, 2003. **27**(1): p. 381.

170. Ma, H., Jimenez, J. and Rajagopalan, R., *Brownian Fluctuation Spectroscopy Using Atomic Force Microscopes.* Langmuir, 2000. **16**(5): p. 2254.

171. Janovjak, H., Struckmeier, J. and Müller, D.J., *Hydrodynamic effects in fast AFM single-molecule force measurements.* European Biophysics Journal, 2005. **34**(1): p. 91.

172. Chen, G.Y., Warmack, R.J., Oden, P.I. and Thundat, T. *Transient response of tapping scanning force microscopy in liquids*. 1996: AVS.

173. Brenner, H., *The slow motion of a sphere through a viscous fluid towards a plane surface.* Chemical Engineering Science, 1961. **16**(3-4): p. 242.

174. Cox, R.G. and Brenner, H., *The slow motion of a sphere through a viscous fluid towards a plane surface-II Small gap widths, including inertial effects.* Chemical Engineering Science, 1967. **22**(12): p. 1753.

175. O'Shea, S.J. and Welland, M.E., *Atomic Force Microscopy at Solid-Liquid Interfaces.* Langmuir, 1998. **14**(15): p. 4186.

176. Hosaka, H., Itao, K. and Kuroda, S., *Damping characteristics of beam-shaped micro-oscillators.* Sensors and Actuators A: Physical, 1995. **49**(1-2): p. 87.

177. Mahaffy, R.E., Shih, C.K., MacKintosh, F.C. and Käs, J., *Scanning Probe-Based Frequency-Dependent Microrheology of Polymer Gels and Biological Cells.* Physical Review Letters, 2000. **85**(4): p. 880.

178. Nemes, C., Rozlosnik, N. and Ramsden, J.J., *Direct measurement of the viscoelasticity of adsorbed protein layers using atomic force microscopy.* Physical Review E, 1999. **60**(2): p. R1166.

179. Radmacher, M., Fritz, M., Kacher, C.M., Cleveland, J.P. and Hansma, P.K., *Measuring the viscoelastic properties of human platelets with the atomic force microscope.* Biophysical Journal, 1996. **70**(1): p. 556.

180. Walser, R., Mark, A.E. and van Gunsteren, W.F., *On the validity of Stokes' law at the molecular level.* Chemical Physics Letters, 1999. **303**(5-6): p. 583.

181. Vinogradova, O.I. and Yakubov, G.E., *Dynamic Effects on Force Measurements. 2. Lubrication and the Atomic Force Microscope.* Langmuir, 2003. **19**(4): p. 1227.

182. Vinogradova, O.I. and Yakubov, G.E., *Surface roughness and hydrodynamic boundary conditions.* Physical Review E (Statistical, Nonlinear, and Soft Matter Physics), 2006. **73**(4): p. 045302.

183. Clifford, C.A. and Seah, M.P., *The determination of atomic force microscope cantilever spring constants via dimensional methods for nanomechanical analysis.* Nanotechnology, 2005. **16**(9): p. 1666.

184. Barnocky, G. and Davis, R.H., *The effect of Maxwell slip on the aerodynamic collision and rebound of spherical particles.* Journal of Colloid And Interface Science, 1988. **121**(1): p. 226.

185. Butt, H.J., Siedle, P., Seifert, K., Fendler, K., Seeger, T., Bamberg, E., Weisenhorn, A.L., Goldie, K. and Engel, A., *Scan speed limit in atomic force microscopy.* Journal of Microscopy, 1993. **169**(1): p. 75.

186. Albrecht, T.R., Akamine, S., Carver, T.E. and Quate, C.F., *Microfabrication of cantilever styli for the atomic force microscope.* Journal of Vacuum Science & Technology A: Vacuum, Surfaces, and Films, 1990. **8**(4): p. 3396.

187. Sader, J.E., *Parallel beam approximation for V-shaped atomic force microscope cantilevers.* Review of Scientific Instruments, 1995. **66**(9): p. 4583.

188. Sader, J.E. and White, L., *Theoretical analysis of the static deflection of plates for atomic force microscope applications.* Journal of Applied Physics, 1993. **74**(1): p. 1.

189. Tortonese, M., *Cantilevers And Tips For Atomic Force Microscopy.* IEEE Eng. Med. Biol., 1997. **16**(28).

190. Cleveland, J.P., Manne, S., Bocek, D. and Hansma, P.K., *A nondestructive method for determining the spring constant of cantilevers for scanning force microscopy.* Review of Scientific Instruments, 1993. **64**(2): p. 403.

191. Timoshenko, S., 1878-1972., *History of strength of materials : with a brief account of the history of theory of elasticity and theory of structures.*: New York : McGraw-Hill, 1953.

192. Roters, A. and Johannsmann, D., *Distance-dependent noise measurements in scanning force microscopy.* Journal of Physics: Condensed Matter, 1996. **8**(41): p. 7561.

193. Hutter, J.L. and Bechhoefer, J., *Calibration of atomic-force microscope tips.* Review of Scientific Instruments, 1993. **64**(7): p. 1868.

194. Lima, J.A.S. and Plastino, A.R., *On the classical energy equipartition theorem.* Brazilian Journal of Physics, 2000. **30**(1): p. 176.

195. Godin, M., Tabard-Cossa, V., Grütter, P. and Williams, P., *Quantitative surface stress measurements using a microcantilever.* Applied Physics Letters, 2001. **79**(4): p. 551.

196. Dintwa, E., Tijskens, E. and Ramon, H., *On the accuracy of the Hertz model to describe the normal contact of soft elastic spheres.* Granular Matter, 2008. **10**(3): p. 209.

197. Bilodeau, G.G., *Regular Pyramid Punch Problem.* Journal of Applied Mechanics, 1992. **59**(3): p. 519.

198. Mahaffy, R.E., Park, S., Gerde, E., Käs, J. and Shih, C.K., *Quantitative Analysis of the Viscoelastic Properties of Thin Regions of Fibroblasts Using Atomic Force Microscopy.* Biophysical Journal, 2004. **86**(3): p. 1777.

199. Alberts, B., Bray, D., Hopkin, K., Johnson, A., Lewis, J., Raff, M., Roberts,K.,Walter, P.,, *Essential Cell Biology*. Second Edition ed. 2003: Garland Science/Taylor & Francis Group

200. Miller J. N. and Miller J. C., *Statistic and chemometrics for analitical chemistry.* 2005: Pearson Education Limited.

201. Wozniak, M.J., Kawazoe, N., Tateishi, T. and Chen, G., *Monitoring of mechanical properties of serially passaged bovine articular chondrocytes by atomic force microscopy.* Micron, 2009. **40**(8): p. 870-875.